DEFECT-INITIATED FRACTURE AND STRENGTH OF CERAMICS

By

© JASON SUNG, B.Eng., M.Sc.

A Thesis

Submitted to the School of Graduate Studies

in Partial Fulfilment of the Requirements

For the Degree

Doctor of Philosophy

McMaster University

October 1988

DEFECT-INITIATED FRACTURE AND STRENGTH OF CERAMICS

DOCTOR OF PHILOSOPHY (1988) MCMASTER UNIVERSITY

(Materials Science and Engineering) Hamilton, Ontario

TITLE: Defect-Initiated Fracture and Strength of Ceramics

AUTHOR: Jason Sung, B.Eng. (Cheng-Kung University, Taiwan)
M.Sc. (Tsing-Hua University, Taiwan)

SUPERVISOR: Professor P.S. Nicholson

NUMBER OF PAGES: 224, (xx)

ABSTRACT

The strength of ceramics is related to their fracture toughness and the fracture-initiating defects. The present thesis reports investigations of the strength/defect relationships that increase understanding of strength-improvement pedagogies and strength prediction methodologies for ceramics.

The strength improvement of a 4.5 wt% yttria-partially-stabilized zirconia (Y-PSZ) via defect elimination is demonstrated. Defect types were identified and eliminated via several novel techniques. These procedures were combined with a conventional sintering route. A crack model is developed and used to examine the discovered flaw/strength relationships. Four-point-bend flexural strengths were systematically improved from 880 to 1380 MPa, a value comparable to hot-isostatically-pressed or slip-cast materials.

The flaw/strength relationships for various fracture origin types were examined, i.e. fiber inclusions, agglomerates, iron inclusions, pores and alumina inclusions. An order of flaw-type severity was discovered and defect types of the same "size" were found to act in a dissimilar fashion in fracture initiation. The "severity" is related to local residual stresses around defects due to thermal

mismatch or differential sintering. The relative defect-severity was quantitatively ranked via the apparent fracture toughness and a "relative defect severity parameter" developed.

The temperature dependence of this parameter for the various defect types was investigated and the behavior explained via residual stress relief. Combined high-temperature four-point-bend and chevron-notched-bar fracture toughness (K_{Ic}) tests were conducted. It was found that the residual stress associated with alumina defects in tetragonal zirconia was temperature-dependent, that associated with agglomerates, temperature-independent and could be annealed. No residual stress was associated with pores. The residual-stress relaxation temperature (T_g) was determined for tetragonal zirconia.

The size equivalence of inclusion defects and the resulting flaws was investigated. The fracture behavior of alumina inclusions was investigated via an Al_2O_3-ZrO_2 composite layer sintered onto the tensile surface of PSZ four-point-bend bars. It was found that inclusion fracture exclusively occurred and the fracture was associated with weak interfaces between the grains of the alumina inclusion or between the inclusions and matrix.

Crack initiation in the fracture-toughness chevron-notched-bend bar was studied. Ideal testing conditions for valid K_{Ic} values strongly depend on specimen preparation and

material. An in-test precracking technique was developed for K_{Ic} testing at room and elevated temperatures. A Y-PSZ ceramic was tested and ideal testing conditions proven.

Defect-initiated fracture models for ceramics were developed. Fracture initiation at a typical inclusion with a thermal expansion coefficient and fracture toughness lower than the matrix and a Young's modulus higher than the matrix was analyzed and modeled for a spherical inclusion using a weight function method to compute the residual stress intensity factor and a part-through elliptical crack model to follow the crack extension. The model was used to predict the strength of PSZ containing α-Al_2O_3 inclusions. It was also used to compute the T_g for tetragonal zirconia. The predictions were in good agreement with the experimental data. For agglomerate-initiated fracture, an agglomerate-sintering/residual-stress-retention model is proposed and used to estimate the fracture stress for agglomerate-matrix decohesion. The residual stress levels after elastic and thermal recovery were estimated and agreed with experimental data.

ACKNOWLEDGEMENTS

The author wishes to express his gratitude for the guidance and support of his supervisor, Dr. P. S. Nicholson and the suggestions and encouragement of his Committee members, Drs. G. R. Piercy and R. Sowerby.

The author would also like to thank all who helped his work. Their kindness and patience enriched his laboratory life.

The financial support from the National Science and Engineering Research Council of Canada is acknowledged.

TABLE OF CONTENTS

LIST OF FIGURES

LIST OF TABLES

LIST OF SYMBOLS

a	Crack length, semi-axis of an elliptical flaw.
a_c	Critical flaw size.
A	Crack area.
α	Thermal expansion coefficient.
α_0	Normalized initial crack length in chevron-notched bar
α_1	Normalized crack length corresponding to the specimen thickness in chevron-notched bar.
b	Specimen width.
B	Specimen width.
c	Semi-axis of an elliptical flaw, Cubic ZrO_2 phase.
d	Specimen thickness.
D_m	Microscopic particle diameter.
D_{vel}	Equivalent settling velocity diameter.
E	Young's modulus.
ε	strain.
Φ	Shape parameter.
ϕ	Plastic constrain factor.
G	Strain energy release rate.
G_m	Shear modulus of matrix.
g	Gravitational acceleration.
γ_i	Effective surface energy for crack initiation.
η	Viscosity.
h	Weight function.

H	Young's modulus in plane strain condition, Hardness.
K	Bulk modulus.
K_I	Plane-strain stress intensity factor of Mode I fracture.
K_{Ic}	Critical K_I.
L	Outer span of the four-point-bend fixture.
m	Monoclinic ZrO_2 phase, Weibull modulus.
μ	Crack opening displacement.
P	Loads, Probability of failure.
P_{max}	Maximum loads.
r	distance.
R	Radius of a spherical particle.
R_c^{min}	Minimum critical inclusion size.
ρ	Density
S	Flexural strength.
θ	angle.
σ	Applied stress.
σ_f	Fracture stress.
σ_m	Mean fracture stress.
σ_r	Radial component of residual stress.
σ_s	Residual stress on the crack surface.
σ_t	Tangential component of residual stress.
σ_T	Hydrostatic thermal stress in inclusion.
$\sigma(t)$	Viscoelastic stress.
t	Tetragonal ZrO_2 phase.
T_g	Residual-stress relaxation temperature.

T_r Room temperature.

V_t Terminal settling velocity.

ν Poisson's ratio.

ξ Stress concentration.

W Specimen width.

Y Geometrical parameter.

Y^* Compliance function for the chevron-notched geometry.

Y^*_m Minimum Y^*.

Z Shape parameter.

To tsernmei

and my parents

CHAPTER 1

INTRODUCTION

Ceramics are brittle at ambient temperatures. Fracture initiation and strength are correlatable with the characteristics of the defects at fracture origins, i.e. the flaw dimensions and distance from stressed surfaces. Various explicit flaw/strength relationships have been suggested and the strength of ceramics can be improved by eliminating the fracture-initiating defects. One effective means of defect elimination from ceramic powders is colloidal processing. Defects of different size and density from the powders can be settled following dispersion in appropriate liquids. The techniques have not been systematically studied.

Previous experimental investigations of flaw/strength relationships for ceramics revealed that different defect types initiate fracture differently and the ceramic strength is modified by specific fracture-initiating defects. This "relative severity" of defect types has not been precisely characterized.

Residual stresses resulting from thermal contraction mismatch between the defect and its matrix are believed responsible for these strength modifications. This issue has been difficult to analyze as elastic mismatches in loading

and stress-field perturbation upon crack extension complicate the system. Previous theoretical treatments were non-rigorous and results did not agree with experimental data. Direct evidence for the existence of residual stresses associated with fracture-initiating defects has not been reported. To understand the defect-initiated fracture and strength of ceramics these issues must be clarified.

In the present work, experimental studies were conducted on a yttria-partially-stabilized zirconia (Y-PSZ) ceramic. This material was used as a model to demonstrate the strength improvement via various processing routes, to characterize the relative severity of the defect types and to explore the existence of residual stresses associated with the defects. Inclusion-initiated and agglomerate-initiated fracture were modelled and the results were compared with experimental data. Fracture toughness (K_{Ic}) measurements were made using chevron-notched bend bars. This led to the development of an improved technique involving in-test subcritical precracking.

CHAPTER 2

LITERATURE REVIEW

2.1 Defect-Controlled Fracture in Brittle Solids

Fracture behavior of brittle elastic solids like zirconia ceramics, is described by linear elastic fracture mechanics (LEFM) [Knott, 1973a]. The fracture stress under plane strain conditions can be explicitly correlated with the fracture toughness of the matrix (K_{Ic}) and the flaw-related defect geometry at the fracture origin [Broek, 1978a]. Since K_{Ic} is a material property [Knott, 1973b], matrix fracture is controlled by the fracture-initiating defects.

2.1.1 Flaw/Strength Relationships and Models of Crack Extension From Defects

An explicit expression for the flaw/strength relationship is essential for understanding defect-controlled fracture in brittle solids. Various models have been developed pertaining to crack extension from defects [Bansal, 1976; Baratta, 1978; Broek, 1978b; Evans, 1972; Irwin, 1962]. These have been derived from LEFM and feature particular crack geometries and cracked-body boundaries. In the simplest two-dimensional model [Broek, 1978b], the

plane-strain stress intensity factor for Mode I fracture (K_I) from a through-the-thickness embedded crack of length $2a$ subjected to a bi-axial or uniaxial stress field, σ, in an infinite plate is ;

$$K_I = \sigma \sqrt{\pi a} \qquad (2.1)$$

If the plate is of finite size, this equation is modified to the general form ;

$$K_I = Y \sigma \sqrt{a} \qquad (2.2)$$

where Y is the "geometrical factor" and is a function of the crack length and plate size. The fracture stress, σ_f, is thus related to the fracture toughness (K_{Ic}) and the critical flaw size (a_c) by ;

$$\sigma_f = K_{Ic} \frac{1}{Y \sqrt{a_c}} \qquad (2.3)$$

This flaw/strength relationship is the simplest for the real situation.

Real crack shapes and defect geometries are often elliptical and part-through-the-thickness [Broek, 1978c]. A more realistic elliptical crack model was developed by Irwin [1962] for which the relevant crack and plate configurations are shown in Fig. 2.1. The K_I value along the periphery of

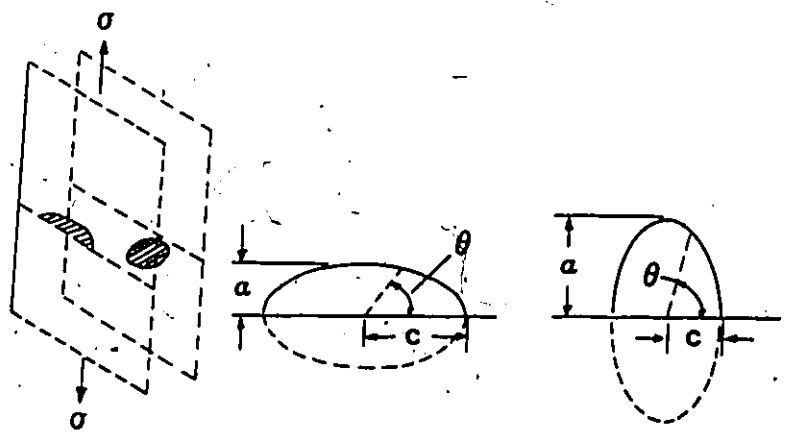

Fig. 2.1 Part-through elliptical crack model

an elliptical crack in the interior of a finite plate (or a semi-elliptical crack at its surface) subjected to a uniform tensile stress perpendicular to one of the elliptical axes is given by (See Appendix A) ;

$$K_I = G\,E = \frac{Y^2\sigma^2(1-\nu^2)}{\Phi^2}\left(\frac{a}{c}\right)\left(a^2\cos^2\theta + c^2\sin^2\theta\right)^{1/2} \qquad (2.4)$$

where G is the Strain-Energy-Release-Rate, E and ν the Young's modulus and Poisson's ratio respectively, σ the applied stress and a, c, and θ are semi-minor, semi-major axes and angle defined in Fig. 2.1. Y is the "geometrical parameter". For a subsurface elliptical crack, Y = 1.77 and for a surface semi-elliptical crack, Y = 1.94. (Similar numerical values were obtained in a recent study [SESA, 1980], where, for small crack-depth-to-plate-thickness ratio ≤ 0.05, Y converges to be independent of θ and a/c). Φ is a "shape parameter" and is an elliptical integral which varies with a/c as ;

$$\Phi_{a<c} = \int_0^{\pi/2}\left[1 - \left(1 - \frac{a^2}{c^2}\right)\sin^2\theta\right]^{1/2} d\theta \quad \text{, for } a \leq c \qquad (2.5a)$$

$$\Phi_{a>c} = \left(\frac{a}{c}\right)\int_0^{\pi/2}\left[1 - \left(1 - \frac{c^2}{a^2}\right)\sin^2\theta\right]^{1/2} d\theta \quad \text{, for } a \geq c \qquad (2.5b)$$

Φ can also be approximated by the polynomial

$[1 + 1.464(a/c)^{1.65}]^{1/2}$ within 2% error [SESA, 1980]. The maximum K_I occurs at $\theta = \pi/2$ for $a < c$ and at $\theta = 0$ for $a > c$. The Critical Stress Intensity Factor (fracture toughness), K_{Ic}, can be obtained from Eq. (2.4) as ;

$$K_{Ic} = \frac{Y\sqrt{1 - \nu^{12}}}{\Phi_{a<c}} \sigma_f \sqrt{a} \qquad \text{,for } a \le c \qquad (2.6a)$$

$$K_{Ic} = \frac{Y\sqrt{1 - \nu^{2}}}{\Phi_{a<c}} \sigma_f \sqrt{c} \qquad \text{,for } a \ge c \qquad (2.6b)$$

It is shown that the smaller dimension of the elliptical crack controls the fracture. If "a" is designated as the smaller crack dimension, Eq. (2.6) can be expressed in a flaw/strength relationship as ;

$$\sigma_f = \frac{K_{Ic}}{\sqrt{1 - \nu^2}} \frac{\Phi}{Y\sqrt{a}} \qquad (2.7)$$

Bansal [1976] modified Irwin's result by approximating the shape parameter (Φ) as the crack area, A, i.e. ;

$$\sigma_f \simeq \frac{1.68}{Y} \frac{K_{Ic}}{A^{1/4}} \qquad (2.8)$$

This equation is more conveniently applied to non-elliptical shaped cracks, but is limited to $0.2 \le a/c \le 3$.

Other crack models, such as Evans and Tappin [1972], incorporate the effective surface energy for fracture initiation, γ_i, i.e. ;

$$\sigma_f = \frac{Z}{Y}\left(\frac{2E\gamma_i}{c}\right)^{1/2} \qquad (2.8)$$

where c is the flaw size, E the Young's modulus and Z and Y are the Φ and Y of Irwin's model with fixed numerical values pertaining to specific crack geometries. Baratta [1978] derived a three-dimensional model for estimating K_I for a solid body containing a spherical void or a hemispheric surface pit as ;

$$K_{Ic} = \sigma_f(\pi L)^{1/2}\left[c - k(\tan^{-1}\alpha)^m\right]\left\{\frac{1}{2(7-5\nu)}\left[(4-5\nu)\left(\frac{1}{\alpha+1}\right)^3 + 9\left(\frac{1}{\alpha+1}\right)^5\right] + 1\right\} \qquad (2.10)$$

where L is the width of the circumferential crack, ν the Poisson's ratio, R the radius of the void, $\alpha = L/R$ and c, m and k are constants.

Irwin's model was considered adequate for the present work since most real fracture origins observed herein were approximately elliptical. The two-dimensional model was also considered sufficient because fracture surfaces were observed to contain the cross-sections of the

fracture-initiating defects. To apply Irwin's model in flaw/strength characterization one needs to assume that the fracture-initiating defect size is equal to the corresponding flaw size. This is reasonable for some pore-like defects if the ratio of matrix grain size to defect size is very small [Rice, 1980a; Evans, 1980a]. In the case of inclusion defects, the occurrence of interfacial cracking or inclusion fracture [Green, 1983] justifies the application of the crack model so long as there is no concomitant crack extension into the matrix. But for radial cracking it may not be applied, because the resulting flaws are considerably larger than the corresponding defect sizes. These have been theoretically analyzed in previous studies [Davidge, 1968; Evans, 1974; Green, 1981, 1982]. It is suggested that various cracking conditions are best judged via experimental observation. Interfacial cracking and inclusion fracture are prominent and can be easily recognized. Radial cracking involves stable crack growth and crack arrest [Green, 1983a], which exhibits a more tortuous fracture surface region in contrast with the subsequent fast fracture region [Wiederhorn, 1974].

Application of the appropriate crack model correlating fracture stresses and fracture origin sizes is considered an effective means of evaluating the response of defects to various elimination techniques. It also facilitates identification of the relative severity of the

defect types. This "severity" issue is important but has attracted little attention [Evans, 1977, 1980a; Lange, 1986a]. Evans and co-workers [1977] predicted the relative severity of typical defects in structural ceramics via the equivalent sharp cracks. They further identified the trends in the severity of defect types in a silicon nitride [1980a] (Fig. 2.2(a)). Lange [1986a] recently generalized this issue and described a possible order of different common flaw populations which undermine the potential strength of ceramics (Fig. 2.2(b)). None of these studies have addressed the problem on an accurate and quantitative basis. Kirchner and co-workers [1986] recently attempted to correlate the fracture-stress/flaw-size relationship for various ceramics via an empirical equation similar to that of Irwin, with assigned values of geometrical and shape parameters for different defect types. The limited success of their results suggests that the relative severity of the defect types in ceramics could be identified quantitatively using an appropriate crack model for characterization.

2.1.2 Types of Fracture-Initiating Defects in Ceramics

The major types of fracture-initiating defects encountered in ceramics are machining flaws, agglomerates, inclusions and pores. These defects constitute fracture origins via peripheral cracks developed during processing [Evans, 1979a, 1982a; Reed, 1978; Rice, 1979] or in-situ

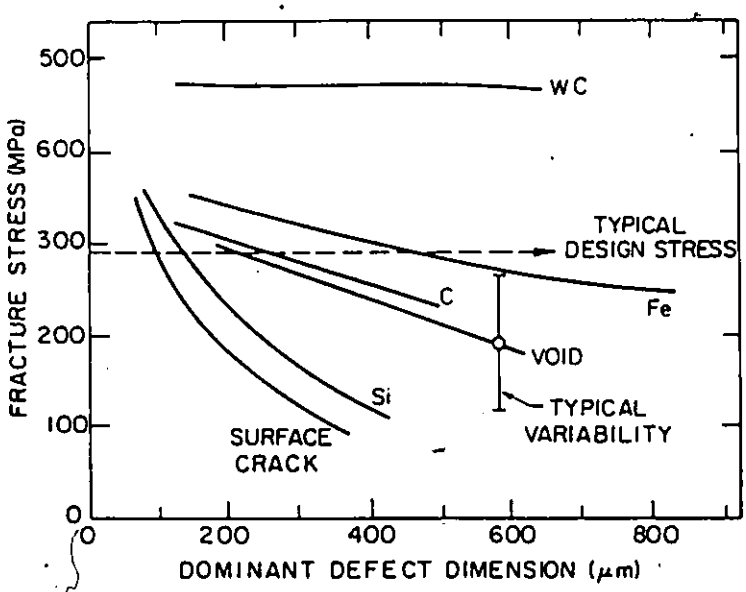

(a)

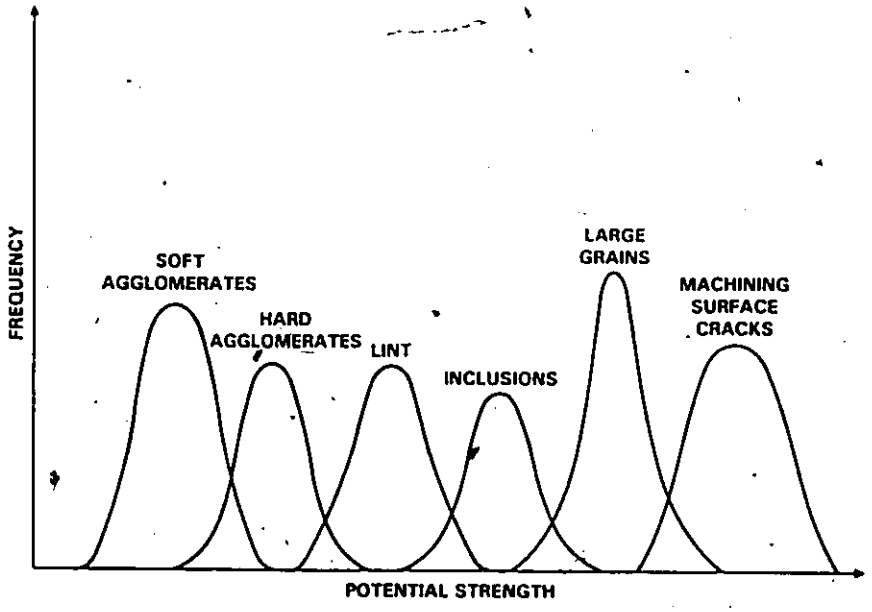

(b)

Fig. 2.2 (a) An trend in the severity of defect types in silicon nitride (b) Dependence of potential strength of ceramics on flaw population.

cracks developed in loading [Evans, 1980a]. Understanding these defect types is a prerequisite for their elimination and predicting their behavior in sintering and fracture. These are described as follows ;

(1) Machining Flaws

Machining flaws are surface penny-shaped or semi-elliptical cracks resulting from surface impact or penetration by hard objects such as grinding and cutting tools [Rice, 1979]. The formation of machining flaws are often simulated by indentation in which the residual tensile stresses underneath the indent due to non-accommodation of the elastic/plastic fields amplify preexisting flaws and result in local fracture [Ostojic, 1987]. Machining flaws are detrimental but inevitable due to necessary precision finishing procedures for ceramic components. The influence of machining on the strength of ceramics has long been a topic of interest [Schneider, 1972; Rice, 1979] and has resulted in a procedure being incorporated into a standard for the preparation of flexural test specimens [DOD, 1983].

(2) Agglomerates

Agglomerates are microstructural inhomogeneities due to preassociation of a number of grains in precursor powders [Pampuch, 1983]. Agglomerates are observed to have either higher or lower green density with respect to the surrounding compacted matrix [Lange, 1983a; Kellett, 1984]. The agglomerated powder grains are thought held by stronger

bonds which result from the partial sintering during powder synthesis [Lange, 1983a] or by weak Van der Waals bonds and surface charges [Barringer, 1984]. The former are termed "hard agglomerates" and the latter "soft agglomerates" in conventional terminology [Lange, 1986b]. It is expected that the hard agglomerates are those with higher green density than the matrix grains while soft agglomerates have a lower green density. During the firing of ceramics, powder agglomerates of differential density will result in locally enhanced sintering and the development of particular microstructures [Lange, 1983a, 1983b]. These usually consist of circumferential crack-like cavities between the agglomerate and its matrix. It has been considered [Evans, 1982a; Lange, 1983a] that the interfacial separation between an agglomerate and the matrix is the consequence of cracking resulting from radial tension developed by differential sintering. Since soft (lower-green-density) agglomerates will sinter faster than the surrounding higher-green-density matrix and consequently develop radial tension, they are often expected to be the source of agglomerate defects in the sintered ceramics. However, soft agglomerates are a weak structure, they may not survive powder treatments like sedimentation and green compaction [Graaf, 1983; Lange, 1986b]. The agglomerate defects in sintered ceramics most probably come from the hard agglomerates. There is evidence that hard agglomerates are more damaging [Hsueh, 1986] and

can also develop circumferential cavities after sintering [Lange, 1983a]. The specific sintering and cavity formation processes associated with the hard agglomerates have not been defined. Agglomerates have a definite influence on the sintering behavior [Rhodes, 1981] and the strength of the sintered body [Lange, 1986b]. The porosities accompanying agglomerate defects can hinder matrix densification during sintering and act as the fracture initiators on loading. Therefore elimination of agglomerates in precursor powders will promote sintering and increase final component strength by reducing the number and size of pore-like cavities therein.

(3) Inclusions

Inclusions are embedded extraneous particles with physical properties and chemical composition different from the surrounding matrix. Inclusions can be introduced into powders during synthesis or subsequent processing, e.g. sizing-down treatments (like milling), green compaction and atmospheric contamination (like lint) etc. [Evans, 1982; Lange, 1986b]. From the processing viewpoint, inclusions can be classified into inorganic inclusions (which survive sintering) and organic inclusions (which do not survive sintering). Solid inclusion defects induce residual stresses due to thermal mismatch (upon cooling from sintering temperatures) and/or elastic mismatch (upon loading). Complicated inclusion fracture, interfacial cracking or

radial cracking may occur, depending on the elastic modulus and fracture toughness of the inclusions with respect to the matrix [Evans, 1982a; Green, 1983a]. Organic inclusions in ceramic powders have attracted less attention. Lange [1986b] studied the sintering behavior of organic inclusions using incorporated polystyrene spheres. Pore-like defects were left in the ceramics on burn-out. Clearly, inclusions can become fracture origins due to associated cracks or pores.

(4) Pores

Pore defects are residual porosity not eliminated by sintering. These may originate from powder density gradients due to non-uniform size distribution of agglomerated powders or inhomogeneities developed during green compaction [Kingery, 1976a]. Circumferential cavities associated with agglomerates after sintering constitute a considerable component of the final porosity. Large pores responsible for strength degradation may result from the ripening of grain-boundary porosity [Kingery, 1976a], or the expansion of existing voids by gaseous phases generated and trapped on the decomposition of extraneous particles [Evans, 1982a]. Large pores will induce high stress concentrations and so may be directly involved in fracture. Small pores may interact with other defects in their vicinity and result in fracture [Evans, 1979a].

Identification and classification of fracture-origin defects is a well-established discipline [Mecholsky, 1976;

Rice, 1974; Richerson, 1982]. The location and geometry of fracture origins can be accurately determined by optical- and scanning-electron- microscopy (SEM). The chemistry of fracture origins can be identified by electron-probe micro-analysis (EPMA). However EPMA resolution is limited for low levels of foreign elements [Healey, 1984].

2.2 Defect Elimination Techniques

Defect elimination or size reduction can lead to improvement of ceramic strength. Several defect elimination techniques have been suggested and tested [Lange, 1986b; Parish, 1984, 1985; Rhodes, 1981] but the detailed processing steps have not been fully established. Some ceramic fabrication methods [Taguchi, 1985; Tsukuma, 1985a] also serve to eliminate defects. These will now be described.

2.2.1 Colloid Dispersion/Sedimentation

The precursor powders for advanced ceramics are usually 1 nm to 1 μm. They are termed as "colloids" [Miller, 1985]. Extraneous defects in ceramic colloids are inhomogeneities that can be isolated if the colloids are well dispersed. The separation of defects in dispersed ceramic colloids by liquid sedimentation is based on the different density or size of the defects relative to their fine powders. Differential settling velocities result and

corresponding settling time of the specific undesirable defects can be predetermined. This facilitates their removal. Sedimentation techniques have been effectively used to separate agglomerates from fine powders. Rhodes [1981] settled 6.5 mol% Y_2O_3-ZrO_2 powders in pH-1.2 water and obtained agglomerate-free powders which gave 74 % green density (usual maximum green density is ≃ 50 %) and 100 % sintered density at sintering temperature 400°C below normal (1100°C v.s. 1500°C). Lange [1986b] settled 2.3 mol% Y_2O_3-ZrO_2 powders in pH-2 water, eliminating hard agglomerates of size > ≃ 1 μm. The supernatant powder was subsequently slip cast giving a fired ceramic 350 MPa stronger than that of the as-received. Parish [1985] successfully prepared ZrO_2 powders with a narrow size distribution (0.4 to 0.6 μm) by repeated sedimentation in methanol but the sedimentation procedures were not reported. The application of Stokes' law to these non-ideal systems is not simple. Inclusion defects of higher density than the ceramic powders are also eliminated by sedimentation, but this has not been reported.

The sedimentation behavior of solid particles in liquids is often characterized by Stokes' law [Geiger, 1973] which describes the terminal settling velocity, V_t, of a single spherical solid particle in a dilute suspension as ;

$$V_t = \frac{2\,R^2(\rho_s - \rho_l)\,g}{9\eta} \qquad (2.11)$$

where R is the radius of the solid particle, ρ_s and ρ_l are the density of particle and liquid respectively, g the gravitational acceleration and η the viscosity of liquid. According to the original derivation, Stokes' law strictly applies only to a single spherical particle settling under laminar flow conditions. Corrections must be made to accurately determine the sedimentation time in practical colloid dispersions of non-infinite-dilute concentration and non-spherical particles. These corrections are associated with the non-sphericity, hydrodynamic and electrostatic effects (Appendix B). The non-sphericity of particle shape necessitates the definition of an "equivalent settling velocity diameter" (D_{vel}). This is defined as the diameter of an equivalent sphere having the same terminal settling velocity as the nonspherical particle. For most commonly encountered particle shapes, D_{vel} is smaller than the conventional optically microscopic particle diameter, D_m. Eq. (2.11) indicates that the actual settling velocity based on D_{vel} is smaller than the expected settling velocity based on D_m, i.e. under most conditions, particles will settle more slowly than predicted by Stokes' law. The non-infinite-dilution of colloid dispersions necessitates hydrodynamic and electrostatic corrections. The former arise from the backflow generated as a particle falls through a fluid dragging some fluid with it. In a bounded dilute system where particles are far apart, the overall effect of

this backflow is to hinder particle settling resulting in a decreased settling velocity as compared with that predicted by Stokes' law. The electrostatic effect is associated with the repulsion of charged particles which commonly exists in colloid dispersions and hydrodynamic influence comes into effect as a result of interparticle separation. The prediction of actual settling velocities in a practical fluid system is facilitated by incorporating a correction factor, F, into the right-hand side of Eq. (2.11) (Eq. (B.7)). The numerical value of F may be expressed as ;

$$F = (1.93\ \alpha_v)\cdot(1 - 6.55C)\cdot(2.32 - 1.5\ \rho_0^{2} - 3.75\ \rho_0^{-1}) \quad (B.8)$$

A theoretical prediction based on Eq. (B.8) has not been reported. It is suggested that experimental determination is best for the complicated systems.

Successful sedimentation requires good dispersion. Fine ceramic powders are normally flocculated due to weak London-van der Waals attraction [Woods, 1988b] or hydrogen bonds [Pimental, 1960]. Such aggregated powders will settle simultaneously with defects on sedimentation so effective dispersion is necessary. Dispersion of fine ceramic powders consists of three stages: (a) wetting the powders, (b) breaking up the powder clusters and (c) stabilizing the particles against flocculation [Parfitt, 1973]. Stage (a) involves interaction between the particles and dispersion

media wherein the degree of wetting depends on a balance of the surface tensions of solid, liquid and vapour [Parish, 1985]. Liquids with high surface tension (eg. water) inhibit proper wetting and addition of "surfactants" decreases the liquid surface tension and promotes wetting. Stage (b) involves mechanical agitation to expose new surfaces to further wetting. This may require simple stirring or more rigorous ultra- sonification or milling, depending on the agglomerated state of the powder. Ultrasonification has been shown more effective than milling for breaking up soft agglomerates [MacKinnon, 1983]. Milling also serves to down-size fine powders and hard agglomerates therein. Milling can however introduce extraneous contamination from the mill or its media, causing subsequent problems [Ferrari, 1983]. Stage (c) involves the development of interparticle repulsions to counterbalance the London-van der Waals attractions which naturally exist between particles. The common repulsion sources in colloid systems are electrostatic and steric repulsion [Miller, 1985]. Electrostatic repulsion interactions between colloidal particles arise from the "electrical double layers" associated with adsorbed ions on the solid and counterions in the solution. For metal oxides the surface adsorbed ions are often [H^+] which lead to counter [OH^-] ions in the diffuse layer in the solution. Adjustment of the pH away from the "ZPC" (zero point of charge, the pH value of the

suspension that results in zero surface charge) leads to effective electrostatic repulsion [Woods, 1988c]. The magnitude of dielectric constant of the solution is an indication of the ability of a solution to hold charge. The higher the dielectric constant the stronger the potential repulsion [Parish, 1985]. The combined effects of the London-van der Waals attraction and electrostatic repulsion explain many colloid dispersion phenomena and is the basis of the DLVO theory[1] [Miller, 1985]. DLVO theory predicts a maximum in the total interaction energy curve such that sufficient energy must be provided to surmount this barrier to make flocculation occur, i.e. the system is in its stabilized dispersed state. This state of affairs is illustrated in Fig. 2.3. Steric repulsion is the interaction between particles due to the adsorption of large macromolecules or polymers thereon. Part of the adsorbed molecule is soluble in the solution and extends away from the particle surface forming a steric barrier to the approach of other particles so promoting deflocculation. No maximum exists in the combined energy curve of London-van der Waals attraction and steric repulsion indicating that steric stabilization may be more reliable and efficient than electrostatic stabilization. Steric stabilization is only

---

1. This theory was developed by Derjaguin, Landau, Verwey and Overbeek.

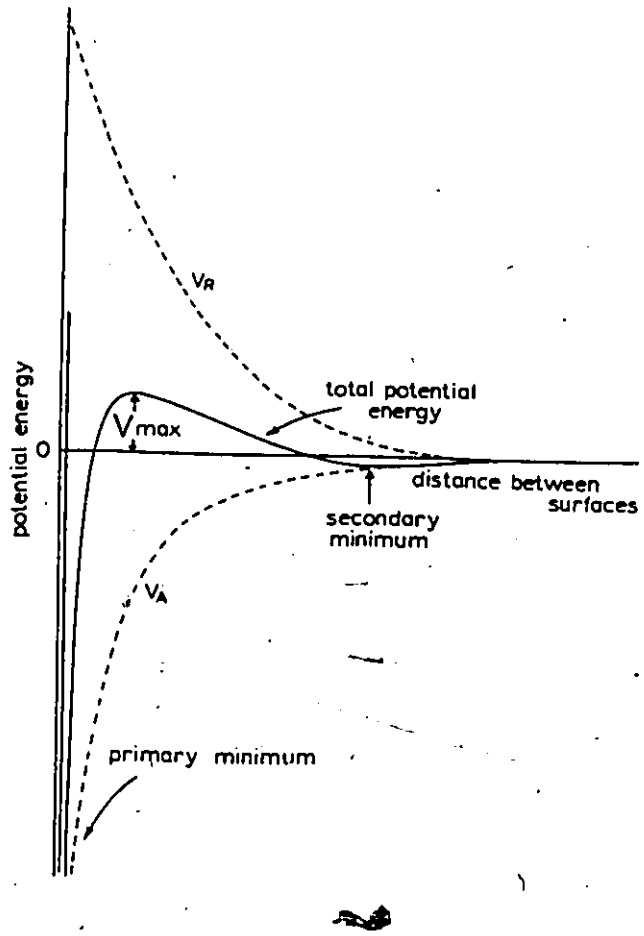

Fig. 2.3 Combined London-van der Waals attraction and electrostatic repulsion (DLVO theory)

understood qualitatively in comparison with the quantitative predictivity of the DLVO theory [Miller, 1985]. It is considered that electrostatic stabilization is sufficient for colloid-dispersion/sedimentation processes. Since this approach simplifies the design of experiments and interpretation of results thereof. It is also more useful as sedimentation may not require very stable dispersions (such as provided by steric interaction). Inhomogeneities in the fine powders must settle in a finite time.

Selection of appropriate media for good dispersion is a prerequisite for successful sedimentation. Several techniques exist for determining the dispersiveness of powders in liquid media [Mizuta, 1984; Parish, 1985; Woods, 1988c]. The "sediment volume test" is the simplest and although qualitative is sufficiently reliable. The procedure used by Parish [1985] to determine the dispersion ability of organic liquids for various oxides is as follows : 4 vol% powder is dispersed in 10 ml of liquid in graduated cylinders. After vigorous mixing, the suspensions are allowed to stand and settle. The final sediment volumes (heights) are used to indicate the dispersion ability of the media. In a flocculated system the particles will settle rapidly and a loosely packed sediment is obtained, i.e. the more agglomerated the powder, the "looser" the final packing nd the larger the final sediment volume. Conversely, in a well dispersed system particles settle into a tightly packed

bed and a smaller sediment volume results. Such tests have not been reported for tetragonal ZrO_2 powders. In spite of its semi-quantitative nature, results of sediment volume test are correlatable with actual dispersive properties [Parish, 1985].

2.2.2 Burnout/Re-Isostatic Pressing and Other Techniques

Organic inclusions from binders, lint in the air or general contamination are difficult to separate by sedimentation due to their low density. Lange [1986b] eliminated organic inclusions by prefiring the greenware to 800 °C for 15 hours and then re-isostatic pressing at room temperature. The organic material was burnt out and the residual porosity closed by the re-isostatic pressing. The organic inclusions were not directly observed but the strength increased ≃ 350 MPa which strongly supports their existence and elimination. Such processing is effective and feasible but the prior identification of the organic inclusions is necessary if they are to be avoided. In practice, burnout is a compromise between volatization of the organics and the non-initiation of sintering.

Several other ceramic fabrication procedures eliminate defects. Hot isostatic pressing (HIPping) [Larker, 1985] and slip casting [Tiller, 1986] are common processing routes for synthesizing high-strength ceramics. Both processes result in sintered bodies of nearly-theoretical

density so eliminating pore defects as fracture origins [Tsukuma, 1985a; Taguchi, 1985]. There is ample evidence that HIPping eliminates large interior pores [Tsukuma, 1985a], and eliminates the residual defects that accompany agglomerates [Tsukuma, 1985b], Slip casting prevents the formation of soft agglomerates [Lange, 1986b] and gives a high green density [Taguchi, 1985] (i.e. reduces pores during green compaction). This is especially so if the slip-cast ware is subsequently isopressed. However the exact nature of defect elimination is unclear as monitoring of defect behavior during processing is not possible.

Ceramics synthesized by conventional dry-pressing/ isostatic-pressing/pressureless-sintering have consistently lower strengths than those slip-cast or HIPped [Masaki, 1986; Matsui, 1984; Tsukuma, 1985a]. This is thought associated with the nonelimination of pore and agglomerate defects. The problems of attaining higher sintered density via this conventional route may be solved by selecting highly reactive starting powders and optimizing the sintering conditions.

From the the theory of defect-controlled fracture and techniques for defect elimination, it can be argued that improvement of ceramic strength depends on how the defects are eliminated rather than the fabrication procedures utilized. One aim of the present work is to combine conventional sintering with defect elimination techniques to

facilitate the synthesis of superior-strength ceramics.

2.3 Residual Stresses Associated with Defects and Their Analysis

Thermal contraction and elastic mismatch[2] between defects and ceramic matrices induce residual stresses inside and around the defects [Eshelby, 1972; Lange, 1978; Selsing, 1961]. These residual stresses are believed to play a role in fracture initiation [Evans, 1974, 1980a] and matrix strength is modified [Davidge, 1968; Green, 1982]. However, previous theoretical models [Evans, 1974, 1980a; Green, 1982] do not correlate well with experimental results. The analytical procedure used to approach these problems is to superimpose the stress intensity factor associated with the residual stress upon that resulting from the applied loads [Knott, 1980]. Since the latter is often known, it remains to determine the residual stress intensity factor. A "weight function method" is particularly useful for this task [Rice, 1972]. It directly tackles the residual stresses acting on the crack lines, but its application to ceramics has not been reported. Residual stresses are also likely developed during the differential sintering of the agglomerates to

---

2. Stress induced by elastic mismatch is actually a transient stress. Insomuch as they interact with residual stresses from thermal mismatch, they are considered as equivalent to residual stress in the present study.

produce crack-like cavities around the agglomerates [Evans, 1982b, Kellett, 1984, Hsueh, 1986]. The relevant fracture behavior of agglomerate defects has not been studied. In the following section the possible sources of residual stress associated with various defects are analyzed and the weight-function analytical method explained.

2.3.1 Sources of Residual Stress

Solid inclusions of different thermal expansion coefficient with an elastic matrix develop thermal stresses therein as the temperature changes. If these are not accommodated by the inclusion or matrix a residual stress develops [Evans, 1980b; Selsing, 1961]. Such is often the case for ceramics when cooled from sintering temperatures. Selsing [1961] analyzed the magnitude of residual stresses developed due to thermal contraction mismatch between a spherical inclusion and the matrix. A hydrostatic stress, σ_T, exists inside the inclusion given by ;

$$\sigma_T = \frac{\Delta\alpha \cdot (T_g - T_r)}{(1 + \nu_m)/2E_m + (1 - 2\nu_i)/E_i} \qquad (2.12)$$

where the difference of thermal expansion coefficients $\Delta\alpha = (\alpha_i - \alpha_m)$, T_r is the room temperature, T_g is defined as the temperature below which residual stresses are no longer relaxed via viscous deformation or lattice diffusion

[Evans, 1980b], ν is the Poisson's ratio and E the Young's modulus. Subscripts i and m refer to the inclusion and matrix respectively. For $\alpha_i < \alpha_m$ the hydrostatic residual stress is compressive whilst for $\alpha_i > \alpha_m$ it is tensile. The value of T_g has been theoretically calculated for alumina assuming relief by lattice diffusion [Evans, 1980b]. The presence of glassy phase at the grain boundaries of polycrystalline ceramics facilitates stress relaxation by viscous flow [Tsai, 1982]. In this case T_g is expected to be lower than that exclusively by lattice diffusion. The components of residual stresses, in the radial (σ_r) and tangential (σ_t) direction, in the matrix a distance r from the center of an inclusion of radius R are ;

$$\sigma_r = \sigma_T(R / r)^3 \qquad (2.13a)$$

$$\sigma_t = -1/2\ \sigma_T(R / r)^3 \qquad (2.13b)$$

In the vicinity of an inclusion, residual tangential tension tends to develop radial microcracking whereas residual radial tension develops circumferential microcracking [Green, 1983a]. The occurrence and degree of such microcracking depends on the magnitude of σ_T, the size of the inclusion and the size of preexisting flaws at the interface [Davidge, 1968; Green, 1981]. A minimum critical inclusion size (R_c^{min}) exists below which microcracking will not occur [Ito, 1980; Lange, 1978]. Once it does occur the

residual stresses will be relaxed. The extent of relaxation is thought associated with the residual-strain-energy-release-rate for crack extension [Ito, 1980; Green, 1981]. Ito [1980] particularly introduced a strain-energy-relaxation function to deal with this situation. Several techniques exist for measuring residual stress in materials [Blendell, 1982; Kino, 1980; Narayanaswamy, 1969]. These involve measurements on a macroscopic scale. Corresponding measurements have not been reported for microscopic residual stresses (eg. due to thermal mismatch around small inclusions).

Agglomerates in a powder compact are expected to develop residual stresses during sintering because their differential green density results in differential sintering vis-á-vis the surrounding powder [Evans, 1982b; Lange, 1983a; Hsueh, 1986]. Powder agglomerates with a lower green density than the matrix will develop radial tensile stresses at the agglomerate/matrix interfaces giving circumferential cavities [Evans, 1982b; Kellett, 1984; Lange, 1983a]. Lower-green-density powder agglomerates are unlikely to survive conventional ceramic processing processes [Graaf, 1983; Lange, 1986b], casting some doubt on their role as the agglomerate defects in sintered bodies. Lange [1983a] observed that those near-surface agglomerates of higher green density than the matrix could also develop circumferential crack-like cavities. This phenomenon was

attributed to the asymmetric stress fields resulting from the compression in the agglomerate/matrix interfaces and the tension on the surface. Real agglomerate defects with circumferential cavities have been observed in the interior as well as near the surface [Reed, 1878; Rhodes, 1981; Fegley, 1985]. Hsueh and Evans [1986] derived an expression for the viscoelastic stress developed around agglomerates during sintering based on the results of Evans [1982b]. They found that a hard agglomerate in a lower-green-density matrix might develop a stress several hundred times larger than that associated with a soft agglomerate and thus more likely become an agglomerate defect. The defect formation process associated with a hard agglomerate has not been analyzed. If the defects come from higher-green-density powder agglomerates, the associated cavity formation may not occur during the intermediate or later stages of matrix sintering, where a radial compressive stress exists. Pampuch [1983] suggested that higher-green-density agglomerates start and finish sintering earlier than the surrounding matrix. Therefore a radial tensile stress state develops as the higher-green-density agglomerate sinters faster than the matrix during the early stages of sintering. Cavity formation then occurs before the subsequent compressive stress state develops.

The residual stresses that develop as agglomerates sinter can be relaxed by viscous flow and formation of

circumferential cavities [Evans, 1982b; Lange, 1983a]. Lange [1983a] suggested a generalized expression for the residual strain resulting from the differential sintering of agglomerates. This residual strain ($\Delta\varepsilon$) was equated to the difference of linear sintering strain between the agglomerate and its matrix, i.e.;

$$\Delta\varepsilon = \varepsilon_m - \varepsilon_a = (\rho_{0a} / \rho_a)^{1/3} - (\rho_{0m} / \rho_m)^{1/3} \qquad (2.14)$$

where $\varepsilon_i = 1-(\rho_{0i}/\rho_i)^{1/3}$ is the sintering strain with respect to green density (ρ_{0i}) and sintered density (ρ_i). Subscripts m and a refer to the matrix and agglomerate respectively. Kellett and Lange [1984] measured maximum stresses of 1 to 3 MPa to develop during the intermediate stages of densification. This sintering stress is much less than predicted by Eq. (2.14) assuming elastic behavior[3]. This suggests that the differential sintering stresses must relax during the early stage of sintering and viscous processes cannot be neglected. Evans [1982b] conducted a viscoelastic analysis of residual stress formation and relaxation on agglomerate differential sintering. Steadily increasing transient stresses result from elastic stress build-up and viscous stress relaxation. Hsueh and Evans [1986] derived an expression for the developing viscoelastic stresses using

---

3. The comparision is demonstrated in Ch. 9.

a constitutive-law based experimental data. The hydrostatic elastic stress developed inside a spherical agglomerate is ;

$$\sigma = \frac{\Delta\varepsilon_a}{1/4G_m + 1/3K_a} \qquad (2.15)$$

where $\Delta\varepsilon_a$ is sintering strain difference between agglomerate and matrix, which is also defined in Eq. (2.14). G_m is the shear modulus of matrix and K_a the bulk modulus of agglomerate. The time-dependent viscoelastic stress, taking account of the viscous relaxation during sintering, can be expressed as ;

$$\sigma(t) = \int_0^t \frac{12K_aG_m}{3K_a + 4G_m} \Delta\dot{\varepsilon}_a(u)\ exp[-3K_aG_m(t-u)/(3K_a + 4G_m)\eta_m]du \qquad (2.16)$$

where $\Delta\dot{\varepsilon}_a(u)$ is the uniaxial strain-rate differential that establishes the stress and η_m is the viscosity of matrix. Eq. (2.16) was applied to agglomerate sintering in Al_2O_3. It was found that developing tensile stress for a lower-green-density agglomerate impedes the sintering and results in a maximum stress of 1 to 2 MPa. But a higher-green-density agglomerate develops a compressive stress as high as 300 MPa. The relevant circumferential cavity formation and its stress relaxation has not been treated. It is also not known whether the residual stresses are totally relaxed by cavity formation and sintering. Conditions for cavity

formation are expected to depend on the relative sintering rates, interfacial bond strength and the preexisting flaw size at the agglomerate/matrix interface. Ito's study [1981] of circumferential cracking around an inclusion suffering thermomechanical stress can be used to analyze this condition.

Solid inclusions of different Young's modulus with their elastic matrix induce elastic mismatch stresses on the application of an external load [Goodier, 1933; Hasselman, 1967]. Under uniaxial applied tension, stress concentrations develop inside and around the inclusion [Eshelby, 1972; Goodier, 1933]. The stress concentration within the inclusion, ξ_i, is given by [Eshelby, 1972; Evans, 1982a] ;

$$\xi_i = 1 + \frac{2\,[(E_i/E_m) - 1](1 - 2\nu)}{[(E_i/E_m)(1 + \nu)] + 2(1 - 2\nu)} \qquad (2.17)$$

The stress concentration around the inclusion is greatest at the interface. The magnitude and direction of these elastic stresses was exemplified for a perfectly rigid inclusion [Goodier, 1933]. A radial tension exists at the particle poles with a stress concentration, ξ_m^r, of magnitude ;

$$\xi_m^r = \frac{2}{1 + \nu} + \frac{1}{4 - 5\nu} \qquad (2.18)$$

for $\nu = 0.25$, $\xi_m^r = 1.96$. A tangential tension exists at the

particle equator with a stress concentration, ξ_m^t, of magnitude ;

$$\xi_m^t = \frac{\nu}{1 + \nu} - \frac{5\nu}{8 - 10\nu} \qquad (2.19)$$

for $\nu = 0.25$, $\xi_m^t = -0.03$, i.e. a compression results. The magnitude of ξ_m^r and ξ_m^t for a real inclusion are expected to be less than those for a perfectly rigid inclusion.

Inclusion defects have been extensively studied with respect to microcracking phenomena [Evans, 1980b; Ito, 1981; Green, 1983a], R_c^{min} under various conditions were explicitly determined and stress relaxation modeled. Little analysis exists on the influence of microcracking on strength [Evans, 1974, 1980a; Green, 1982]. Evans [1974] analyzed the case of a radial crack extending from an inclusion under the combined influence of thermal-contraction and elastic mismatch (i.e. $\alpha_i < \alpha_m$, $K_{ci} > K_{cm}$ and $E_i \neq E_m$, where K_{ci} and K_{cm} are the fracture toughness of inclusion and matrix respectively). A methodology was demonstrated. Evans [1980a] further analyzed an inclusion fracture model and tested it for silicon inclusions in silicon nitride. The measured strength was underestimated. Green [1982] analyzed a SiC defect in a Si_3N_4 matrix assuming no elastic mismatch (i.e. $\alpha_i > \alpha_m$, $K_{ci} < K_{cm}$ and $E_i = E_m$). An inclusion failure model was assumed and the results were claimed to correlate with experimental data. Both techniques [Evans, 1974; Green,

1982] used to calculate the stress intensity factor were restricted to a through-the-thickness crack or perturbation of stress fields by crack extension was neglected. A more rigorous analysis is necessary for the realistic situation for a part-through crack experiencing residual stresses that are partially relaxed by microcracking.

2.3.2. Weight Function Method

The stress field in an elastic body is modified by the presence of a crack and the modification is described by its stress intensity factor [Knott, 1973a]. In a multi-loading condition the total stress intensity factor for a specific fracture mode is the sum of the individual stress intensity factors for each loading condition of the same mode [Broek, 1978c]. The problem of crack extension under the combined influence of residual and applied stress is often simplified to the acquisition of a residual stress-intensity-factor if the applied stress-intensity-factor is known. According to the principle of superposition [Parker, 1981a], the local stresses acting on the crack line can be transferred to the remote boundaries (Fig. 2.4), provided the stress function associated with the cracked body is known. The residual stress-intensity-factor can then be acquired based on this "equivalent applied stress". If the relevant stress function is not known (and usually it is not) there are several analytical methods for acquiring the

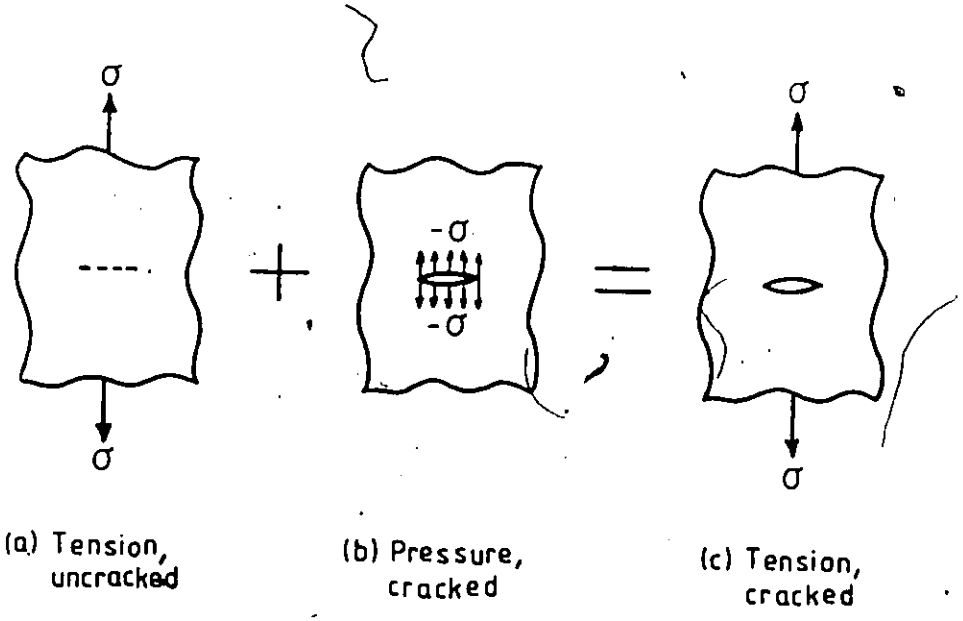

Fig. 2.4 Principle of Superposition

residual stress-intensity-factor [Parker, 1981b]. The "weight function method" is one of these which deserves special attention. This method deals directly with the residual stress acting on the crack surface and is therefore suitable for the inclusion problem. The non-uniform distribution of residual stress can be easily accommodated and the mathematical procedure involved is no more difficult than integration. The weight function method has been used to characterize the extension of part-through elliptical cracks (with large depth-to-thickness ratio) in weldments and during fatigue in metals [Besuner, 1974; Mattheck, 1983a, 1983b; Wu X, 1984]. The accuracy was shown comparable with that of the finite element method [Wu X, 1984]. This method has not been applied to defects in ceramics.

Following the expression derived by Rice [1972] and referring to Fig. 2.5, if the crack opening displacement and stress intensity factor are known for one crack geometry and loading (System (1)), the stress intensity factor can be obtained for any other symmetric loading (System (2)) applied to the same crack geometry . The "weight function" (h) for a two-dimensional crack symmetrical about the x-axis and extending in the x-direction is ;

$$h(x,a) = \frac{H}{2K_I^{(1)}} \frac{\partial \mu(x,a)}{\partial a} \qquad (2.20)$$

where μ is the crack opening displacement along the crack

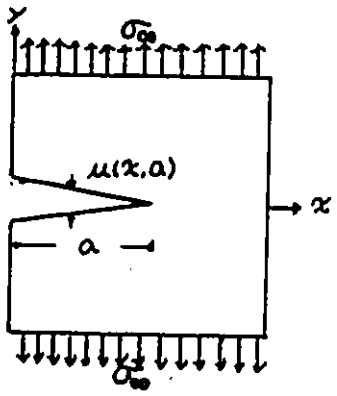

System 1

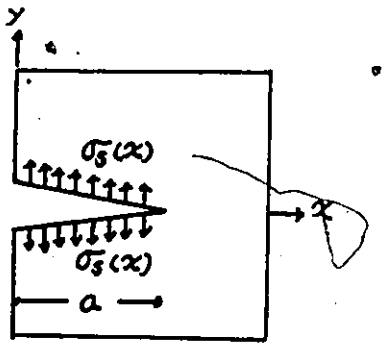

System 2

Fig. 2.5 Weight function method for acquiring the stress intensity factor

surface perpendicular to the x-axis, a the crack length, $K_I^{(1)}$ the stress intensity factor for a known symmetric loading (System (1)) and H = (E) (the Young's modulus) for plane stress and = $(E/(1-\nu^2))$ for plane strain. The stress intensity factor, $K_I^{(2)}$, for another symmetric loading (System (2)) with stress, $\sigma_s(x)$, acting along the surface of the same crack geometry is ;

$$K_I^{(2)} = \int_0^a \sigma_s(x)\, h(x,a)\, dx \qquad (2.21)$$

The final expressions for $K_I^{(2)}$ along the crack front of a two-dimensional crack was shown to be [Bueckner, 1971] ;

$$K_I^{(2)} = \frac{H}{K_I^{(1)}} \int_0^a \sigma_s(x)\, \frac{\partial \mu(x,a)}{\partial a}\, dx \qquad (2.22)$$

A general expression for $K_I^{(2)}$ for a three-dimensional crack was given by Bueckner [1977], but is difficult to reduce to the case of an elliptical crack. The average $K_I^{(2)}$ along an elliptical crack front has also been determined [Besuner, 1974]. However, the maximum $K_I^{(2)}$ at the ends of the semi-axes (Eq. (2.6)) must be known in order to study the crack initiation issue. This has not been determined.

To apply the weight function method to the problem of an inclusion with an elliptical-shaped flaw subjected to local residual stresses and remote uniaxial tension, the

parameters for System (1) can be taken from the results of Irwin's model (Ch. 2.1.1). The residual stress distribution along the crack surface for System (2) must be known .

2.4 Tetragonal Zirconia and Transformation Toughening

Tetragonal zirconia has recently emerged as a structural ceramic due to its unique stress-induced phase transformation toughening. Synthesis of tetragonal zirconia requires appropriate starting powders and optimum control of sintering. Studies of the transformation toughening have established the linear elastic nature of tetragonal zirconia and explained the high-temperature degradation of its mechanical properties. The characteristics of tetragonal zirconia and transformation toughening are now described.

Zirconia has three polymorphs [Subbarao, 1981], whose transformations are ;

$$\text{cubic (c)} \overset{2370^{\circ}C}{\rightleftarrows} \text{tetragonal (t)} \overset{1170^{\circ}C}{\underset{900^{\circ}C}{\rightleftarrows}} \text{monoclinic (m)}$$

The monoclinic phase is of little practical value. The high-temperature cubic or tetragonal phases can be stabilized by doping with conventional oxides such as CaO, MgO and Y_2O_3 or rare earth oxides [Garvie, 1972; Porter, 1979; Tsukuma, 1985c]. Fully-stabilized cubic zirconia is used as solid electrolytes [Baumard, 1984] and conventional refractories [Chen, 1983]. Partially-stabilized zirconia (PSZ) (c+t+m,

c+t, t+m, t) is used for structural applications such as tools, extrusion dies, liners for cylinders etc. [Butler, 1985; Garvie, 1984]. Fine-grained 100% tetragonal ZrO_2 polycrystals (TZP) are synthesized by doping ZrO_2 with 2-3 mol% Y_2O_3 [Claussen, 1984]. These ceramics are reported to have extraordinary mechanical properties at ambient temperatures [Masaki, 1986; Tsukuma, 1985a, 1985b, 1985d]. A comparison with other structural ceramics [Butler, 1985; Claussen, 1985] shows that the high strength, high thermal expansion coefficient and low thermal conductivity of tetragonal zirconia make it a potential candidate for the adiabatic heat engine [Katz, 1985]. A concentrated effort has improved the ambient-temperature strength and toughness of tetragonal zirconia. Average flexural strengths of 1500 MPa (3-point-bend for zirconia) [Masaki, 1986; Tsukuma, 1984, 1985a], and 2300 MPa (3-point-bend for zirconia composites) [Tsukuma, 1985d] have been obtained. The high ambient-temperature strength of tetragonal zirconia is attributed to the unique tetragonal → monoclinic phase transformation. The high-temperature strength of tetragonal zirconia is mediocre. The diminishing potency of the transformation toughening is considered responsible for this degradation [Claussen, 1985; Ingel, 1982; Tsukuma, 1985b]. Retention of the maximum possible tetragonal phase is essential in fabrication of tetragonal zirconia. This is accomplished via proper stabilizer amount and grain size

control as well as an optimized sintering schedule [Claussen, 1984]. The sintering temperature must reside in the tetragonal phase field as shown in the Y_2O_3-ZrO_2 phase diagram (Fig. 2.6) [Claussen, 1984]. In this field, the optimum sintering temperature and duration is a compromise between the prevention of excessive grain growth and full densification. Fig. 2.6 outlined several fabrication routes and their results. Only route 2 and 4 give fine-grained 100% TZP with good mechanical properties. Grain size control is also dependent on the precursor powder. Because the critical size for spontaneous transformation to monoclinic is $\simeq$ 0.3 μm [Gupta, 1978], the particle size of the powder must be < 0.1 μm. The relative amounts of the ZrO_2 phases in the sintered body are determined by X-ray diffraction and a typical intensity vs. 2θ diffraction plot for a partially-stabilized zirconia (t+m+c) is shown in Fig. 2.7 [Gupta, 1977]. The range (2θ = 25° to 40°) encompasses the strongest lines of the monoclinic phase ($\simeq$ 28.3° $(11\bar{1})$ and $\simeq$ 31.7° (111)) and the tetragonal phase ($\simeq$ 30.5° (111)). The cubic phase peaks merge in most cases with those of the tetragonal phase, making cubic characterization difficult (a slightly better distinction occurs at the t(222) peak where $2\theta \simeq$ 62° to 64°). The tetragonal → monoclinic transformation occurs more easily on the surface of tetragonal-zirconia bodies [Green, 1983a; Sato, 1985]. This transformation can be induced by grinding [Green, 1983a] or low-temperature

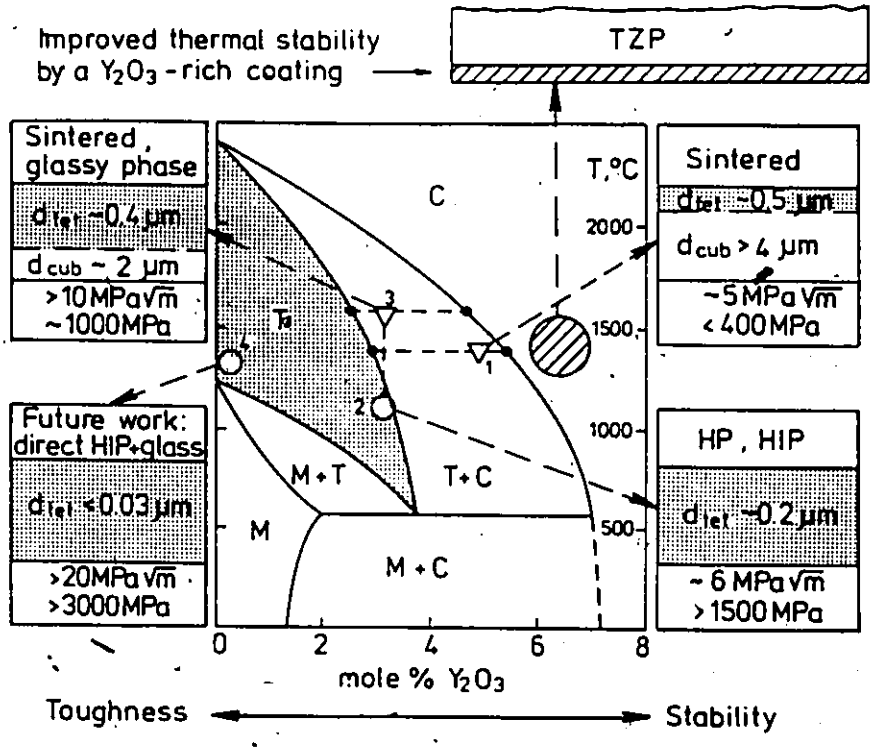

Fig. 2.6 ZrO_2-Y_2O_3 phase diagram and various sintering conditions.

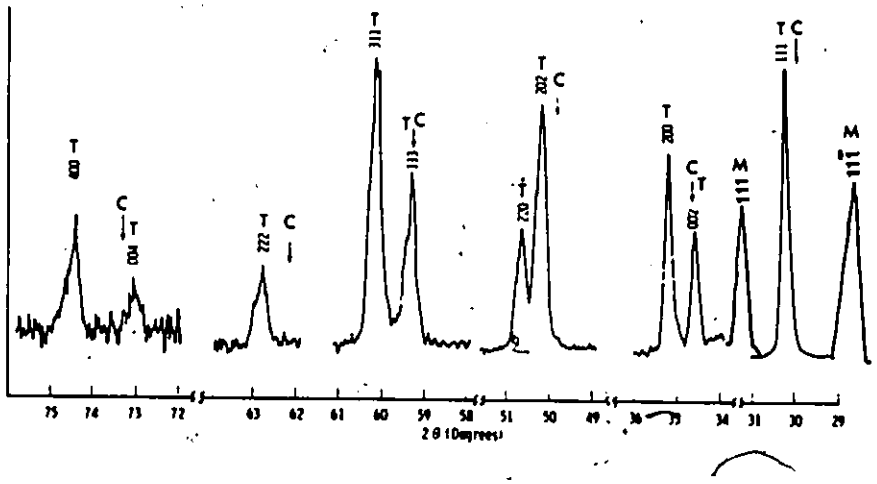

Fig. 2.7 X-ray diffraction pattern of tetragonal ZrO_2 and marked positions for cubic and monoclinic phases.

aging (in the range 200 to 300°C and especially in water) [Sato, 1985]. Transformation by low-temperature aging is effectively prevented by appropriate stabilizer levels and grain size control [Tsukuma, 1984]. The grinding-induced transformation leaves a residual compressive stress in the surface thereby strengthening these materials [Green, 1984]. This is not considered a reliable strengthening method as the transformed monoclinic layer can be polished away [Li, 1980] or re-transformed upon annealing (used in the present study). The machining (i.e. cutting and grinding) of test specimens can introduce surface compressive stresses. Chemical etching [Troczynski, 1987a] or annealing [Tsukuma, 1985b] effectively remove these stresses. The relevant quantitative procedure has not been established.

Transformation toughening originates from stress-induced phase transformation of the metastable tetragonal ZrO_2 phase to the monoclinic phase in the vicinity of propagating cracks [Gupta, 1978]. This transformation is martensitic and is accompanied by a volume increase of $\simeq$ 4% [Evans, 1980]. From the mechanics point of view [McMeeking, 1982], transformation toughening can be considered as originating from the residual stress field, or as a crack shielding process. The transformed zone ahead of the crack tip is under compressive stress following the transformation of tetragonal particles therein. The untransformed matrix is subject to a tensile stress. The residual stress developed

from the resulting inhomogeneity of stress states limits the crack opening so providing additional hindrance to the crack propagation. McMeeking [1982] modeled the crack shielding process and recognized that the transformation zone gradually develops to its full size as the crack extends. The local fracture toughness increase results in R-curve behavior (i.e. the crack extension resistance force increases as the crack advances), as shown in Fig. 2.8. The asymptotic value of the increased fracture toughness for a fully developed zone is given by;

$$\Delta K^T = [0.22/(1 - \nu)]\ E\ V_f\ e^T \sqrt{h} \qquad (2.23)$$

where ν is Poisson's ratio, E Young's modulus, V_f the volume fraction of transformable tetragonal phase, e^T the transformation strain accompanying the volume increase and h the transformation zone size. The constant term changes from 0.22 to 0.55 when the criteria for transformation includes a shear component [Swain, 1985]. The fracture toughness value predicted by the above theory agrees well with experimental data. Evans [1984] demonstrated that a thermodynamic approach yielded a similar result. Lange [1982a] considered a penny-shaped crack embedded in a stressed composite containing ZrO_2 inclusions. This alternative thermodynamic approach gave the increased strain energy release rate as ;

$$2\ R\ V_f(|\Delta G^\circ| - \Delta U_{ee}\ f) \qquad (2.24)$$

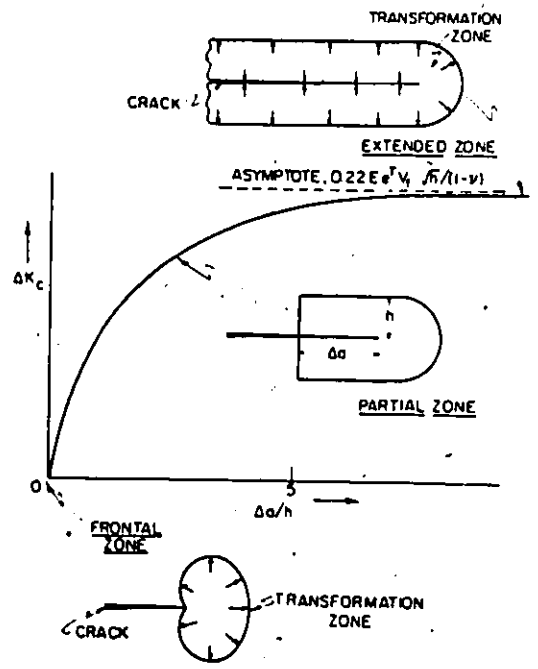

Fig. 2.8 Schematic showing the R-curve and the associated transformation zone shapes in transformation toughening.

where R is the size of the transformation zone, V_1 the volume fraction of the tetragonal phase and ($|\Delta G^c| - \Delta U_{ss} f$), the work done per unit volume by the stress field to induce transformation. Eq. (2.24) is identical to that of Evans which gave Eq. (2.23). The consistency of the various approaches indicate ZrO_2 transformation-toughening is well understood. Swain [1986] proposed recently that the R-curve behavior pertaining to transformation toughening may influence the linear elasticity and strength degradation of partially-stabilized zirconia. The stable crack growth accompanying the R-curve behavior will produce pronounced nonlinear and inelastic behavior. This may result in a final critical flaw size much larger than the original preexisting flaw so degrading the predicted strength. The extent of stable crack growth is expected proportional to the ΔK^T in Eq. (2.23) and hence the transformation zone size (h). Swain [1985] obtained experimental evidence that $MgO-ZrO_2$ and CeO_2-ZrO_2 having nonlinear inelastic loading responses also have large h values ($\simeq$ 30 μm). They also exhibit a disproportional low strength for their high fracture toughness (10 to 15 $MPa \cdot m^{1/2}$). Similar reasoning can apply to Y_2O_3-PSZ, though it has not been reported. For these ceramics, the transformation zone size is very small ($\simeq$ 2 μm) and the associated R-curve behavior is negligible [Swain, 1986]. Predictions based on this reasoning are consistent with their mechanical behavior, i.e. the load-

displacement curve is linear-elastic and the strength is exceptionally high with medium fracture toughness (≃ 6 to 9 MPa·$m^{1/2}$). Metastable tetragonal phase is retained at room temperature by stabilizer addition [Claussen, 1984; Tsukuma, 1985c] and grain size control [Gupta, 1978]. Optimum stabilizer contents are observed to coincide with the maximum retained tetragonal phase and fracture toughness [Tsukuma, 1984]. The maximum strength, on the other hand, does not coincide with the maximum fracture toughness for the various stabilizer levels [Masaki, 1986; Tsukuma, 1984]. The reason for this difference is not well understood. Suggested reasons are the existence of cubic phase [Tsukuma, 1984] or the occurrence of surface plastic deformation induced by the phase transformation [Swain, 1985]. This anomaly does not violate the flaw-strength relationship (Eq. (2.7)) or the transformation toughening theories (Eq. (2.23)) for fixed stabilizer type and content. The grain size dependence of tetragonal phase retention is illustrated by the spontaneous transformation of tetragonal grains over a critical size on cooling to room temperature [Gupta, 1978]. The existence of a critical size was thought the consequence of the balance between the transformation strain energy and the surface energy [Lange, 1982b]. For optimum mechanical properties it is necessary to use fine-grained starting powders and prevent exaggerated grain growth during sintering. The stress-induced phase

transformation is also temperature-dependent [Lange, 1982c]. The chemical driving force (and thus the free energy difference between the tetragonal and monoclinic phases) diminishes as temperature increases and vanishes above the phase transformation temperature. This is illustrated in Fig. 2.9(a), where the fracture toughness of tetragonal zirconia and its composites is drastically reduced with increasing temperature. The corresponding strength also decreases (Fig. 2.9(b)). Lange [1982a] explained this via the free energy term, ΔG^c, of Eq. (2.24). The tetragonal→monoclinic transformation temperature of PSZ was reported to be 600 to 800°C [Claussen, 1984]. The temperature dependence of the transformation toughening limits the usefulness of these ZrO_2 materials at elevated temperatures. Claussen [1984] pointed out that special high-temperature microstructures must therefore be developed.

2-3 mol% Y_2O_3-PSZ is a suitable model material for the present study. It is linear elastic at ambient temperatures and fits into the flaw-strength relationships of LEFM. The attainable high ambient-temperature strengths are expected to give a wide range of fracture stress following a series of processing modifications, thus a good characterization of flaw-strength relationships can be obtained using this material. There is a well-established data base of strength for this material fabricated by various methods. Finally, the prominent temperature-

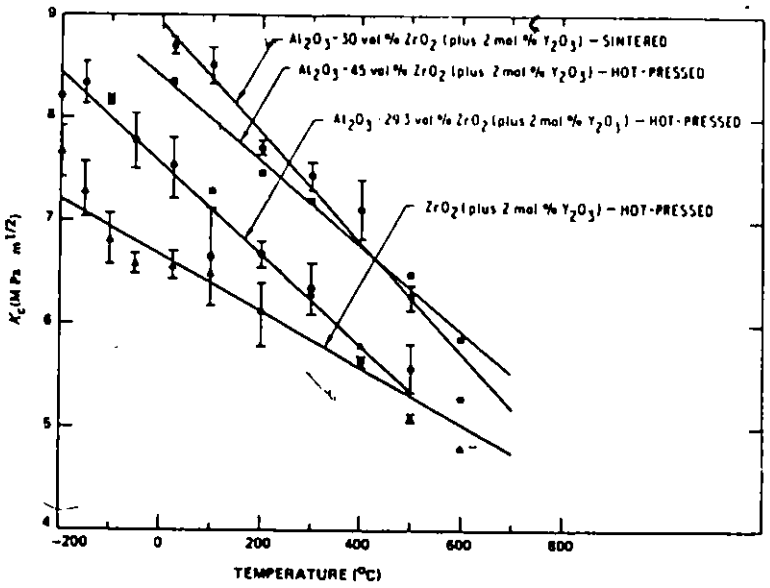

(a)

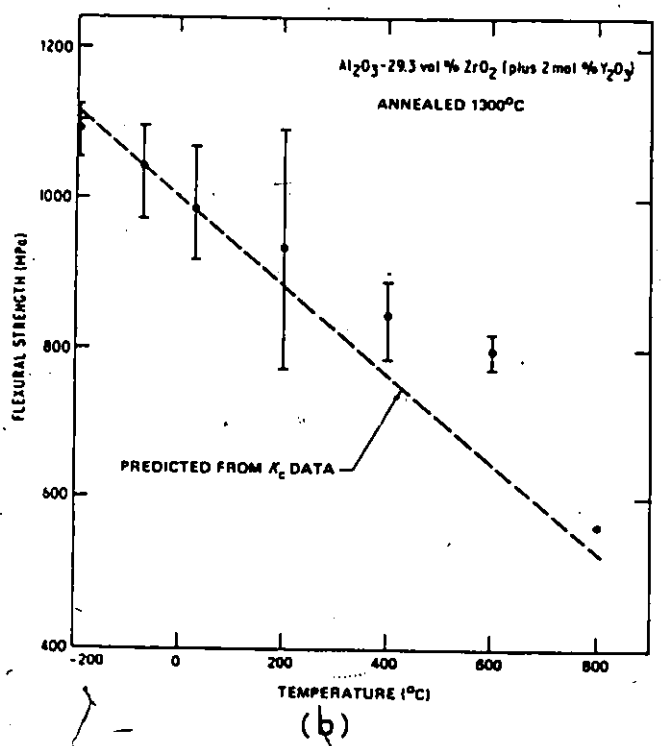

(b)

Fig. 2.9 (a) Fracture toughness plotted v.s. temperature for four ZrO_2 ceramics.(b) Flexural strength plotted against temperature for a ZrO_2-Al_2O_3 composite material.

dependence of fracture toughness in this material makes possible the distinct characterization of the flaw-strength relationships at elevated temperatures.

2.5 Principal Experimental Techniques

Many experimental techniques were used in the present study. Standard techniques including SEM, XRD and other sophisticated equipment which require routine operation and result interpretation are not described. Special techniques developed specifically for the present work are described in the experimental procedure sections. Those techniques vital for data procurement and experiments conducted, are now described.

2.5.1 Four-Point-Bend Strength Test and Weibull Statistical Analysis of Data

In the present study, strength data was acquired by the four-point-bend test. The reliability of strength data depends on the proper preparation of test specimens as well as the accurate performance of tests. The acquired strength data was analyzed by Weibull statistics

(1) Four-Point-Bend Strength Test

Strength is a property needed for design and development purposes. The tensile strength of a component is defined as the maximum opening-mode (mode I) fracture stress

in a uniform tensile stress state. It is related to the fracture-initiating flaw through the fracture toughness. The standard tension test for metallic materials is difficult to perform on ceramic materials due to fixture grip and specimen preparation problems [Quinn, 1984]. The bend test (flexural test) is most often used to determine the tensile strength of ceramic materials. The bend strength (flexural strength) is defined as the maximum outer fiber stress developed in the fracture of a standard rectangular beam. Three-point-bend or four-point-bend test geometries are conventionally used [Baratta, 1982], as shown in Fig. 2.10 (a). The four-point-bend test is preferred for design data as a larger test volume is involved in the maximum tensile stress region (Fig. 2.10(b)). This ensures a higher probability of stressing a critical flaw. The conventional formula used for calculating the bend strength of a rectangular beam, S, in four-point-bend flexure is [DOD, 1983] ;

$$S = \frac{3\,P\,L}{4\,b\,d^2} \qquad (2.25)$$

where P is the breakload, L the outer span, b the specimen width and d the specimen thickness. If the failure location of the specimen is outside the maximum fiber stress region, a correction must be made, i.e. ;

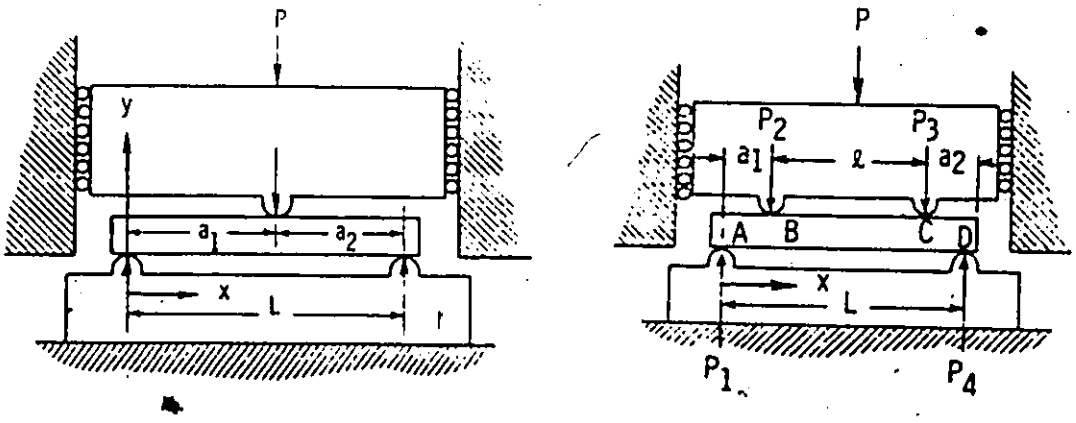

Three-point bend Four-point bend

(a)

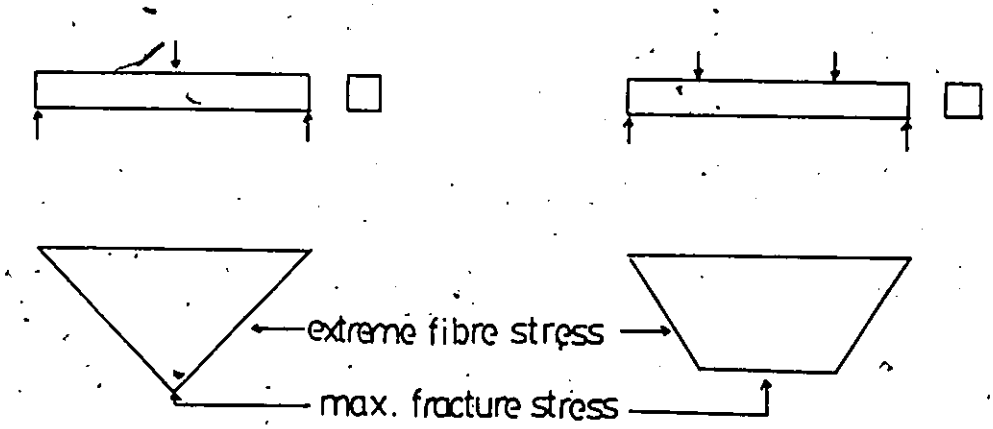

Three-point bend Four-point bend

(b)

Fig. 2.10 (a) Loading arrangement of three-point bend and four-point bend (b) Stress states of three-point bend and four-point bend.

$$S = \left(\frac{3\ P\ L}{4\ b\ d^2}\right)\left(\frac{L - 4x}{L}\right) \qquad (2.26)$$

where x is the distance between the nearest inner bearing cylinder and fracture surface. To characterize the flaw-strength relationship, the location of the fracture-initiating defects on the fracture surface must be known and the corresponding fiber stress (F.S.) determined as;

$$F.S. = S \cdot (2h\ /\ d) \qquad (2.27)$$

where h is the distance from the centre of fracture origin to the tensile surface. The variation of fiber stress across the fracture origin can be reasonably neglected since the natural flaw is very small compared with the thickness of specimen (observed in the present study). The bend-test specimen is very surface and edge sensitive and bend testing is very error-prone. A lack of adequate care in testing is often the major cause of the unreliability [Quinn, 1984]. A standard for the flexural test of ceramics at ambient temperatures has recently been prepared by DOD [1983]. This standard (MIL-STD-1942(MR)) is the most up-to-date and unified one in the United States. Similar standards also exist in Japan and Germany [Quinn, 1984]. The American standard was adopted in the present study. The specimen dimensions, finishing procedures, fixture design and machine cross-head speed are specified as per Table 2.1. In addition

Table 2.1 Summary of MIL-STD-1942(MR) for flexural test of ceramics at ambient temperatures

Specimen Dimension	Size A : 1.50±0.03mm x 2.00±0.03mm x 25mm Size B : 3.00±0.03mm x 4.00±0.03mm x 45mm Size C : 6.00±0.03mm x 8.00±0.03mm x 90mm
Specimen Finishing	Grinding Media : Water or other suitable media Grinding Mode : Surface, parallel to long axis, no blanchard or rotary grinding coarse stage : <0.03mm/pass and <0.06mm/face fine stage : with diamond wheel 200-500 grit, <0.002mm/pass and >0.06mm/face edge chamfer : four long edges at 45°, a distance of 0.15±0.05mm, or round with a radius 0.20±0.05mm
Fixtures (os./is.)	A : 20/10 mm, B : 40/20 mm, C : 80/40 mm (Accuracy ±0.10mm)
Roll Dia. CH. Speed	A : 2-2.5mm, B : 4.5mm, C : 9.0mm A : 0.2mm/min. B : 0.5mm/min., C : 1.0mm/min.
# of Specimens	Minimum 10 for estimating the mean σ_f, Minimum 30 for estimating the Weibull modulus

to conforming with the Standard's requirements, a sample holder is considered necessary to adjust the relative position of the specimen and the fixtures. The design and use of such a holder is part of the present study. No parallel standard for the high-temperature flexural test exists at present. DOD [1983] suggests that MIL-STD-1942(MR) be used as a basis and the fixture materials be converted to hot-pressed silicon carbide. They also recommend use of a

loading rate so fast as to cause fracture in a few seconds thus minimizing time-dependent phenomena such as creep and slow crack growth. The Japanese standard [JIS, 1981] recommends either silicon nitride, silicon carbide or alumina be used for the fixture construction.

(2) Weibull Statistical Analysis of Data

The strength data of ceramic materials exhibit a distribution of values which are adequately described by a Weibull distribution function [Weibull, 1951; Weil, 1964]. Use of the Weibull distribution function characterizes a set of strength data with respect to its variability (represented as the Weibull modulus) and its mean fracture strength. On such a basis, different sets of strength data can be compared. The two-parameter Weibull distribution function can be generally expressed as [Weil, 1964];

$$P = 1 - exp\left[-\left(\frac{\sigma_f}{\sigma_0}\right)^m K\cdot(V,S)\right] \qquad (2.28)$$

where P is the probability of failure, σ_f the fracture stress, σ_0 the scale factor (also the characteristic strength) and m the shape factor (also the Weibull modulus). K is a term related to loading configuration (i.e. tensile, 3-point or 4-point loading) and flaw location (surface flaw or volume flaw). (V,S) is the corresponding stressed volume (V) or surface area (S). In the four-point bend test,

$K = 1 / 2(m + 1)^2$ for a volume flaw and $K = \{[1 / (m+1)] + (b/d)\} / 2[1 + (b/d)]$ for a surface flaw [Jayatilaka, 1979]. The various methods of dealing with Eq. (2.28) lead to different values of m and σ_0 [Batdorf, 1978; Jeryan, 1978]. The position estimator, $P = (j - 0.5) / N$ (where j and N are the corresponding sequential and total number of specimens), shows the least bias [Bergman, 1986]. Curve fitting by the least squares method is the simplest way to analyze the data and gives high accuracy [Jeryan, 1978]. Eq. (2.28) can be rearranged in a linear form ;

$$ln\ ln\left(\frac{1}{1-P}\right) = m\ ln\ \sigma_f + \left[ln\ K\ (V,S) - m\ ln\ \sigma_0 \right] \qquad (2.29)$$

A plot of $ln\ ln[1/(1-P)]$ v.s. $ln\ \sigma_f$ with curve-fitting by least squares method gives a straight line of slope m (the Weibull modulus) and the intercept $[ln\ K(V,S) - m\ ln\ \sigma_0]$. The Weibull modulus is an indication of strength variability and a high value is desirable. The mean fracture stress, σ_m, can be obtained by inserting the specific K term and the stressed volume or surface area of the specimen into the intercept equation. This gives σ_0, and the following relationship [Stanley, 1973] ;

$$\sigma_m = \sigma_0\ \Gamma\left[1 + \left(\frac{1}{m}\right) \right] \left[K\ (V,S) \right]^{-1/m} \qquad (2.30)$$

where Γ is a gamma function. The calculation of σ_m is

tedious and not often done [Jayatilaka, 1979]. In most cases the arithmetic mean, σ_a, (at P = 0.5), is substituted for σ_m. This results in an error < ≃ 5% [Bergman, 1985] and is considered acceptable within the variability of the data. The accuracy of m and σ_0 (and hence σ_m and σ_a) strongly depend on the number of test specimens [Jeryan, 1978]. The MIL-STD-1942(MR) standard specifies at least 10 samples are required to obtain σ_a values and at least 30 samples for m. Even so a 2 to 4% error of average fracture stress and a 25% error of Weibull modulus, within a 90% confidence interval, may result.

2.5.2 Fracture Toughness Testing Using Chevron-Notched Bend Bar

In the present study the fracture toughness of the material is acquired by the chevron-notched-bend-bar technique. This geometry has the merit of easy specimen preparation without precracking and data procurement without knowledge of the crack length. This technique is therefore particularly suitable for ceramics. Subcritical crack growth problems and crack initiation difficulties can be associated with this type of specimen and result in invalid measurements. The present technique is therefore improved as part of the work reported herein.

Fracture toughness determinations for ceramic materials have utilized the double-cantilever beam (DCB) or

the double torsion (DT) technique [Freiman, 1988]. The precracking procedures with these geometries are often tedious and crack-length measurements have to be involved. Revised chevron-notched bar geometries have recently been developed, which eliminate the necessity of precracking and lead to easy computation of the fracture toughness value directly from the maximum load with no prior knowledge of the crack length [Barker, 1977; Shih, 1979]. Among several specimen types reviewed by Newman [1984] the bend-bar specimen is best for high-temperature determinations and was adopted in the present study. The loading arrangement and the geometry of the four-point-bend chevron-notched bar are shown in Fig. 2.11 [Munz, 1981]. A chevron-shaped notch is cut into one side of the specimen and, upon loading, a crack with initial length a_0 propagates from the chevron apex. The crack width, b, continuously increases from zero to the full specimen thickness B, corresponding to a crack of length a_1. Due to the special geometry of the chevron-notched bar, the stress intensity factor per unit load, K_I/P, decreases as the crack initially advances [Shih, 1981]. An increasing load is required to maintain crack extension and this results in stable crack growth. K_I/P passes through a minimum corresponding to the maximum load, thereafter K_I increases as the crack advances. Unstable crack growth then follows. The K_I/P v.s. crack-extension curve and the corresponding load-displacement curve are schematically

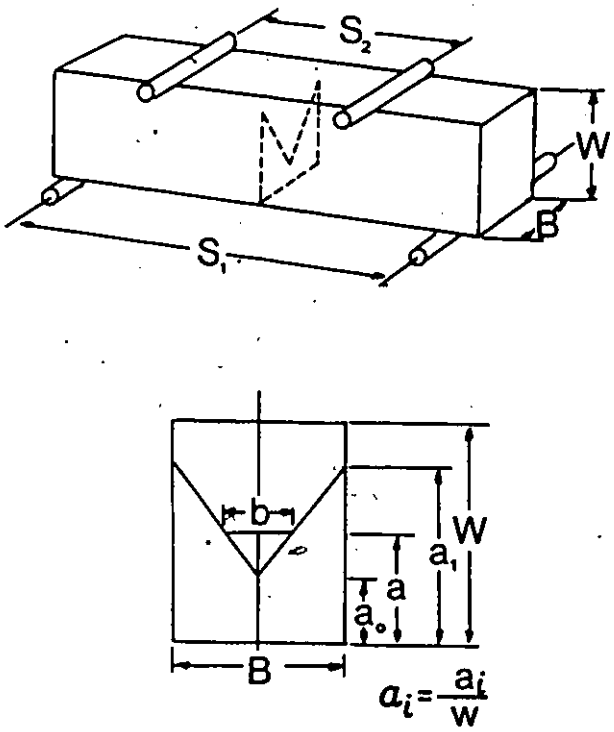

Fig. 2.11 Loading arrangement and specimen geometry for a chevron-notched four-point bend bar.

shown in Fig. 2.12. Munz [1981] used an energy balance analysis to derive a stress-intensity-factor expression for the chevron-notched bend bar in the stable crack growth regime. A compliance function, Y^*, is involved in his expression. This has the same characteristics as K_I/P. The fracture toughness is evaluated at the onset of unstable fracture where the maximum load (P_{max}) and the minimum Y^* (Y^*_m) occurs i.e. ;

$$K_{Ic} = \frac{P_{max}}{B\sqrt{W}} Y^*_m \qquad (2.31)$$

The compliance function (Y^*) is derived either from a straight-through-crack assumption [Munz, 1981] or a slice model [Bluhm, 1975]. Y^*_m is obtained by curve-fitting , i.e.;

$$Y^*_m=(3.08+5.00\alpha_0+8.33\alpha_0^2)\frac{S_1-S_2}{W}\left[1+0.007\left(\frac{S_1S_2}{W^2}\right)\right]^{1/2}\left(\frac{\alpha_1-\alpha_0}{1-\alpha_0}\right) \qquad (2.32)$$

where all the parameters are as specified in Fig. 2.11. To apply Eq. (2.31) with validity, stable crack growth must precede the final unstable crack growth. This condition appears on a load-displacement curve as a nonlinear region between the initial elastic region and final fracture [Munz, 1983]. The influence of notch geometry on K_{Ic} has also been extensively studied [Munz, 1980, 1981; Salem, 1987; Shannon, 1984]. It is generally agreed that in the

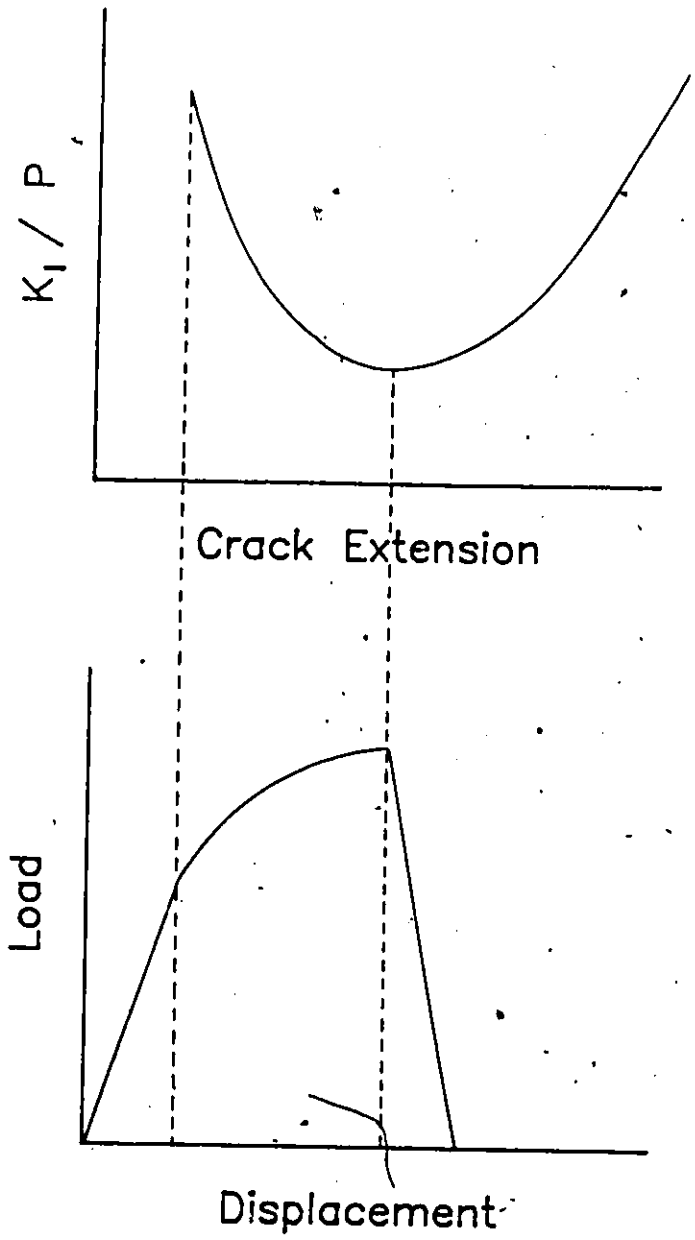

Fig. 2.12 K_I/P-a curve and load-displacement curve for a chevron-notched bend bar

range of α_0= 0.2 to 0.6 and α_1= 0.8 to 1.0 the measured K_{Ic} value is independent of geometry. The influence of the displacement rate on K_{Ic} has not been ascertained. A low machine cross-head speed (≃ 0.05 mm/min) was conventionally used in previous studies. This speed is about ten-times lower than that used for the flexural testing of ceramics [DOD, 1983]. The latter was chosen to avoid the subcritical crack growth. It is known that ceramics are susceptible to subcritical crack growth in corrosive environments at the stress intensity factors well below the critical value [Wiederhorn, 1974]. Similar behavior has also been found at high temperatures [Evans, 1986]. In both cases, the crack velocity (V) is related to the stress intensity factor (K_I) giving a three-region K_I-V curve. A lower limit "threshold" K_I exists below which crack will not grow. At high stress levels, the curve asymptotes to K_{Ic}. Between the threshold K_I and K_{Ic}, subcritical crack growth follows a power law relation and the crack grows at a relatively constant speed over a considerable range of K_I. Recently Troczynski and Nicholson [1987b] studied the theoretical effect of subcritical crack growth on K_{Ic} determinations via chevron-notched specimens. They found the commonly employed low displacement speed could promote subcritical crack growth during stable crack extension and might invalidate the K_{Ic} determination using the P_{max} value (Eq. (2.31)). Experimental evidence was not given. To obtain valid K_{Ic}

values via chevron-notched bend bar testing, displacement rates free of subcritical crack growth must be used.

The merit of elimination of precracking in the chevron-notched specimen may be overestimated, particularly for the ceramic samples. Recent studies of Troczynski and Nicholson [1985, 1987b] have demonstrated that overload is necessary for crack initiation due to non-ideally machined chevron-notched tips in an 8 wt% Y-PSZ ceramic. This non-ideal condition was analyzed and modeled [Troczynski, 1987b]. Similar analyses are also found in earlier studies [Bluhm, 1978; Wu S., 1984]. A modified chevron-notched sample specially for ceramic materials was recently developed [Himsott, 1987]. Knoop indentation was used to introduce a sharp starter crack at the chevron tip and tests were performed on several silicon nitride and silicon carbide materials. However, the success rate of valid tests was only 30%. In a more recent series of tests performed by Sung and Nicholson [1988], extreme care was taken to prepare specimens of 4.5 wt% Y-PSZ to ensure sharp chevron tips but still the test data did not produce valid results. It is thought that transformation-induced compressive residual stresses resulting from the machining of the material [Green, 1983b] may deactivate surface microcracks as crack initiators. Clearly crack initiation at lower loads in ceramic chevron-notched bar specimens is not guaranteed either because of improper specimen preparation or due to

intrinsic material properties. The required overload may easily exceed the maximum load resulting in immediate catastrophic fracture with no stable crack growth. An improved precracking technique is needed. It is suggested that crack initiation in chevron-notched ceramic specimen will never be as easy as expected. The conventionally employed low displacement speed is very likely to promote subcritical crack growth and so facilitates the crack initiation at a lower threshold K_I, (i.e. lower load). However it is argued that stable crack extension under subcritical conditions will not be related to K_{Ic}, resulting in invalid fracture toughness determination. Only if the displacement speed is changed after subcritical precracking to that for fast fracture will the test be valid. This rationale has become part of the present study.

2.5.3 Fracture Toughness Testing Using Microindentation

Hard indent contact with the surface of brittle materials produces irreversible damage containing the indent impression and varjous cracks propagating away from the indent [Evans, 1976a; Lawn, 1979]. The extent of indent impression and cracking is related to the elastic/plastic stress field beneath the indenter. This in turn is determined by the applied loads and the material properties [Lawn, 1980; Marshall, 1979]. Microindentation has long been used to measure the hardness of materials. Recently the use

of microindentation to measure the fracture toughness of brittle materials has been extensively studied [Evans, 1976b, 1979b; Marion, 1979; Niihara, 1982]. The most-often cited formulation was originally developed by Evans [1976b] and later modified by Niihara [1982]. Evans [1976b] conducted a dimensional analysis of the indentation fracture of a Vickers indenter and determined the relation between the fracture toughness (K_c) and the test parameters i.e. ;

$$K_c\phi / H\sqrt{a} = 0.48\ (c/a)^{-3/2} \qquad (2.33)$$

where ϕ is the plastic constraint factor ($\simeq 3$), H the hardness, a the impression radius and c the half median crack length. Eq. (2.33) can be used when the Young's modulus of a material is unknown but may result in $\simeq$ 30% error. Such an equation is too inaccurate for application. Niihara [1982] modified the approach by incorporating the observed Palmqvist cracks at lower loads in addition to the normal median cracks (Fig. 2.13). The Palmqvist cracks accounted for the discrepancy in Evans' results (Eq. 2.33). The final expressions for K_{Ic} were obtained by curve-fitting the experimental data, i.e.;

for Palmqvist cracks ($0.25 \leq l/a \leq 2.5$)

$$(K_{Ic}\phi / H\, a^{1/2})\ (H / E\,\phi)^{2/5} = 0.035\ (l/a)^{-1/2} \qquad (2.34a)$$

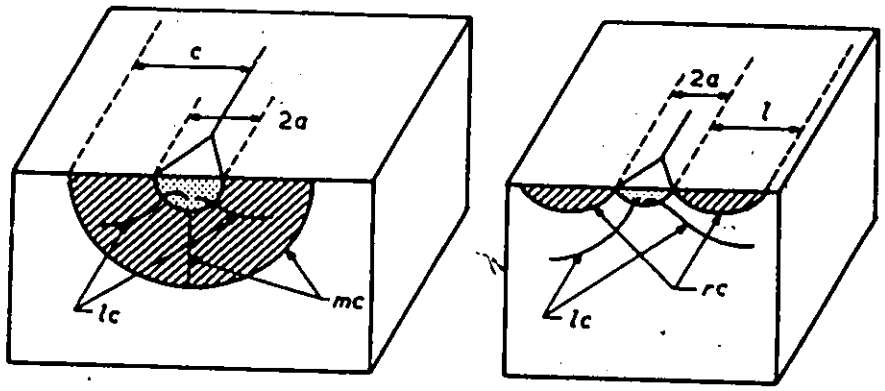

Fig. 2.13 Top and cross-sectional views of median, lateral and radial (Palmqvist) cracks, mc, lc, rc, respectively around Vickers indentation.

for median cracks ($c/a \geq 2.5$)

$$(K_{Ic}\phi / H a^{1/2}) (H / E \phi)^{2/5} = 0.129 (c/a)^{-1/2} \qquad (2.34b)$$

The microindentation technique is convenient for determination of fracture toughness at ambient temperatures. It is used to complement other techniques in the present study.

2.6. Summary of the Literature Issues and Statement of the Thesis Problems

The major issues which led to the present studies are as follows :

(1) the necessity for a systematic investigation of the strength improvement of a model ceramic via a colloid dispersion/sedimentation/burnout and the conventional dry pressing/isopressing/pressureless sintering route.

(2) the characterization of the flaw-strength relationship via an appropriate crack extension model and exploration of the relative severity of the fracture-initiating defect types.

(3) the exploration of the influence of residual stresses around inclusions on the strength of their ceramic matrices. The associated thermal contraction mismatch and elastic mismatch is analyzed using the weight function method.

(4) the verification of the existence of residual stresses associated with the defects in ceramics.

(5) the study of an agglomerate-initiated fracture model for ceramics.

(6) the development of an improved precracking technique for valid K_{Ic} determination using a chevron-notched bend bar.

Some minor issues added are ;

(1) the use of the sediment volume test for 4.5 wt% Y-PSZ powders in aqueous and organic solutions.

(2) the annealing of surface residual stresses resulting from the grinding of tetragonal zirconia.

(3) the experimental and theoretical acquisition of T_g data for tetragonal zirconia.

(4) justification of the application of the crack extension model to fracture-initiating defects in ceramics.

(5) an investigation of the effect of the displacement speed on subcritical crack growth in chevron-notched bend-bars.

These topics are organized into eight chapters, five on experimental procedures and their results, two on theoretical treatments and the last chapter on conclusions.

CHAPTER 3

Strength Improvement of Yttria-Partially-Stabilized-Zirconia by Flaw Elimination

3.1 Introduction

Y_2O_3-partially-stabilized zirconia (Y-PSZ) has extraordinary mechanical properties at ambient temperature. It has been found that the flexural strength depends on the processing route, being higher for hot-isostatically-pressed or slip-cast material and lower for materials synthesized by conventional sintering (Ch. 2.4). Elastic brittle materials like Y-PSZ have a strength correlatable with fracture origin defect size so increased flexural strength can be attained by eliminating or reducing the size of these defects (Ch. 2.1.1). Sedimentation eliminates hard agglomerates and solid inclusions. Burnout of green shapes followed by re-isostatic pressing eliminates residual porosity associated with organic inclusions (Ch. 2.2). It should be feasible to synthesize superior-strength materials by modifying the conventional dry pressing/isopressing/pressureless sintering routes by these defect elimination techniques.

Flaw/strength relationships for ceramics have been extensively studied. These relationships are considered an adequate means of investigating the response of defects to

the elimination techniques. Various models of crack extension from defects have been developed, refined and applied (Ch. 2.1.1). A part-through elliptical crack model is used in the present study.

The different defect types in a 4.5 wt% Y-PSZ are examined and their response to elimination techniques investigated. The consequent improvement of flexural strength and precise characterization of the correlations between the fracture stress and the fracture origin size are undertaken.

3.1 Analytical Procedure

The part-through elliptical crack model was used to characterize the correlation between the fracture stresses and fracture origin sizes. By rearranging Eq. (2.7) the resulting relationship is ;

$$\sigma_f \cdot \frac{Y\sqrt{a}}{\Phi} = \frac{K_{Ic}}{\sqrt{1-\nu^2}} = \text{constant} \qquad (3.1)$$

i.e. a plot of σ_f v.s. $Y\sqrt{a}/\Phi$ should give a curve characterized by constant K_{Ic}. The fracture-stress-related fracture origin size includes not only the simple dimension of the crack but the geometrical parameter, Y, and the shape parameter, Φ . "$Y\sqrt{a}/\Phi$" is therefore termed the "equivalent fracture origin dimension" in the present study.

The above model was applied to the data and fracture stresses were calculated as the actual stresses applied to the fracture origins. For subsurface origins this involved measuring the distance from the centre of the fracture origins to the tensile surface of the specimens and correcting fracture stresses accordingly. The variation of the fiber stress across the origins was neglected due to their relatively small dimension. The equivalent fracture origin dimension, $Y\sqrt{a}/\Phi$, was calculated from observed or approximated elliptical shapes. Non-elliptical fracture origins were approximated by the closest elliptical shape with an area equal to that of the origin. The projection of the semi-minor axis parallel to the tensile surface was chosen as the crack dimension. This is a compromise between the ideal Irwin model and Bansal's modification thereof (Ch. 2:1.1). Φ was calculated from the a/c ratios and Y values were determined by the location of the fracture origins. 1.94 was used for semi-elliptical shapes and 1.77 for completely elliptical shapes (Ch. 2.1.1). Values between 1.77 and 1.94 were assigned to shapes between these extremes (maximum error of $\simeq$ 5%).

3.3 Experimental Procedure, Results and Discussion

4.5 wt% Y-PSZ submicron powder[4] was used as the starting material. The 4.5 wt% (2.5 mol%) Y_2O_3 content is in the range reported to give optimum flexural strength values (Ch. 2.4). The powders were dry-pressed[5] in a steel die at 40 MPa and isostatic-pressed[6] at 300 MPa. The compacts were then pressureless-sintered[7] in air using the schedule shown in Fig. 3.1. 99.5%-theoretically dense sinters were obtained after firing at 1400°C for 3 hours at a heating rate of 215°C/hr. This density is close to that produced by hot isostatic pressing and is necessary to minimize large pore fracture origins (Ch. 2.4).

The sintered bodies were examined by XRD (CuKα) between $2\theta = 28^\circ$ and 36° as shown in Fig. 3.2(a). The tetragonal phase (111), (002) and (200) peaks at $2\theta \simeq 30.5^\circ$, 35° and 35.5° respectively are evident. No monoclinic phase ($(11\bar{1})$ and (111) peaks at $2\theta \simeq 28.3^\circ$ and 31.7°) were detected and no cubic phase ($2\theta \simeq 30^\circ$ and 35°) is present. The sintered body was the ≃ 100% tetragonal phase, necessary for optimum strength (Ch. 2,4). The sintered body was ground

---

4. Zircar Inc. Florida, NY., U.S.A.

5. Carver, Wis. U.S.A.

6. Autoclave, Pa. U.S.A.

7. C.M. Co., NY. U.S.A.

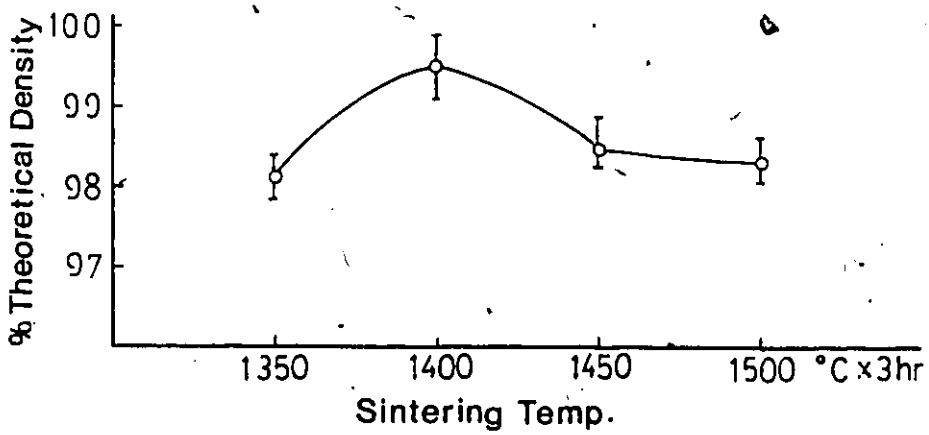

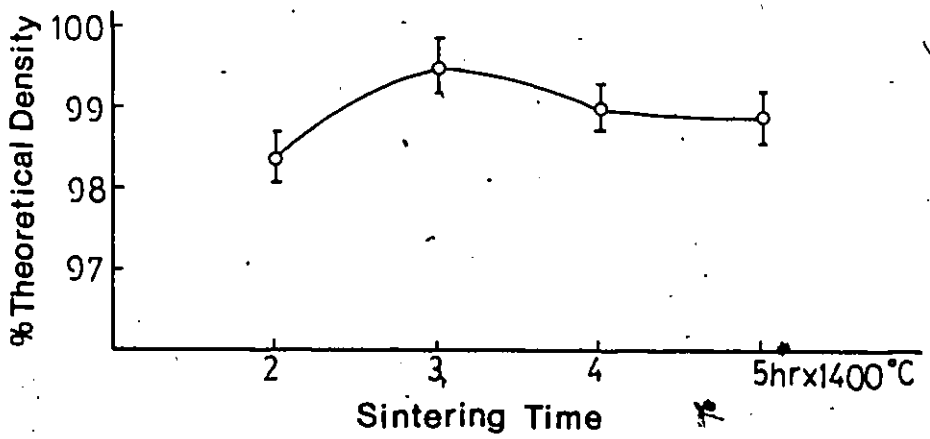

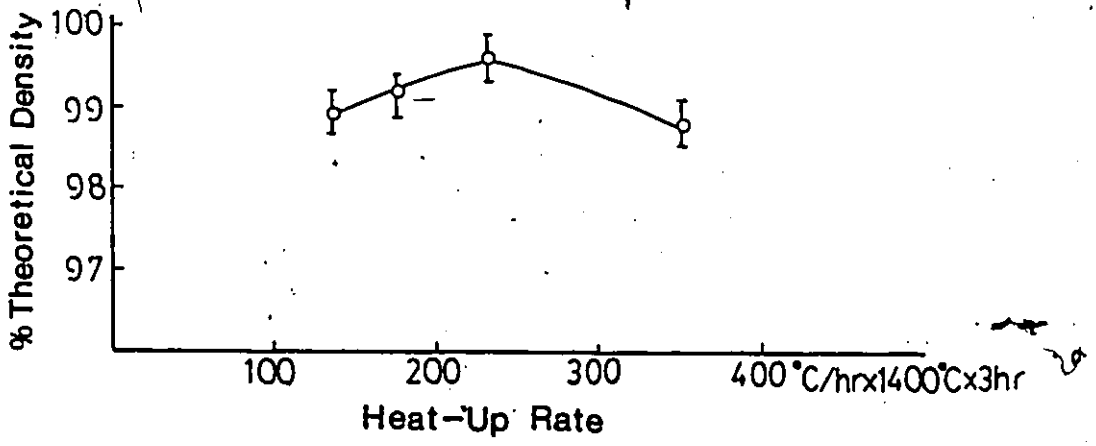

Fig. 3.1 Sintered density v.s. sintering schedule for 4.5 wt% Y-PSZ.

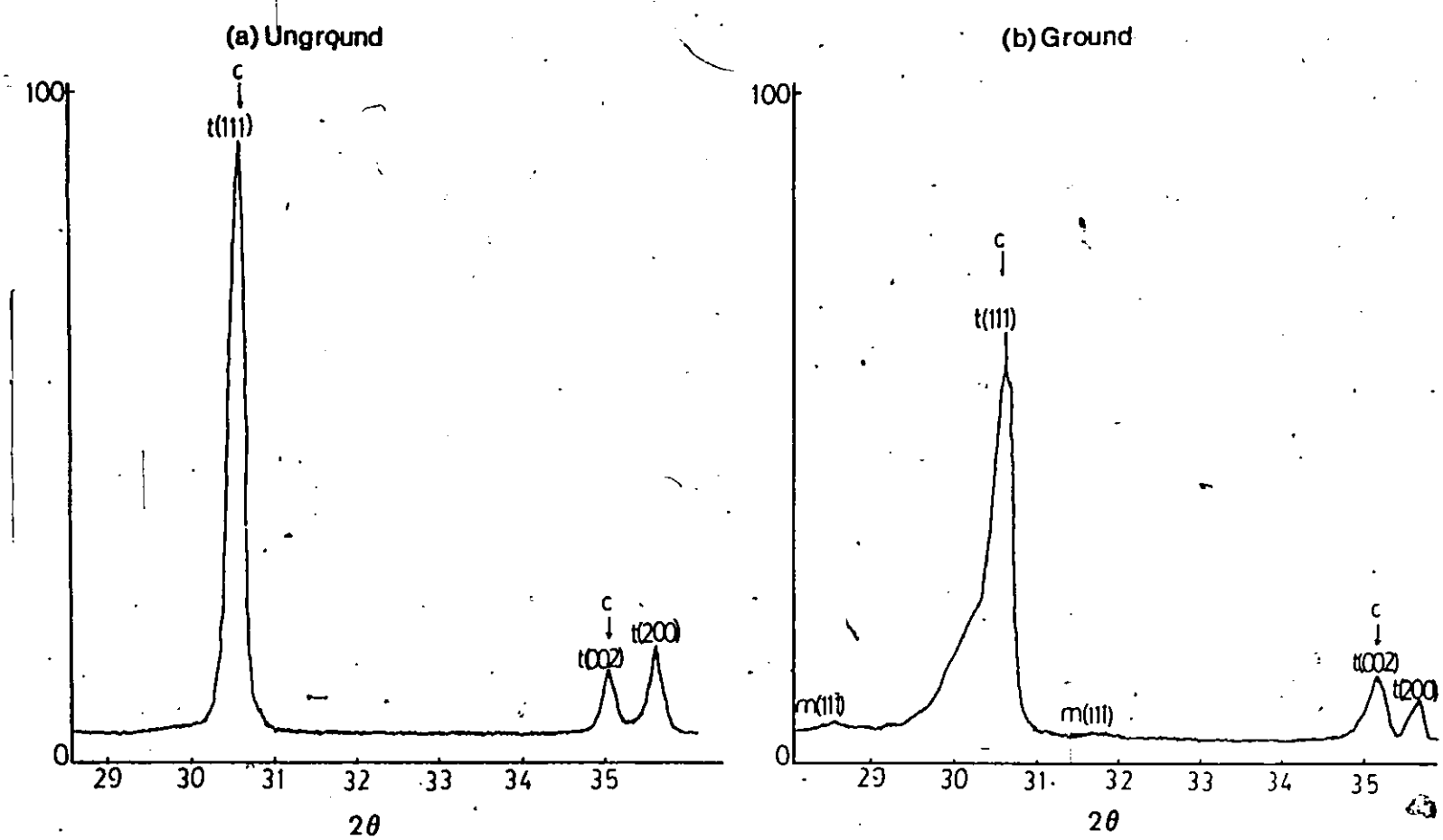

Fig. 3.2 X-ray diffraction of 4.5 wt% Y-PSZ (a) as sintered (b) surface ground (320 grits).

and polished to 1 μm, etched with dilute HF[8] and examined in the SEM[9]. The average grain size was ≈ 0.1 μm (Fig. 3.3), well below the critical size required for full retention of tetragonal phase (Ch. 2.4).

The sintered plates were cut into bars, ground and edge-chamfered to final dimensions, 25 x 2 x1.5 mm. The bars were four-point-bend tested with an inner span of 10 mm and an outer span of 20 mm. The specimen dimensions, finishing procedure, test fixture design and test procedure all conformed with the American Standard MIL-STD-1942(MR) (Ch. 2.5.1). A specially designed adjustable sample holder (Fig. 3.4) was used to set the relative position of the specimen and test fixture with an accuracy of ± 0.03 mm. The design was such as to avoid identified sources of testing error (Ch. 2.5.1).

During surface finishing of the test bars, the surface tetragonal phase can transform to monoclinic and the resultant compressive residual stress can strengthen the material (Ch. 2.4). As this was undesirable, a thermal recovery procedure was developed. A ground test bar (325 grit) was first examined by XRD (Fig. 3.2(b)). The tetragonal (111) peak is lower and broader than that of the

---

8. BDH, ON. Canada.

9. Philips 515.

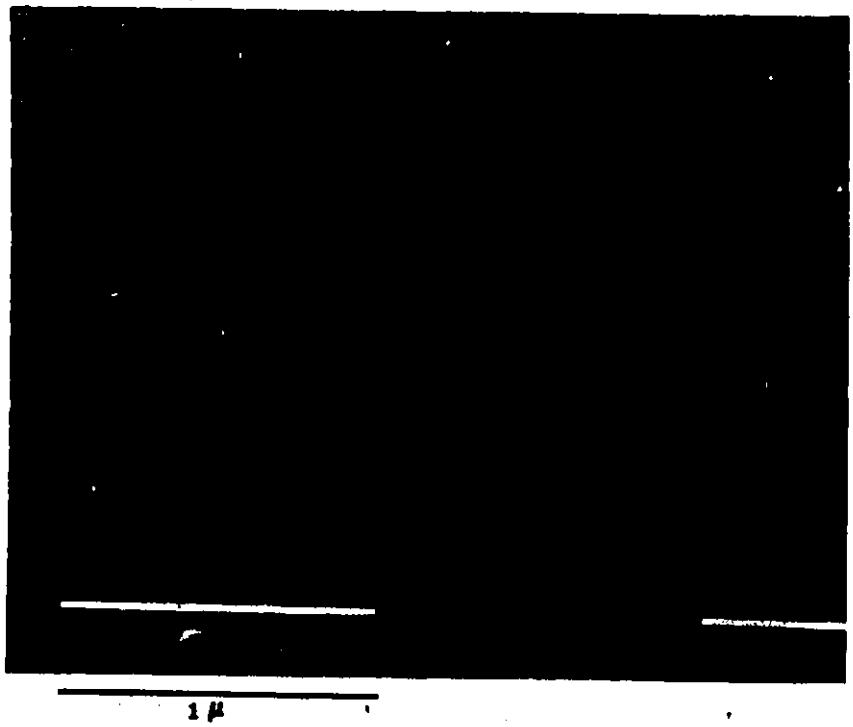

(a)

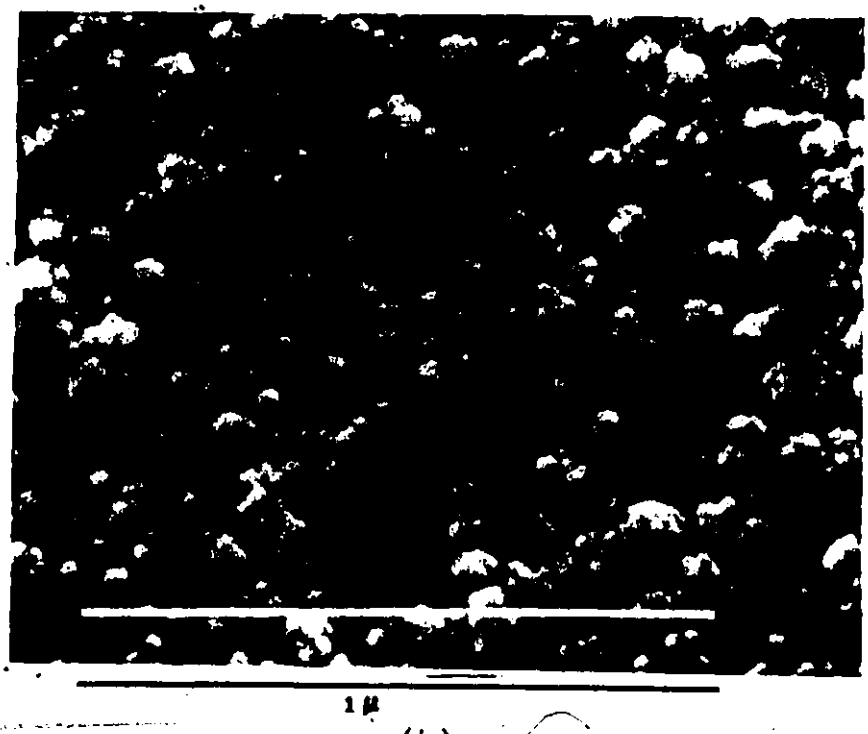

(b)

Fig.3.3 Microstructure of sintered 4.5 wt% Y-PSZ (a) low (b) high magnification, showing average grain size ≈ 0.1 μm.

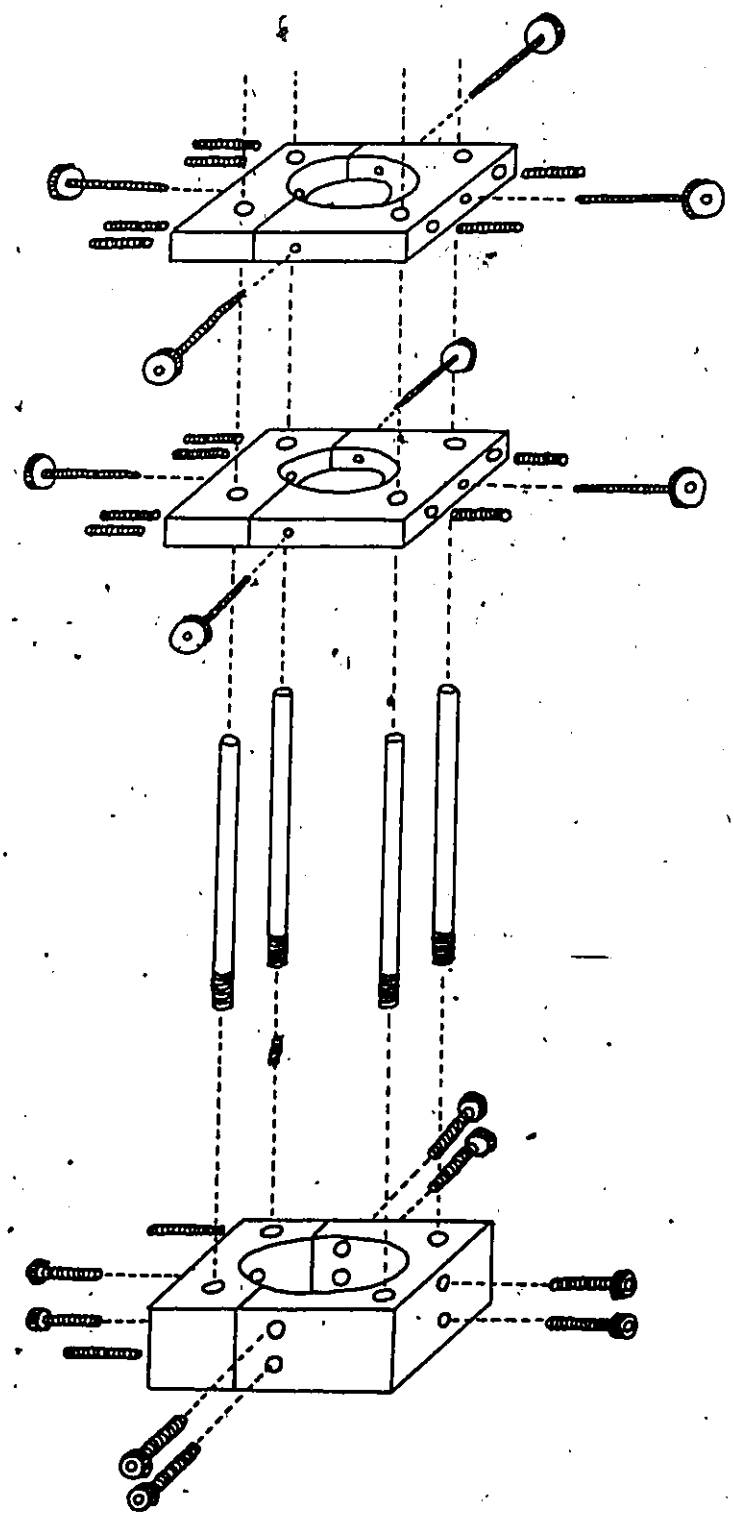

Fig. 3.4 Design drawing of the adjustable sample holder.

unground material (Fig. 3.2(a)). It also shows some low-angle asymmetry, indicating the influence of the monoclinic $(11\bar{1})$ peak. There is also traces of a monoclinic-phase peak at $2\theta \propto 28.3^{\circ}$. The height and width of the tetragonal (111) peak was used to indicate the extent of annealing recovery. The ground test bars were thermally treated between 500 and 1400°C for 0.5 hr and the height of the tetragonal (111) peaks were recorded as shown in Fig. 3.5. It is clear that annealing at 1400°C for 0.5 hr is sufficient to retransform the monoclinic phase and relieve the residual stress.

The experimental device used for bend testing is shown in Fig. 3.6. This device is also designed for the high-temperature test (Ch. 5 and 7). The test specimen is placed between the upper and lower fixtures and then loaded via the push rod and support post connected to a load cell[10] and attached to the machine crosshead. The testing machine is a compression type of capacity 5000 Kg[11]. The fixture has inner span, 10 mm, and outer span, 20 mm. The fixtures, push rod and upper part of the support tube are made of hot-pressed alumina[12] and the rollers are sapphire[13].

---

10. Kulite TC-2000-500, U.S.A.

11. Wykeham Farrance WF 10053, U.K.

12. McDanel, NJ. U.S.A.

13. Insaco, PA. U.S.A.

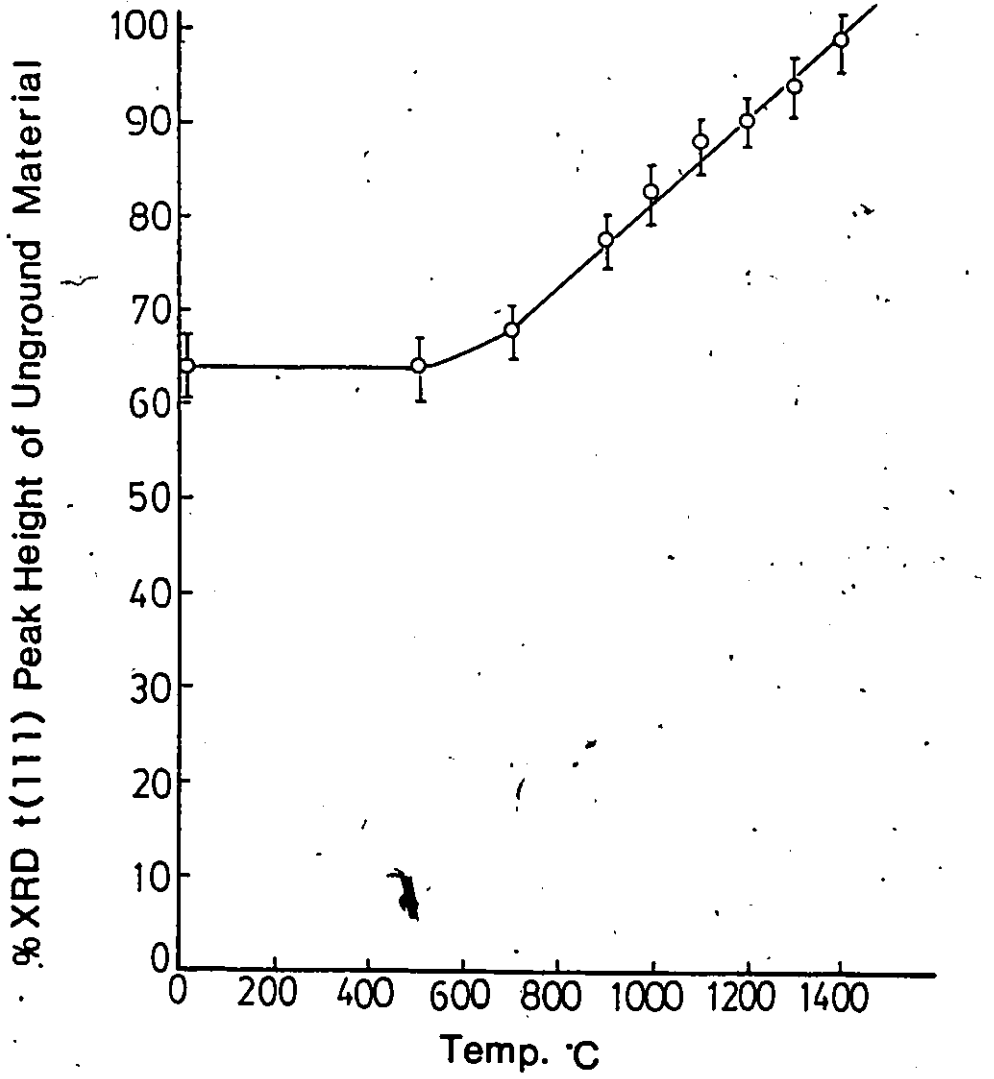

Fig. 3.5 Results of thermal recovery from ground surface of 4.5 wt% Y-PSZ (320 grit).

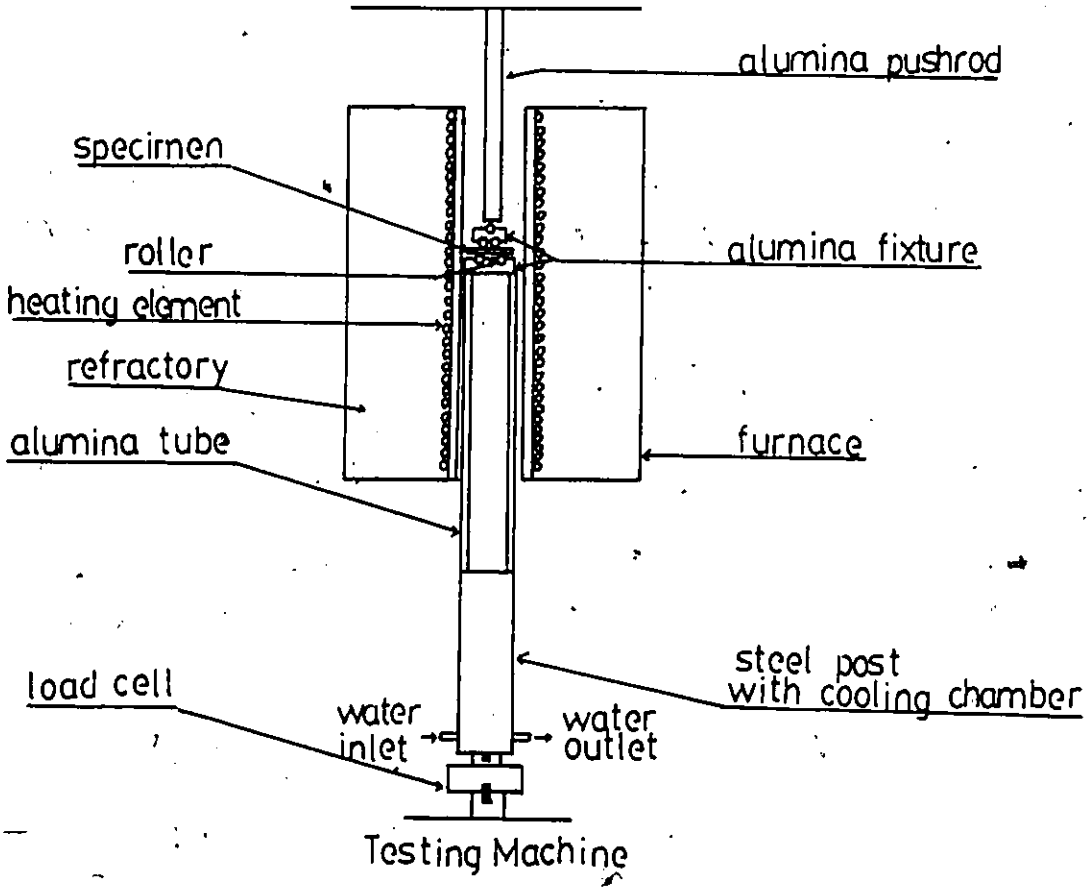

Fig. 3.6 Experimental set-up for four-point-bend test.

3.3.1 Fracture of Sinters of the As-Received Powders

The flexural strength of samples made from the as-received powders is plotted in the Weibull plot of Fig. 3.7. Values ranged between 650 and 1020 MPa, with an average of 880 MPa and a Weibull modulus of 12.3. These results are similar to those of previous studies (Ch. 2.4). Both fracture surfaces of each test bar were examined optically at 80 X and the approximate location of the fracture origins recorded. Representative half specimens were then sputter-coated with gold and examined by SEM at 25 KeV. The exact shape and dimensions of the fracture origins were thus obtained. Inclusion-type fracture origins were further analyzed by EPMA to identify their composition. Five types of fracture origin were classified as shown in Fig. 3.8 to 3.12 (KV : SEM voltage in 1000 volts; KX = 1000X magnification; bar unit is μm). Type A origins (Fig. 3.8) are regularly-shaped elongated pores. These pores are cavities left by fiber-shaped inclusions after burn off. These were termed "fiber inclusions". No chemical information could be obtained by EPMA. These pores act as fracture origins. Type B origins (Fig. 3.9) are aggregates of large grains centered in pore- or crack-like cavities surrounded by a matrix of smaller grains. These defects were associated with original powder "agglomerates" (Ch. 2.1.2). Differential sintering of these agglomerates leads to this defect morphology (Ch. 2.3.1). The associated cavities act

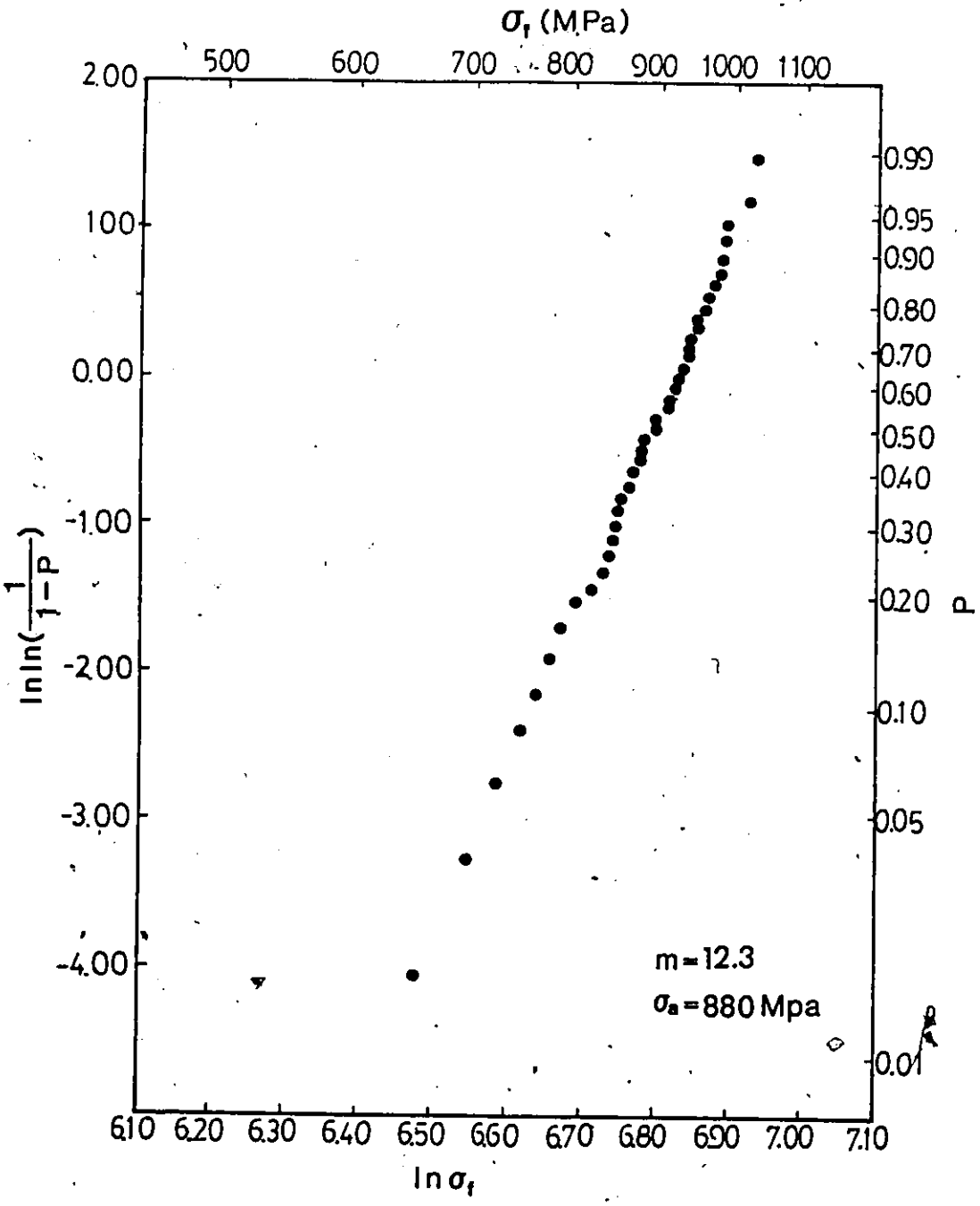

Fig. 3.7 Weibull plot of the flexural strength of samples made from the as-received powder.

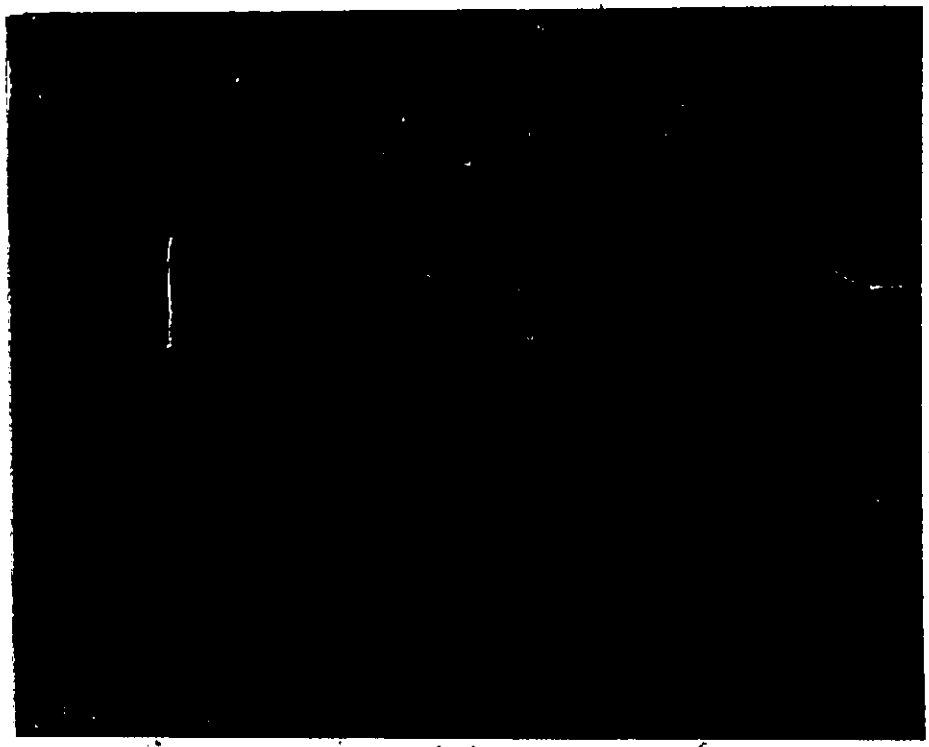

(a)

(b)

Fig. 3.8 Type A fracture origin - fiber inclusion (a) low magnification (b) high magnification.

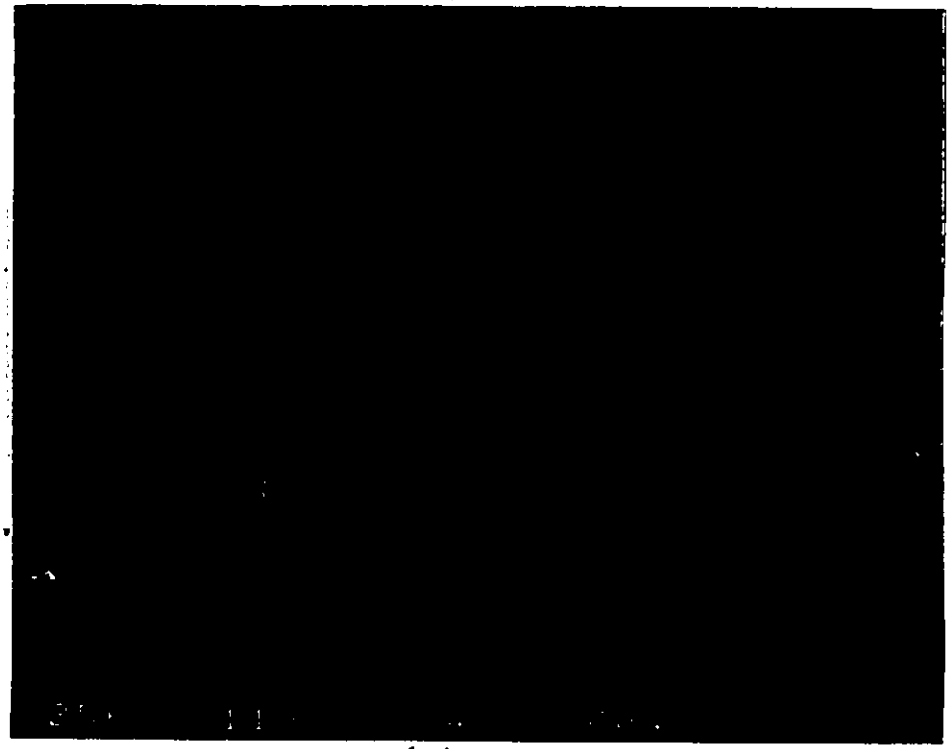

(a)

(b)

Fig. 3.9 Type B fracture origin - agglomerate (a) low magnification (b) high magnification.

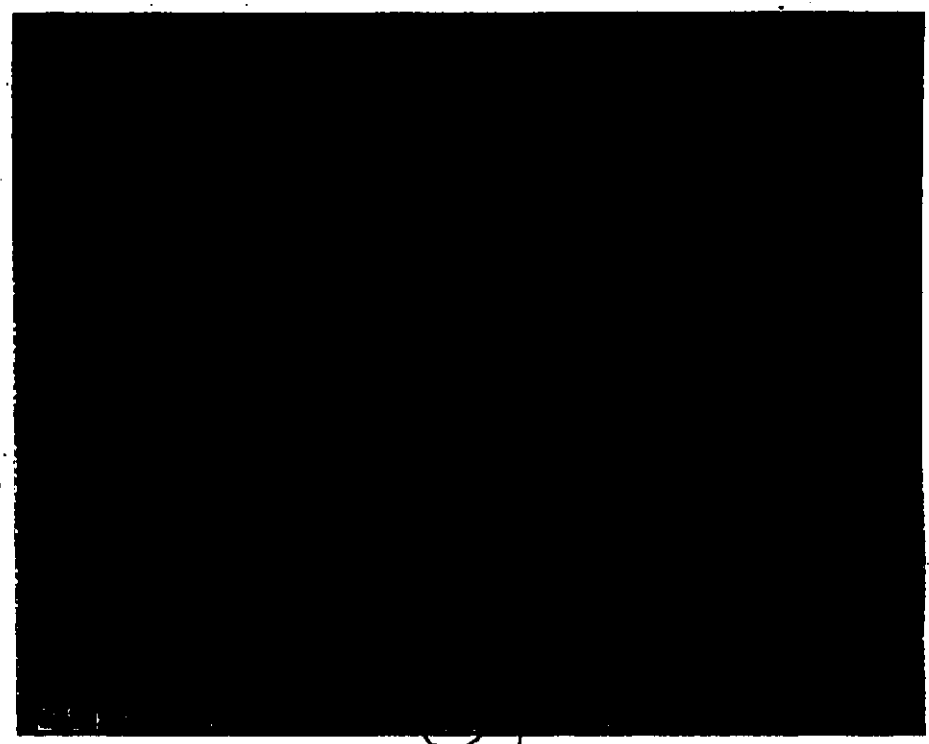

(a)

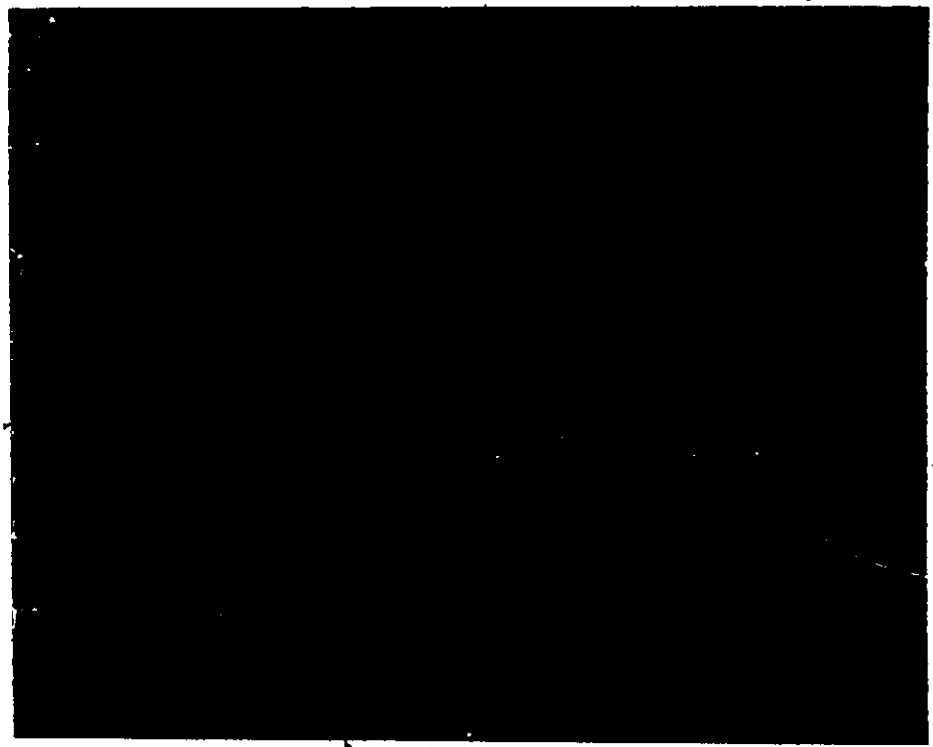

(b)

Fig. 3.10 Type C fracture origin - iron inclusion (a) low magnification (b) high magnification.

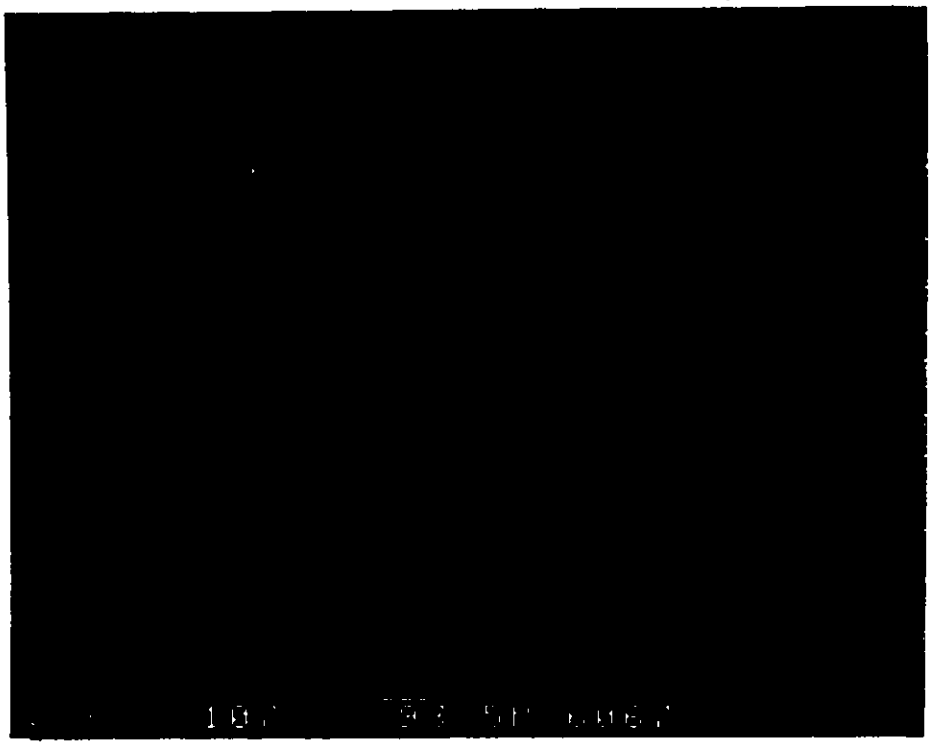

(a)

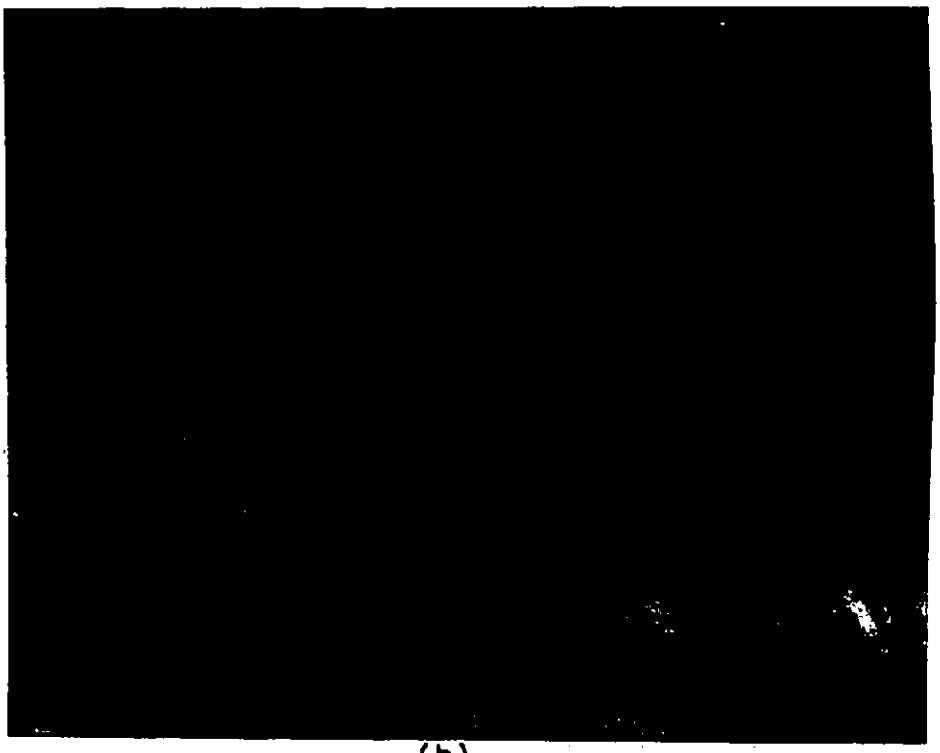

(b)

Fig. 3.11 Type D fracture origin - alumina inclusion (a) low magnification (b) high magnification.

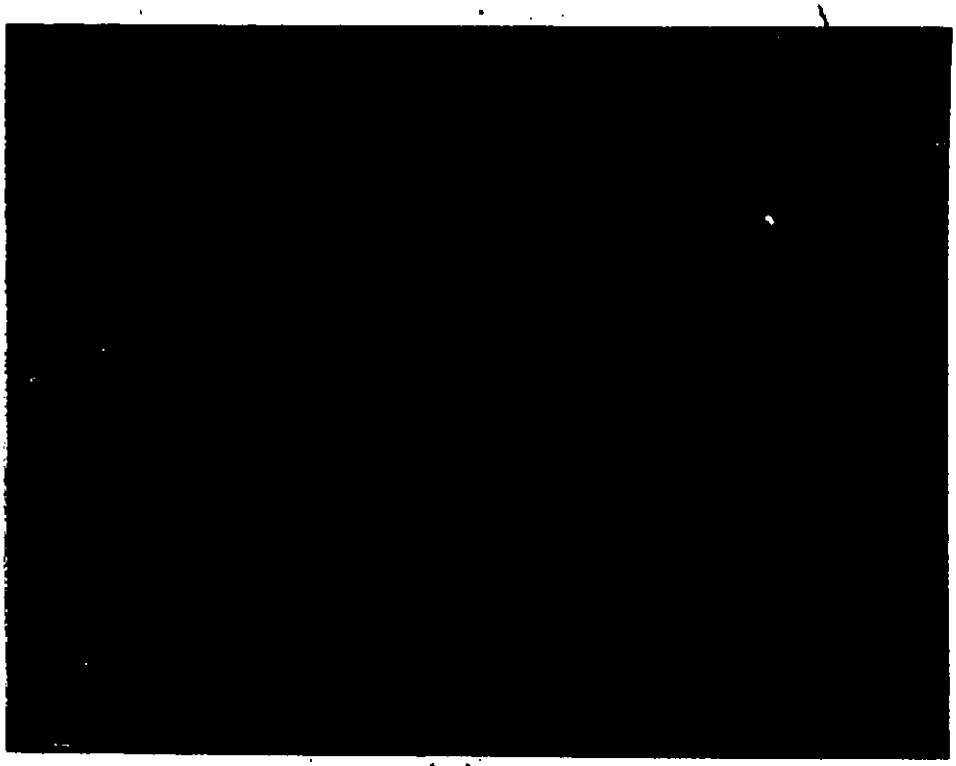

(a)

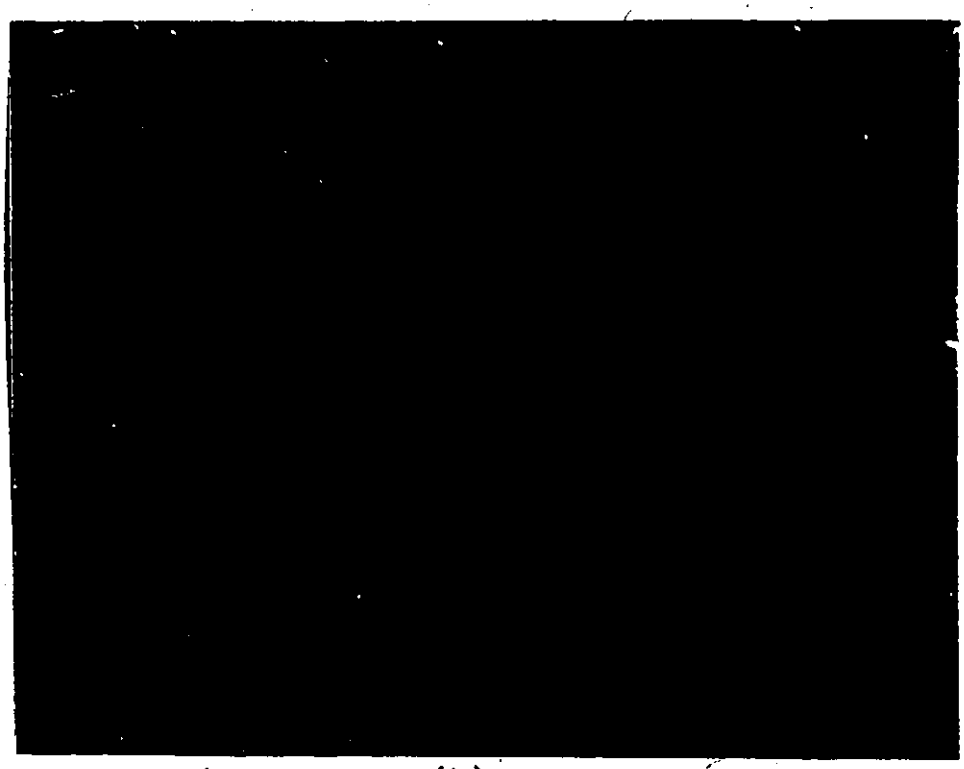

(b)

Fig. 3.12 Type E fracture origin - pore (a) low magnification (b) high magnification.

as fracture origins. Type C origins (Fig. 3.10) are nearly round or elliptically shaped dark regions of porous undiscernible grains. EPMA examination revealed appreciable levels of iron so these were termed "iron inclusions". It is thought that iron particles in the compacted powder melted and oxidized at sintering temperatures and penetrated the local matrix. The impregnated zirconia grains then sinter abnormally leaving porous region with visually undiscernible grains. These porous regions had less coherency than the matrix and so act as fracture origins. Type D origins (Fig. 3.11) are large regions of irregular shape elongated along the surface direction. They appeared dense and coherent with the local matrix. EPMA detected aluminum indicative of alumina and were termed "alumina inclusions". Although these inclusions appeared coherent, their fracture toughness is lower than the zirconia matrix. Cracks could initiate from these region. Type E origins (Fig. 3.12) are pores left after processing or developed during sintering. These could act as natural fracture origins.

To apply the crack model to the present fracture origin types, size equivalence of the defects and the corresponding flaws must exist (Ch. 2.1.1). The resulting equivalence is considered to hold for the five fracture origin types. The observed fiber inclusions, agglomerates and pores had well-defined cavity boundaries. Iron inclusions act in a similar fashion to pores. As for

alumina inclusions, there is no evidence of radial cracking. Interfacial cracking or inclusion fracture justifies use of the crack model (Ch. 2.1.1). Experimental verification of Al_2O_3 inclusion-fracture will be given in Chapter 6. A corresponding inclusion-fracture model is proposed in Chapter 8.

The correlation between fracture stress and fracture origin dimension for the sinters of as-received powders was established via the $\sigma_f - Y\sqrt{a}/\Phi$ plot shown in Fig. 3.13. The results approximately follow the prediction of Eq. (3.1) for each fracture origin type. Three distinct groups are revealed i.e., A and B types are the most-severe group, C and E intermediate and D type the least severe. These data indicated a good correlation between the fracture stress and the equivalent fracture origin dimension. There is a discernible order-of-severity for the fracture origins which could serve as a priority guide for defect elimination. Agglomerate defects were responsible for the largest strength degradation. Some were 60 μm diameter and resulted in flexural strength values as low as 650 MPa. Efforts were first made to eliminate them.

3.3.2 Fracture of Sinters of Sedimented, As-Received Powders

Sedimentation has been used to remove agglomerates from ultrafine ceramic powders (Ch. 2.2.1). On dispersion in liquid media, the "soft" agglomerates disintegrate and the

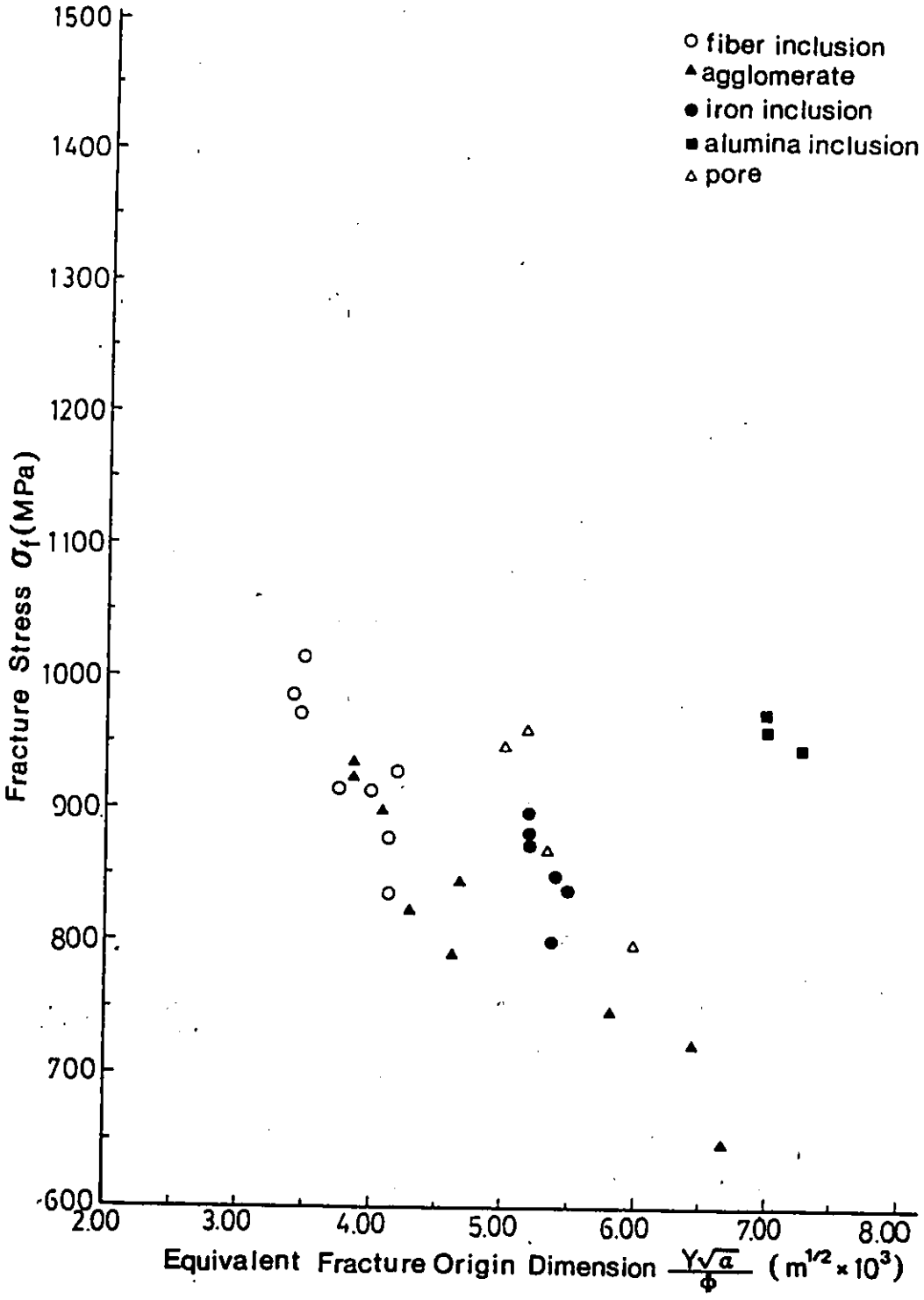

Fig. 3.13 $\sigma_f - Y\sqrt{a}/\Phi$ plot for samples made from the as-received powder.

"hard" agglomerates sediment out. Sedimentation behavior is characterized by Stoke's law following correction for non-sphericity and non-infinitely dilute suspension (Appendix B). In the present study, the correction factor (F) (in Eq. (B.7)) was obtained experimentally by comparing the observed sizes of the agglomerate-fracture-origins with the calculated ones. Successful sedimentation needs an appropriate dispersion medium (Ch. 2.2.1). In the present study, the dispersion efficiency of the tetragonal zirconia powders in various media was determined via the sediment volume test (Ch. 2.2.1). Dispersion media representative of several chemical groups were used. These were 2-propanol[14], methanol[15], acetone[16], 1-butanol[17], water pH-2[18], water pH-7, n-Hexane[19] and propionic acid[20]. Their physical properties are listed in Table 3.1.

---

14. Fisher Certified A.C.S., N.J. U.S.A.

15. Caledon HP grade, ON. Canada.

16. BDH assured, Canada

17. Fisher certified A.C.S., N.J. U.S.A.

18. Sulfuric acid : Baker NJ. U.S.A.

19. Caledon reagent grade, ON. Canada.

20. Fisher, NJ. U.S.A.

Table 3.1 Physical properties of the dispersants

Liquid	Dielectric constant	Surface tension v-l (mN/m)	Boiling point(°C)	Viscosity (cP)
2-Propanol	18.3	21.3	82.4	2.86
Methanol	32.6	22.5	65	0.597
Acetone	20.7	25.1	56.2	0.316
1-Butanol	-	-	117.0	-
Water	78.5	72.75	100.0	1.002
n-Hexane	1.89	18.4	69.0	0.326
Propionic acid	3.3	26.7	141.0	1.10

2-propanol and methanol are alcohols. These have been reported to have excellent dispersion properties for oxide powders (Ch. 2.2.1). Acetone is a ketone and 1-butanol an alcohol. They are commonly-used chemical agents with ceramic powders and show no chemical reaction. Water, both acid and neutral, has been reported to give good results (Ch. 2.2.1). n-Hexane is a hydrocarbon with negligible polarity and propionic acid is an acid. These were included for comparison. The dispersive ability of the former is expected poor whilst the latter should be good (Ch. 2.2.1). The test results are shown in Fig. 3.14. The best dispersions were obtained in water pH-2, methanol, water pH-7 and 2-propanol. These results conform with their physical properties (Ch. 2.2.1). Amongst the good dispersants, methanol and 2-propanol have strong hydrogen bonds, relatively high dielectric constants and low surface tension. Methanol has a

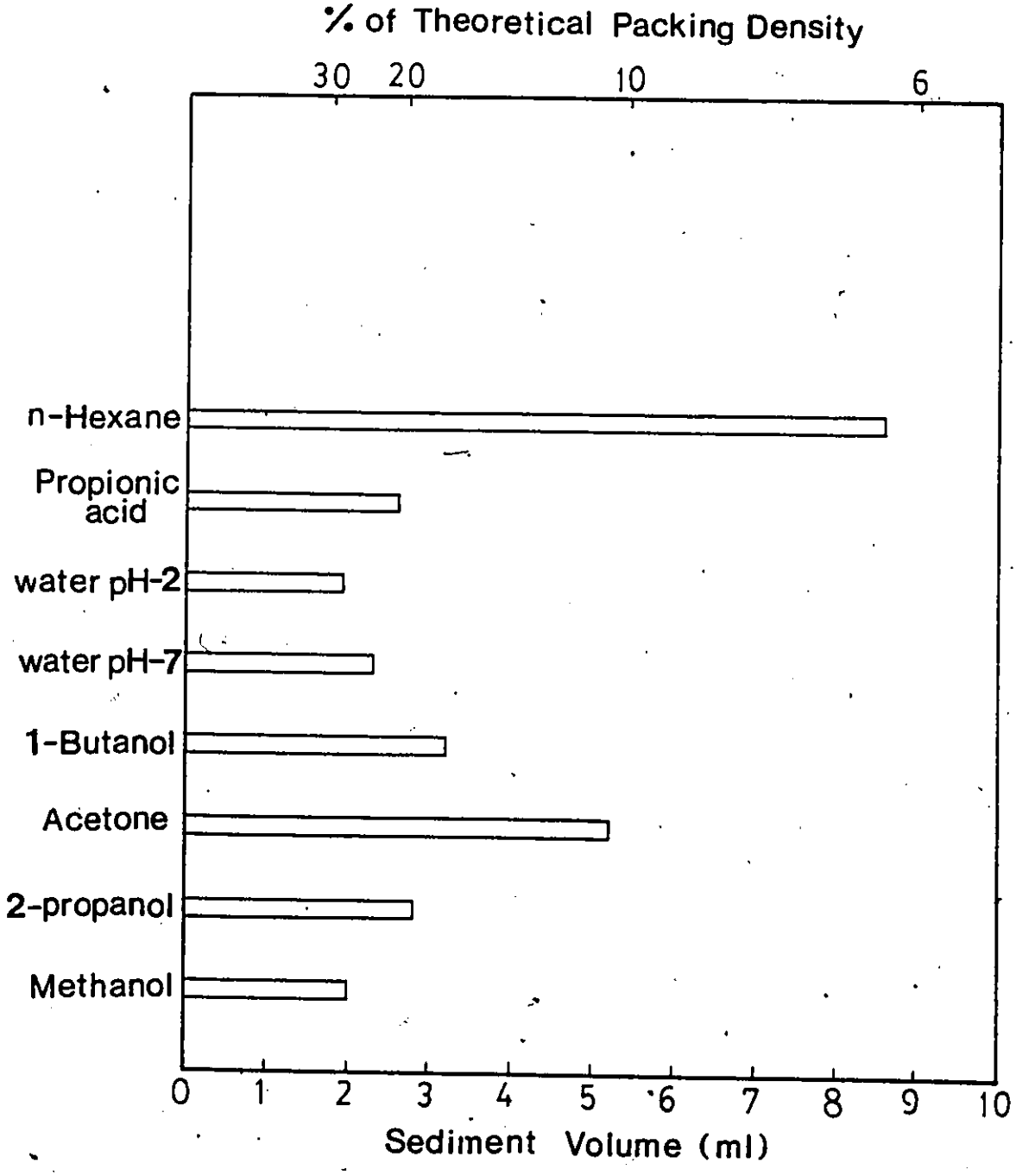

Fig. 3.14 Results of the sediment volume test for 4.5 wt% Y-PSZ.

a higher dielectric constant than that of 2-propanol. These were reflected in the results. Water has strong hydrogen bonds and a high dielectric constant. However its high surface tension may cause wetting difficulty. To use water a pre-wetting and pre-dispersion procedure may be necessary. Little difference existed between water pH-2 and pH-7, indicating the ZPC for tetragonal zirconia is ≃ pH-5, consistent with a theoretical prediction [Woods, 1988c]. Other media did not have good dispersive ability owing to low dielectric constant or lack of hydrogen bonding. The sediment volume test is semi-quantitative in nature (Ch. 2.2.1) and the results were only used to screen out unsuitable media. The best four dispersants were further examined by the sedimentation test. Calculations (Appendix C) showed that 2-propanol is the media most suitable when the target particle size to be eliminated is large and the sedimentation time is long. A previous study showed that Stoke's law is applicable to this medium with the least correction [Parish, 1984]. 2-propanol was therefore examined first in the present study.

To accurately calculate the sedimentation time for removal of target defects, the powders must be well dispersed and start settling at the same time. This is a problem for high-surface-tension liquids or highly agglomerated dry powders. Powders must therefore be pre-wetted and pre-dispersed before starting sedimentation. In

the present study the as-received Y-PSZ powders were ultrasonically agitated[21] in a 4 vol% suspension of the same dispersant for 30 minutes. The dispersed suspension was then slowly poured into the bulk dispersant in a 500 ml beaker of 10 cm height and settled for the time calculated via the corrected Stokes' law.

(1) 2-Propanol Sedimentation

Close examination of Fig. 3.13, reveals that the fracture-initiating agglomerates had an equivalent dimension $> \simeq 4 \times 10^{-3}\ m^{1/2}$, or an equivalent spherical diameter (D_m) of $\simeq 20\ \mu m$. These agglomerates were therefore targeted for removal. 4 vol% as-received powder was dispersed in 2-propanol, ultrasonically agitated and then poured into 2-propanol liquid and settled for a length of time determined via Stoke's law (F = 1, 1 hour). The supernatant was removed, centrifugally consolidated[22] and dried at 100°C for 24 hours. The dried cake was ground, pressed, isopressed and sintered (as per the as-received powder). The resulting flexural strength data are shown in the Weibull plot of Fig. 3.15. Fracture stresses ranged from 740 to 1280 MPa with an average value of 995 MPa. This is an improvement of 110 MPa over the as-received powder sinters (Fig. 3.7). The Weibull modulus was 10. The reasons for the improvement are

---

21. Branson, CN. U.S.A.

22. Damon/IEC, MA. U.S.A.

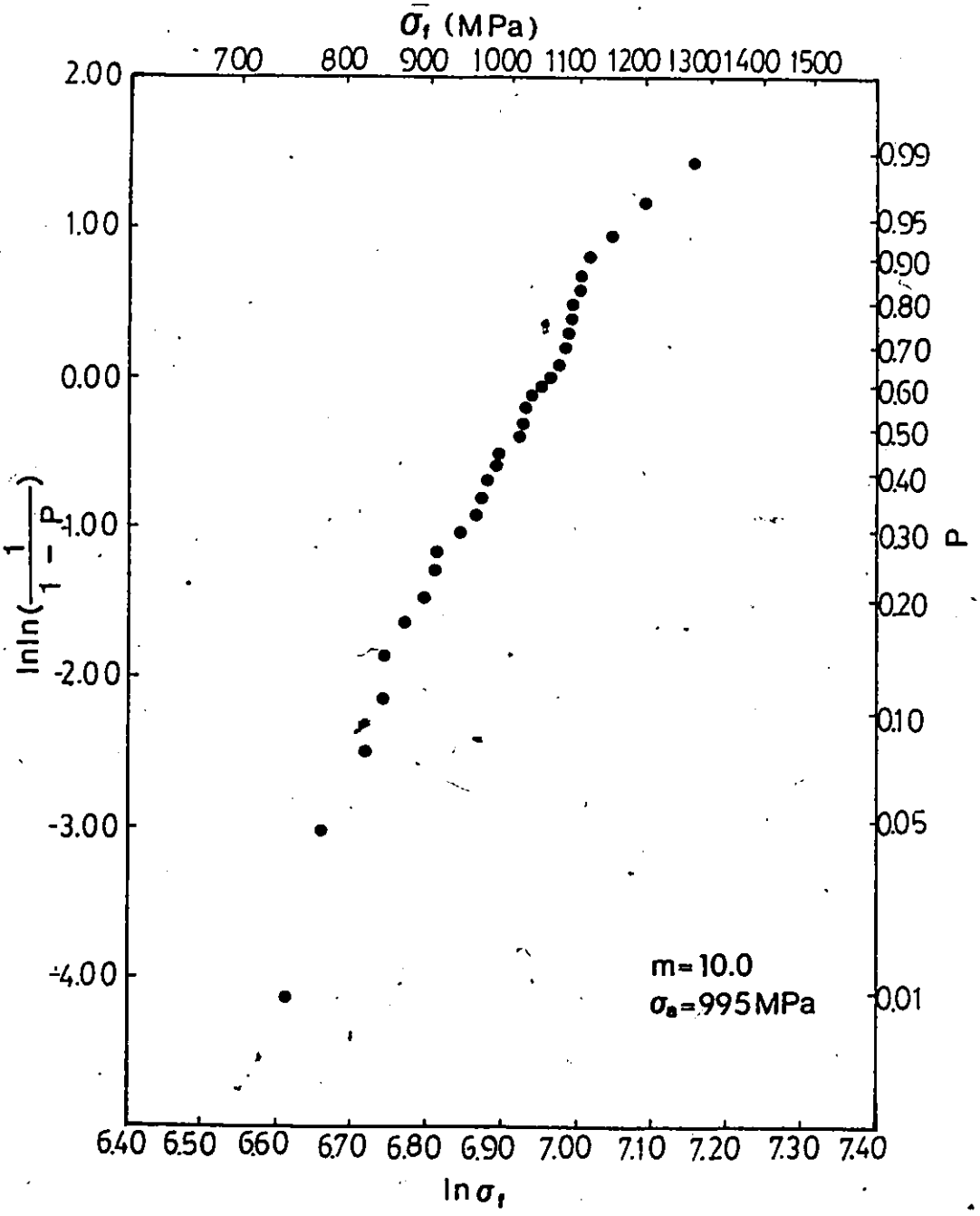

Fig. 3.15 Weibull plot for samples made from powder following 2-propanol sedimentation.

illustrated in the corresponding σ_f-$Y\sqrt{a}/\Phi$ plot of Fig. 3.16. Again three distinct groups of defect-severity emerge in the same order as before and are well described by Eq. (3.1). The observed agglomerate fracture origin are $< 4 \times 10^{-3}$ $m^{1/2}$ equivalent dimension, in good agreement with Stoke's law. The reduction of agglomerate size which accounts for $\simeq$ 50% of the fracture is the main reason for the improved flexural strength. Type-C iron and type-D alumina inclusions are also reduced in size. Using Stokes' law to calculate the sedimentation time for removal of the iron inclusions, sizes $\simeq$ 1.15 times larger than the agglomerates can be removed in the same time. This verifies the results of Fig. 3.16. The equivalent iron inclusion dimension was $< 4.5 \times 10^{-3}$ $m^{1/2}$ after sedimentation. The sedimentation time for type-D alumina inclusions cannot be calculated due to their irregular shape. Type-A fiber inclusions are uninfluenced by the sedimentation, suggesting their low density.

To reduce the agglomerate and iron inclusion sizes further, and eliminate the fiber inclusions, methanol sedimentation followed by burnout and re-isopressing was next investigated.

(2) Methanol Sedimentation, Burnout and Re-isostatic Pressing

Close examination of the data in Fig. 3.16 shows that reduction of agglomerates to very small sizes is unjustified since fiber inclusions and pores then become the

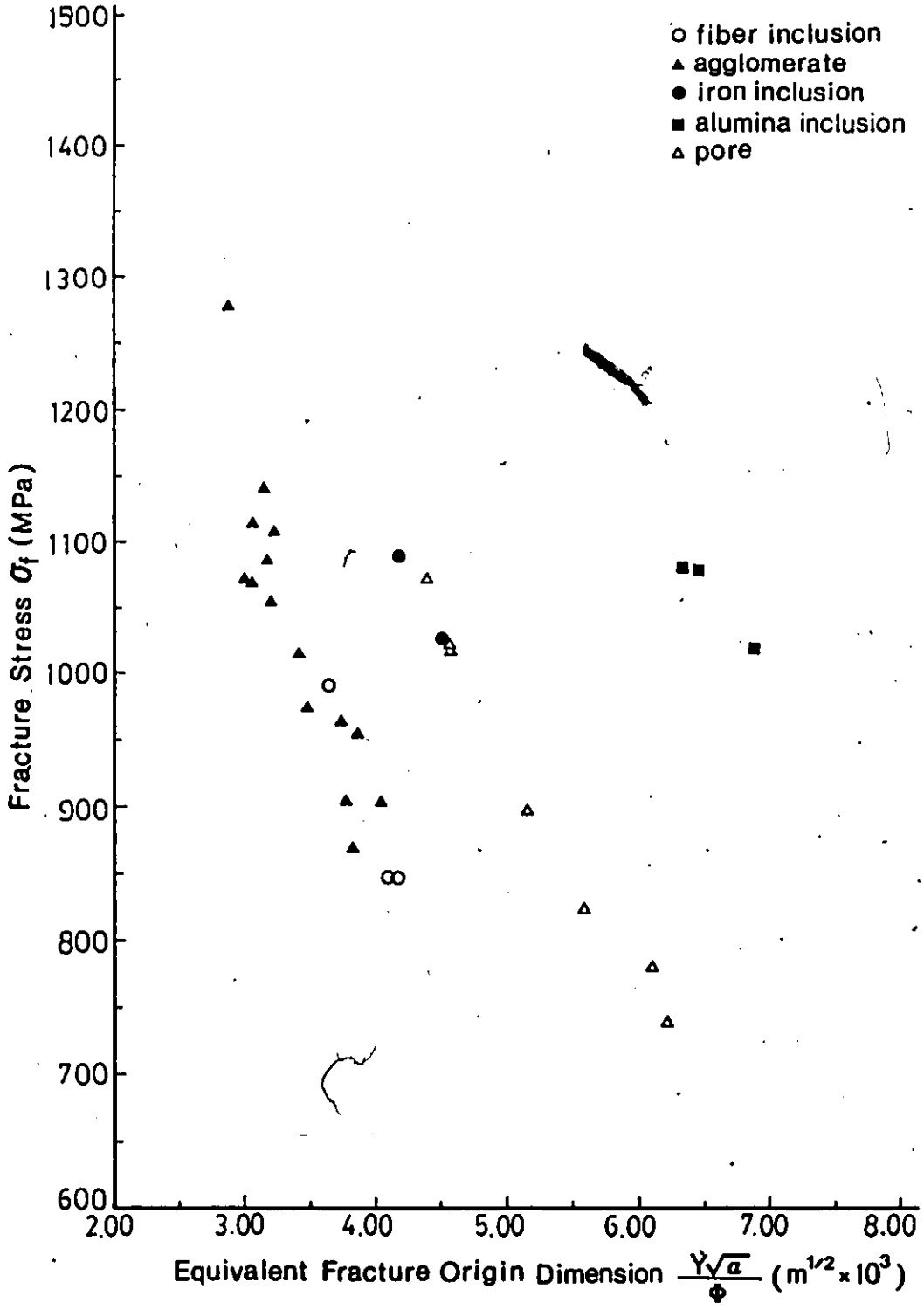

Fig. 3.16 $\sigma_f - Y\sqrt{a}/\Phi$ plot for samples made from powder following 2-propanol sedimentation.

dominant fracture-initiating defects responsible for low fracture stresses. The second target for sedimentation was therefore set at equivalent dimension $\simeq 3.5 \times 10^{-3}\ m^{1/2}$ for agglomerates and $\simeq 4 \times 10^{-3}\ m^{1/2}$ for iron inclusions, i.e. the elimination of agglomerates responsible for fracture stresses < 1000 MPa and the complete elimination of the iron inclusions. Methanol is suitable for this task (Appendix C). The fiber inclusions are materials of low density that do not survive sintering, i.e. organics (Ch. 2.1.2). Burnout followed by re-isopressing was used to remove these inclusions (Ch. 2.2.2). The as-received powders were settled in methanol (as per 2-propanol sedimentation) and the correction for Stokes' law was applied (F = 0.1, 5 hours). The resulting powders were then compacted, fired at 600°C for 24 hours and then re-isostatically-pressed at 300 MPa. The flexural strength data following sintering is shown in Fig. 3.17. The fracture stresses are from 820 to 1470 MPa with an average of 1150 MPa. The Weibull modulus is 10. The average fracture stress was increased by $\simeq$ 150 MPa over that following 2-propanol sedimentation. The reasons for strength improvement are revealed in the corresponding σ_f-$Y\sqrt{a}/\Phi$ plot of Fig. 3.18. The relative severity positions of the fracture origin types remain unchanged and are well described by Eq. (3.1). Type-A fiber inclusions were eliminated by burnout and re-isostatic pressing and their disappearance leads to competition between type-B and -E

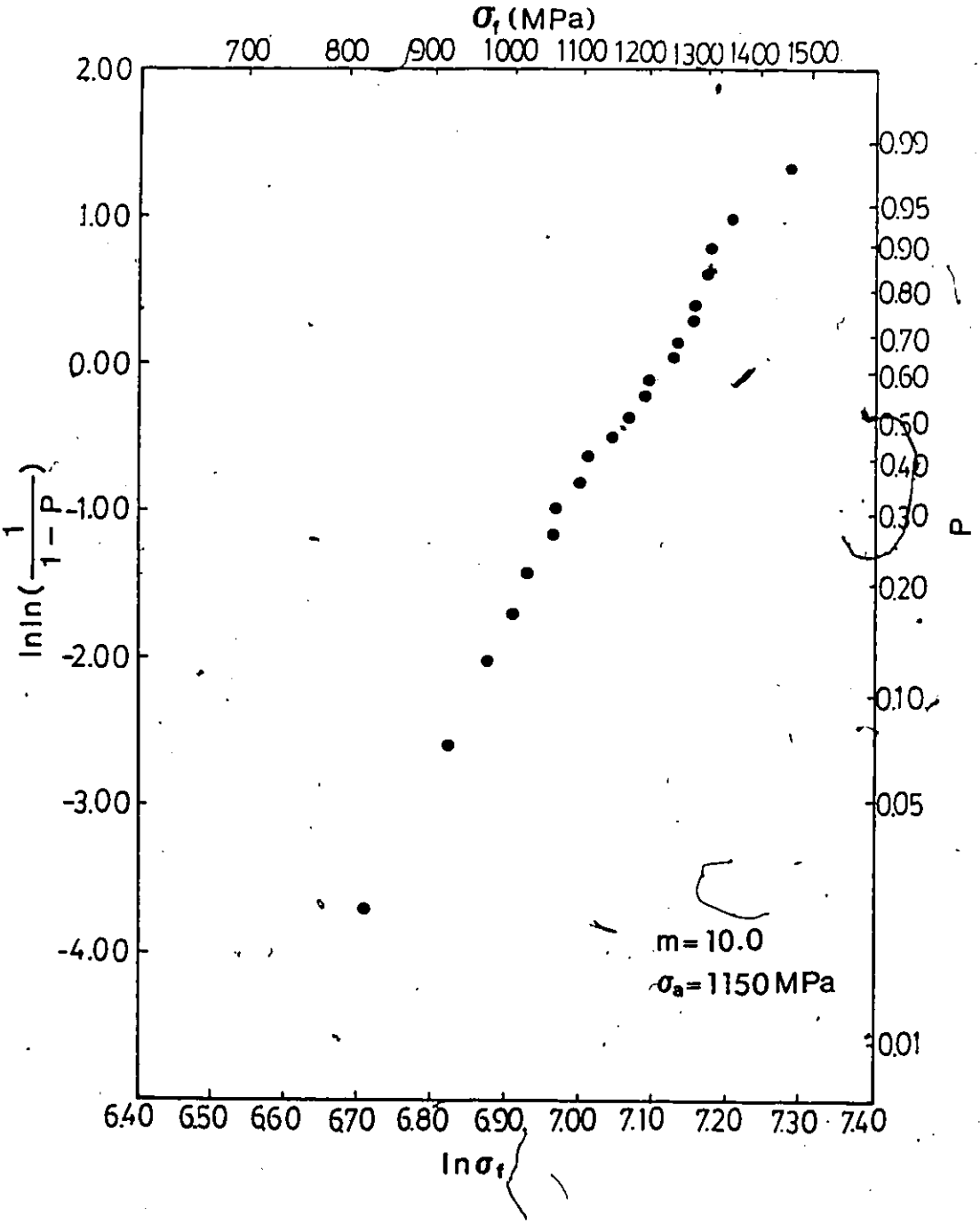

Fig. 3.17 Weibull plot for samples made from powder following methanol sedimentation.

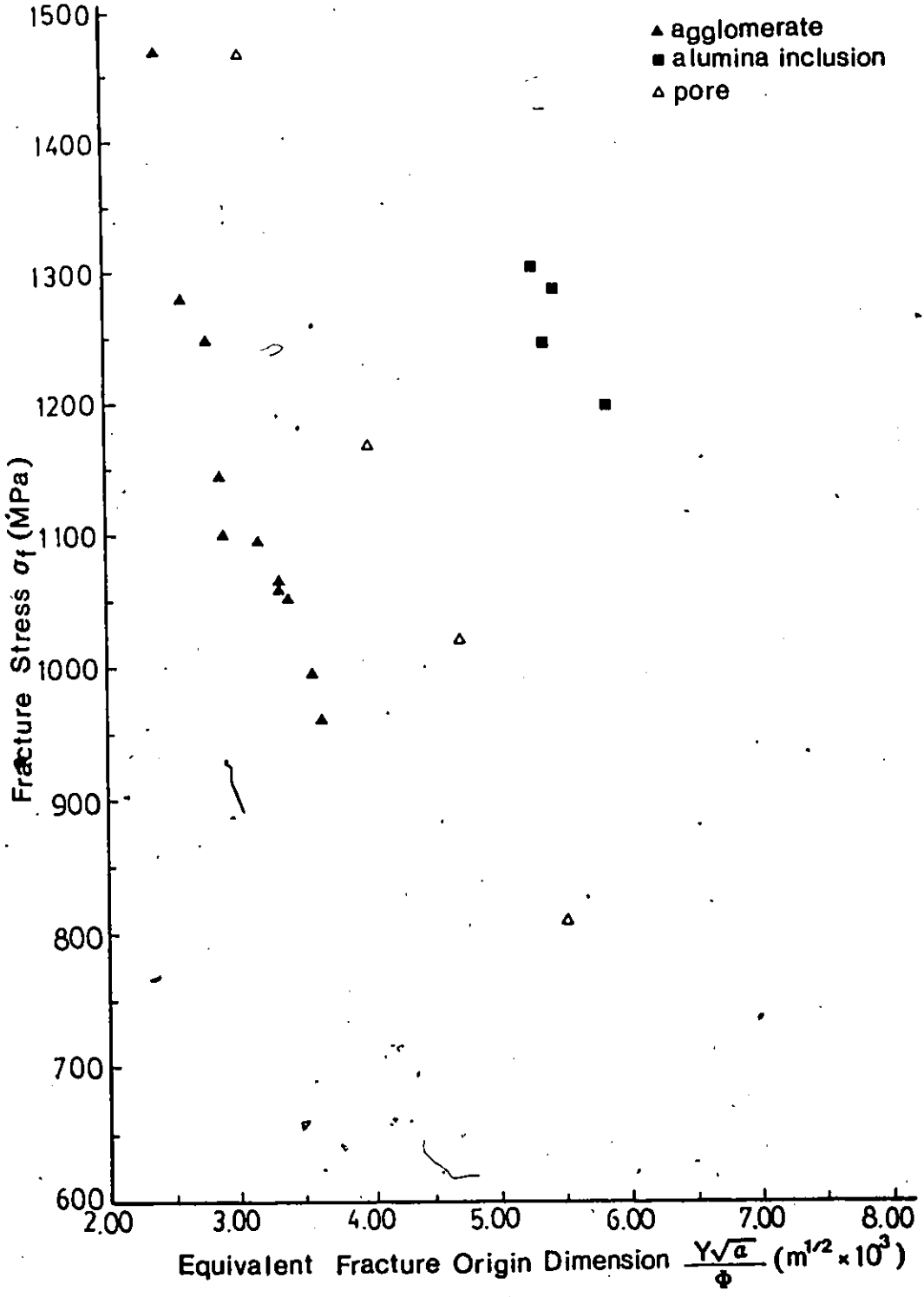

Fig 3.18 $\sigma_f - Y\sqrt{a}/\Phi$ plot for samples made from powder following methanol sedimentation.

fracture origins. The type-C iron inclusions have also disappeared, suggesting they were > 4 x 10^{-3} $m^{1/2}$ in the as-received powders or so small after sedimentation as to be non-competitive fracture origins. Type-B agglomerates > 3.5 x 10^{-3} $m^{1/2}$ equivalent dimension were eliminated as scheduled by the sedimentation giving agglomerate-origin fracture stresses > 950 MPa and as high as 1470 MPa. The type-D alumina inclusions were partially removed by the sedimentation and gave higher fracture stresses. The type-E pores were reduced in size by the sedimentation, burnout and re-isostatic pressing procedure. The processing resulted in a total improvement of 270 MPa average flexural strength over the as-received powder samples. Further strength improvement is now confined to the elimination of pore fracture origins.

(3) pH-2 Water Sedimentation, Burnout and Re-isostatic Pressing

The results of sediment volume test indicated that water (pH-2) was a good dispersion medium. Previous studies also used water (pH-1.2 to 3) as a dispersion medium with good results (Ch. 2.2.1). For a comparison with methanol, the as-received powders were settled in pH-2 water and pressed, isopressed, burnt-out, re-isopressed and sintered (as per that following methanol sedimentation). The agglomerate size scheduled for elimination was > 3.5 x 10^{-3} $m^{1/2}$ equivalent dimension. A considerable correction was

applied to Stokes' law (F ≃ 0.03). The resulting flexural strength data are shown in Fig. 3.19. The fracture stresses were between 950 and 1330 MPa with an average of 1145 MPa, i.e. approximately the same as that following methanol sedimentation. The Weibull modulus was improved to 16.5. The corresponding σ_f-$Y\sqrt{a}/\Phi$ plot is showed in Fig. 3.20 and is similar with Fig. 3.18. The position of the relative severity of fracture origin types was unchanged. Type-A and -C fracture origins were eliminated as expected. The size range of the agglomerates is narrower as compared with that following methanol sedimentation. This may account for the higher Weibull modulus. No pore fracture origins were observed at fracture stresses below ≃ 950 MPa. These findings suggest a relationship between the pore removal and the sedimentation with burnout/re-isostatic pressing. It is thought that the dispersion of the non-settled fraction could give an improved green packing density enhancing densification and porosity elimination on sintering. This process could be further aided by burnout and re-isostatic pressing. The type-D alumina inclusions were not reduced in size by pH-2 water sedimentation indicating their irregular behavior in sedimentation.

It is noted that although agglomerates could be effectively reduced in size and fiber inclusions and iron inclusions totally eliminated by proper processing, the average flexural strength could not be further improved

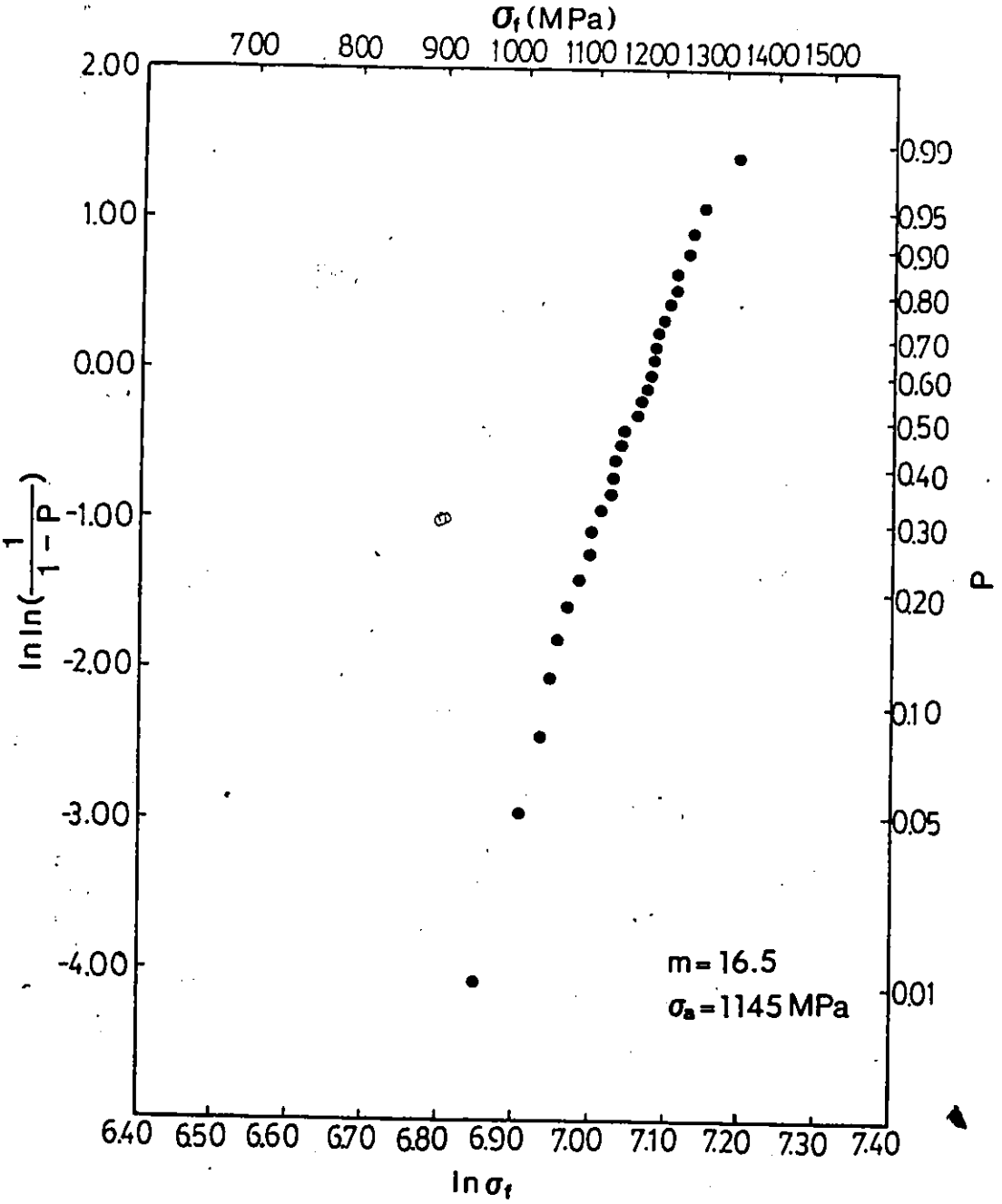

Fig 3.19 Weibull plot for samples made from powder following pH-2 water sedimentation.

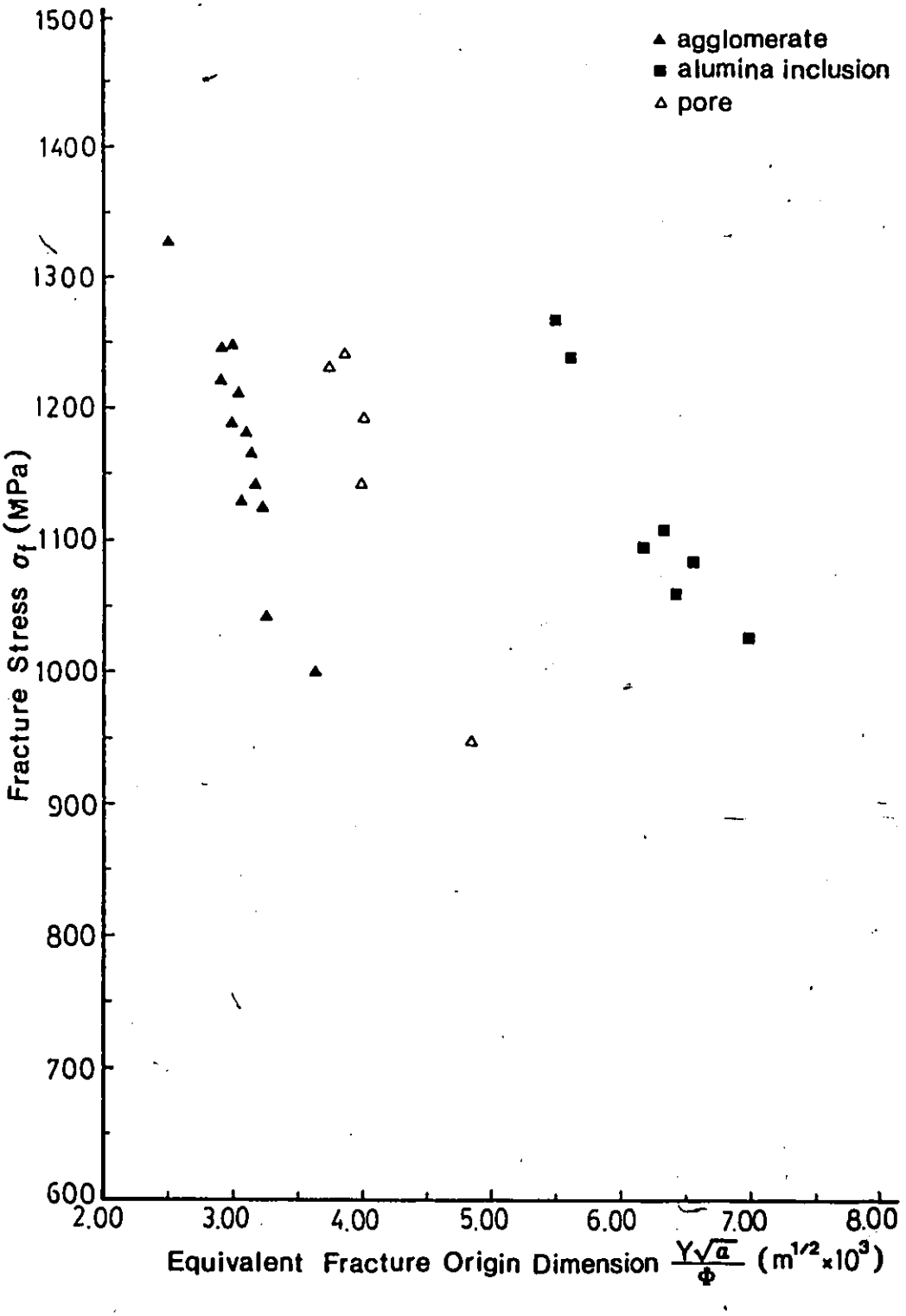

Fig. 3.20 $\sigma_f - Y\sqrt{a}/\Phi$ plot for samples made from powder following pH-2 water sedimentation.

because the alumina inclusions and pores were uninfluenced. It was also observed that further reduction of agglomerate size by sedimentation becomes gradually unjustifiable since the yield (the powder remaining in suspension) decreases. This suggests a high content of hard agglomerates in the as-received powders which are not dispersed by the liquid and its ultrasonification.

3.3.3 The Optimum Process

Based on the above results, an optimum processing route was identified. This involved elimination of agglomerates $> 2.5 \times 10^{-3}\ m^{1/2}$ equivalent dimension via methanol sedimentation followed by burnout and re-isostatic pressing. This procedure resulted in flexural strengths between 1090 to 1630 MPa with an average of 1380 MPa and a Weibull modulus of 12. This average strength is 500 MPa higher than that of the as-received-powder based ceramics. Fractographic examination showed that fiber and iron inclusions were eliminated and agglomerates were reduced in size.

3.3.4 The Predicted Optimum Fracture Stress

The above findings predict that high fracture stresses are attainable by fracture origin control. If (i) the starting Y-PSZ powder is free of alumina inclusions (the responsibility of the powder supplier) (ii) agglomerates and

pores are the only defects existing in the final sintered body (iii) the size distribution of agglomerates and pores is similar to those following methanol and pH-2 water sedimentation (iv) the final obtainable maximum agglomerate equivalent dimension after sedimentation is $\simeq 2 \times 10^{-3}$ $m^{1/2}$ (or $\simeq 5$ μm spherical diameter) then an average fracture stress of 1750 MPa with a maximum value of 2050 MPa is attainable. This is the upper limit of four-point-bend flexural strength or equivalent data (statistically converted from three-point-bend flexural strength) for Y-PSZ processed by the other methods (Ch. 2.2.2) (v) the lower limit of fracture stress due to pore defects will be 1100 MPa corresponding to the lower limit of flexural strength via hot isostatic pressing (Ch. 2.2.2). This strength level was also achieved in the present conventional sintering study. Pore-originated fracture is assumed as agglomerate-fracture will give the higher fracture stress levels. The predicted four-point-bend fracture stresses based on the above assumptions range between 1136 and 2047 MPa with a average of 1630 MPa. This figure should be realizable by carefully controlled processing.

3.3.5 Conclusions

The various processing routes and their results are summarized in Fig. 3.21. It was found that ;

(1) Sedimentation is an effective means of eliminating

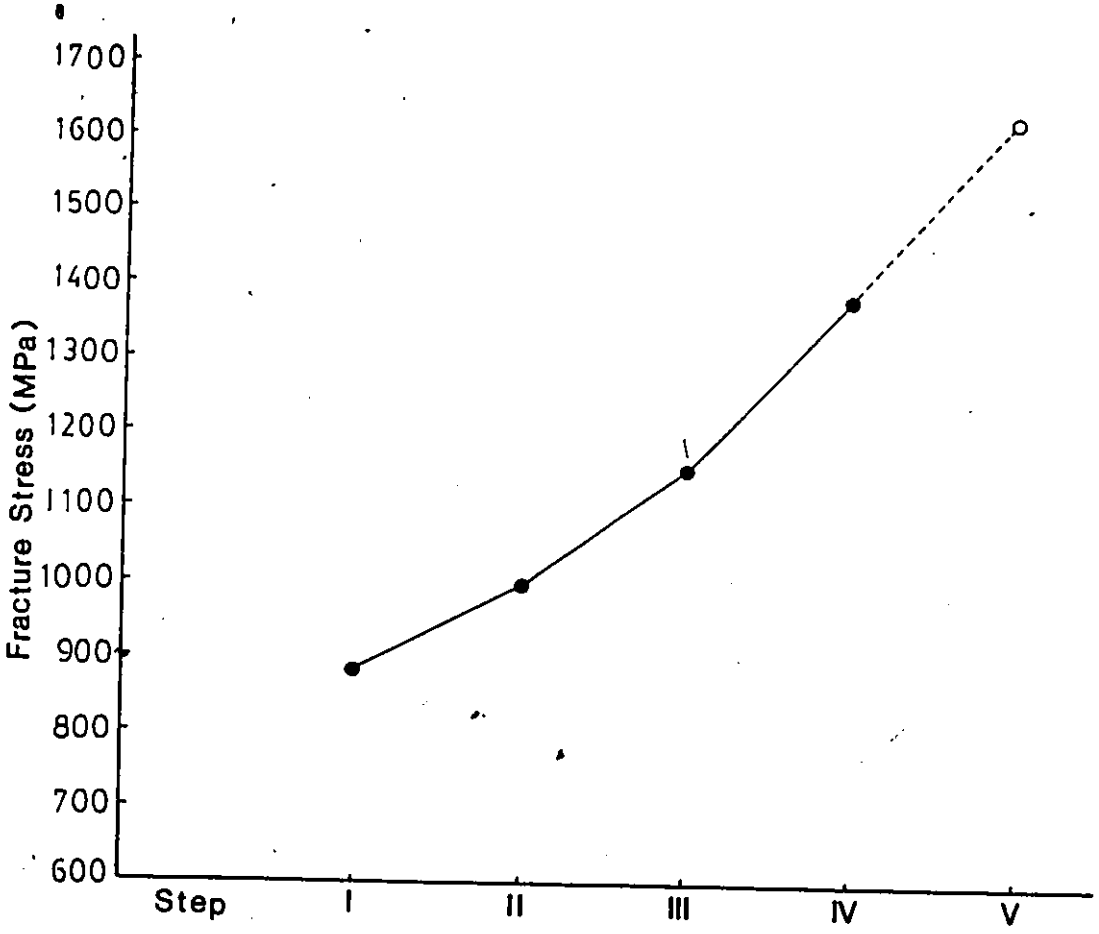

Processing route		As-received	2-Propanol sediment.	methanol (pH-2water) sediment. burnout	methanol sediment. burnout	prediction optimum
Fracture Origin Type	A	○	○	×	×	×
	B	○	4×10^{-3}	3.5×10^{-3}	2.5×10^{-3}	2×10^{-3}
	C	○	4.5×10^{-3}	×	×	×
	D	○	↘	↘	↘	×
	E	○	○	↘	↘	↘
Strength average		880	995	1150	1380	1630
Strength spread		650–1020	740–1280	950–1470	1090–1630	1100–2050

Fig. 3.21 Strength improvement via various processing routes for 4.5 wt% Y-PSZ.

agglomerates and other inclusion-type defects such as iron.

(2) Burnout/re-isostatic pressing is necessary if organic inclusions exist in the powders.

(3) The part-through elliptical crack extension model satisfactorily correlates the fracture stress and equivalent fracture origin dimension.

(4) Careful processing can result in conventionally-sintered ceramics with flexural strength values similar to those obtainable by hot-isostatic-pressing.

CHAPTER 4

The Relative Severity of Defect Types in Ceramics

4.1 Introduction

The trend of relative severity of defect types has been recognized in the previous studies (Ch. 2.1.1). The origin of this defect severity was not identified, nor quantitatively characterized. In Chapter 3, the part-through elliptical crack model was put forward to characterize the flaw/strength relationships for various processing routes and revealed some important aspects of the severity of defect types in a model ceramic. These will now be analyzed.

4.2 The Existence of the Severity of Defect Types

The results plotted in Fig. 3.13, 3.16, 3.18 and 3.20, are gathered together in Fig. 4.1. Clearly the behavior of each fracture-origin-type is predicted by Eq. (3.1). The curves reveal that the fracture origin types differ with respect to their responsibility for fracture, i.e. their relative "severity". The type-A fiber inclusions are the most severe (i.e. for a given size they reduce the potential strength the most), then type-B agglomerates, type-C iron inclusions and type-E pores, and finally type-D alumina inclusions. The relative severity of the agglomerate

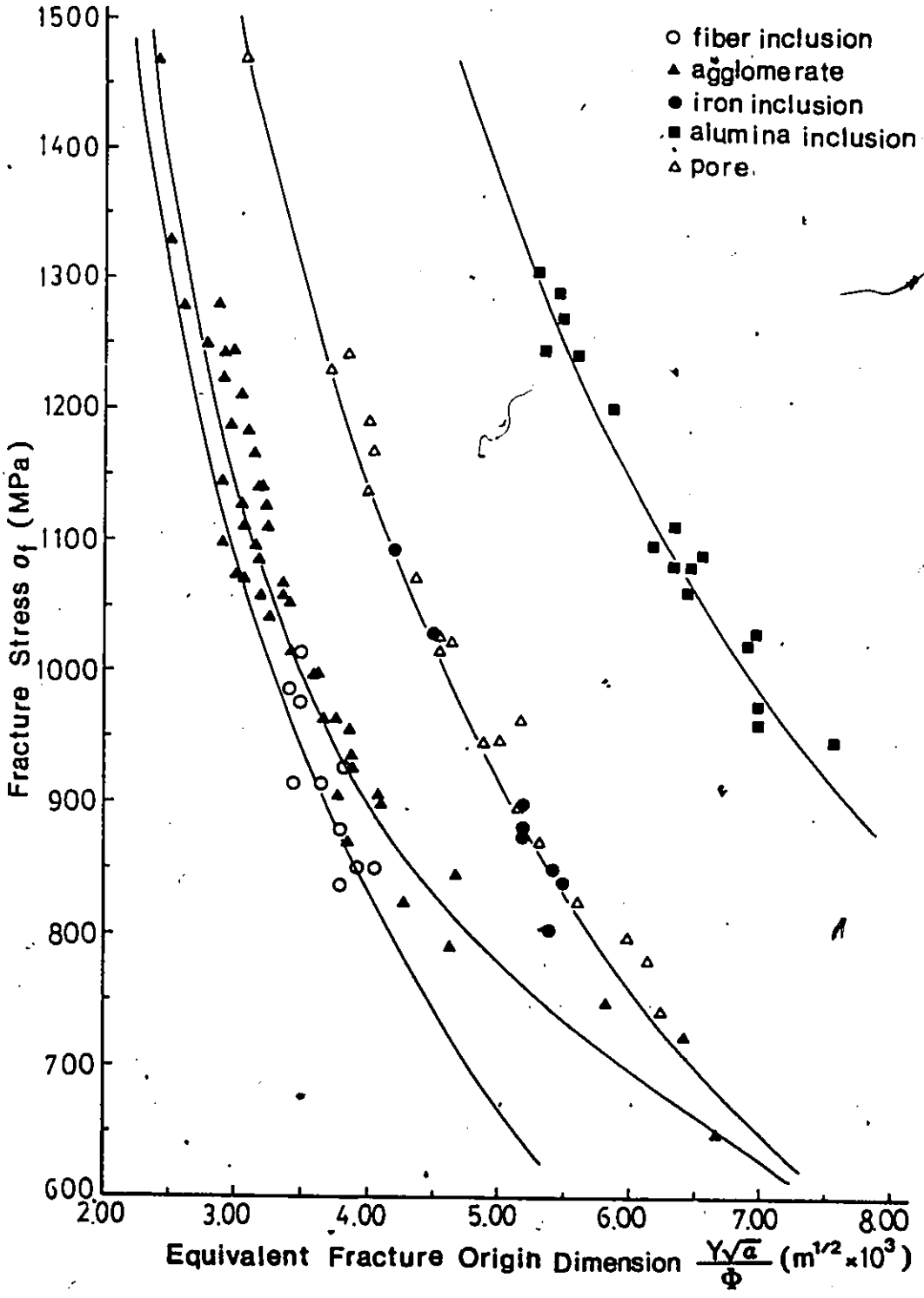

Fig. 4.1 Fracture stress - equivalent fracture origin dimension correlation for 4.5 wt% Y-PSZ samples.

fracture origins decreases below 900 MPa and finally merges with type-C and -E. Type-C and -E fracture origins have almost the same severity. The part-through crack model considers a crack equivalent to a pore with a traction-free periphery such as might develop normally on sintering (i.e. the model predicts type-E behavior). Therefore the fiber-inclusion and agglomerate fracture origins are more severe than predicted by the crack model, the iron-inclusion and pore fracture origins the same as predicted and the alumina-inclusion fracture origins less severe than predicted.

4.3 Origin of the Relative Severity of Defects

An explanation of the severity of fracture origin types will now be put forward based on associated residual stresses. The microstructure of agglomerate fracture origins (Fig. (3.9)) with their central larger-grained region and peripheral pores suggests the early start and completion of sintering. i.e. the higher-green-density agglomerates sinter faster to final density (Ch. 2.1.2, 2.3.1). This faster densification at the early stage of sintering will result in a tangential tensile residual stresses along the interface with the matrix (Ch. 2.3.1). This residual stresses are partially relieved by incoherency between the agglomerate and the matrix resulting in a pore-like cavity. However the densified matrix and the agglomerate itself may inhibit

complete stress relief leaving a residual stress[23]. This residual tensile stress when superimposed on the applied stress could cause fracture at lower stresses than predicted by the crack model (the latter considers the part-through-crack, residual-stress-free). The agglomerate fracture origin will thus be more severe than a pore of equivalent dimension. Similar reasoning can be applied to the fiber inclusions. By resisting the forming pressure during dry and isostatic pressing, a denser packing of the matrix ZrO_2 powder is expected to form local to the fibers. During sintering this denser layer will differentially sinter in a way similar to the agglomerate defect resulting in similar local residual stresses between it and the local matrix. This denser layer will not break away from the matrix and the residual tensile stresses are unrelieved by cavity formation. A more-severe condition than associated with the agglomerate defects thus develops (as observed). The observed microstructure peripheral to the cavity left by a fiber inclusion (Fig. 4.2) supports this explanation, i.e. the ZrO_2 grains around the cavity are denser and have larger size indicative of faster sintering. The iron inclusions will melt, oxidise and penetrate the surrounding ZrO_2

---

23. The existence of residual stresses around agglomerate defects in ceramics is experimentally verified in Ch. 5 and a residual-stress retention model is proposed in Ch. 9.

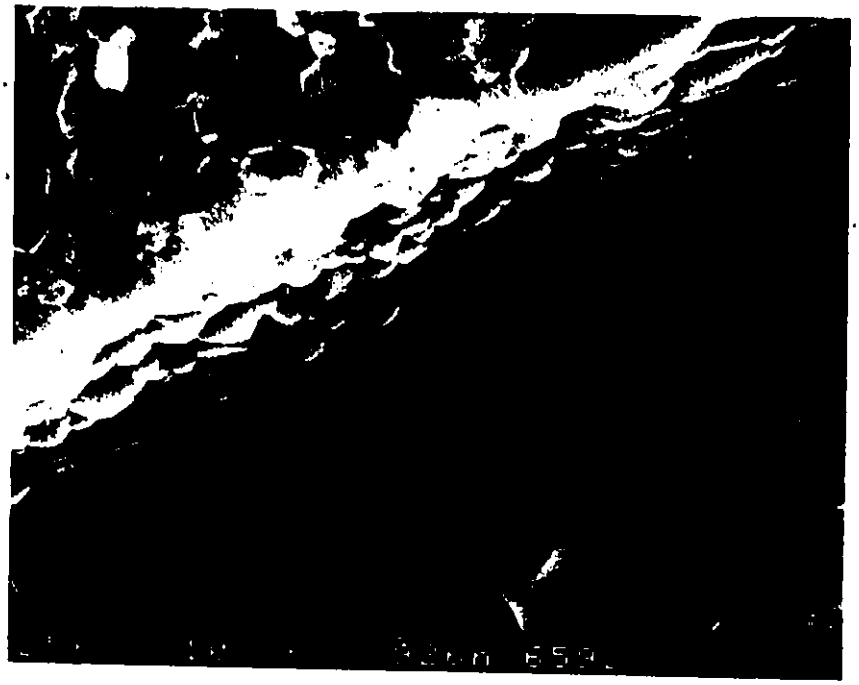

Fig. 4.2 A denser packed layer around a fiber inclusion

particles during sintering. No residual stresses should develop around such defects. The ZrO_2 grains inside these defects appear porous and unsintered and should have a fracture toughness lower than the surrounding matrix, i.e. the iron inclusions shall act like pores and have a severity similar to pores (as observed). Alumina inclusions, being coherent with the matrix, will develop radial compressive and tangential tensile residual stresses around their periphery due to their lower thermal expansion coefficient ($\simeq 8 \times 10^{-6}/^{\circ}C$) as compared with that associated with t-ZrO_2 ($\simeq 10 \times 10^{-6}/^{\circ}C$) (Ch. 2.3.1). The tangential tensile stresses would have the potential to develop radial microcracking (Ch. 2.3.1). However no microstructural evidence (Fig. 3.11) of microcracking was observed. This suppression may be related to the small tangential tensile stresses developed (Eq. 2.13)[24] and the subsequent elastic mismatch active on loading (Eq. 2.17 to 2.19) (Young's moduli: 400 GPa for Al_2O_3 and 220 GPa for t-ZrO_2)[25]. The superposition of the radial compressive stress and the applied tensile stress will result in higher fracture stresses than predicted by the crack model. Alumina

---

24. This is estimated as 0.2 to 0.3 times the fracture stress of the matrix (details see Ch. 8).

25. This is experimentally verified in Ch. 6 and an inclusion fracture model is proposed in Ch. 8.2.

inclusions are therefore less severe than pores. The evident size-effect of the agglomerate-fracture-origin severity is also explained by the magnitude of the residual stresses. When the agglomerates exceed an equivalent dimension of $\simeq 4 \times 10^{-3}\ m^{1/2}$ (corresponding to a fracture stress of $\simeq$ 900 MPa), the residual stresses can be further relieved by the defects becoming pores of $> \simeq 7 \times 10^{-3}\ m^{1/2}$ equivalent dimension.

The above explanation provides a unified argument for the relative severity of defect types and is considered to hold reasonably well for pores, iron inclusions and alumina inclusions. Previous studies on the experimental determination of the residual-stress distribution in ceramics have not reported the existence of residual stress around pores developed normally on sintering (Ch. 2.3.1). This indicates that pores are residual-stress-free defects. The retention of post-sintering residual stresses around fiber inclusions and agglomerates requires that these are not completely relieved upon formation of the associated cavities and during sintering. To further assert these arguments, it is first necessary to establish the existence of residual stresses around the fiber inclusions and agglomerates. This is the subject of the next chapter.

4.4. Quantitative Expressions for the Relative Severity of Defects

Since each fracture origin type is well characterized by the crack model, a quantitative expression for their relative severity is obtained by rearranging Eq. (3.1), i.e. ;

$$\sigma_f = \left(\frac{K_{Ic}}{\sqrt{1 - \nu^2}} \right) \frac{1}{Y\sqrt{a}/\Phi} \qquad (4.1)$$

and plotting σ_f v.s. $1/(Y\sqrt{a}/\Phi)$ for the various fracture origin types. The straight line plots obtained by the least squares method have slopes of $K_{Ic}/\sqrt{1 - \nu^2}$ and, using $\nu = 0.25$ for the tetragonal ZrO_2, the apparent K_{Ic} values (denoted as K_{Ic}^*) are calculated and results are shown in Fig. 4.3. These K_{Ic}^* values are : 3.2 ± 0.1 $MN \cdot m^{-3/2}$ for the fiber-inclusion fracture-origin contained t-ZrO_2, 3.4 ± 0.1 $MN \cdot m^{-3/2}$ for the agglomerate fracture-origin contained t-ZrO_2, 4.4 ± 0.1 $MN \cdot m^{-3/2}$ for the iron-inclusion and the pore fracture-origin contained t-ZrO_2 and 6.7 ± 0.1 $MN \cdot m^{-3/2}$ for the alumina-inclusion fracture-origin contained t-ZrO_2. These values reflect the severity of the fracture origin types vis-á-vis the fracture of Y-PSZ materials containing them.

Further characterization of the relative severity was obtained by measuring the actual K_{Ic} value of the tetragonal ZrO_2 matrix and comparing with the apparent K_{Ic} values for the t-ZrO_2 with various fracture-origin types. The microindentation technique (Ch. 2.5.3) using a Vickers

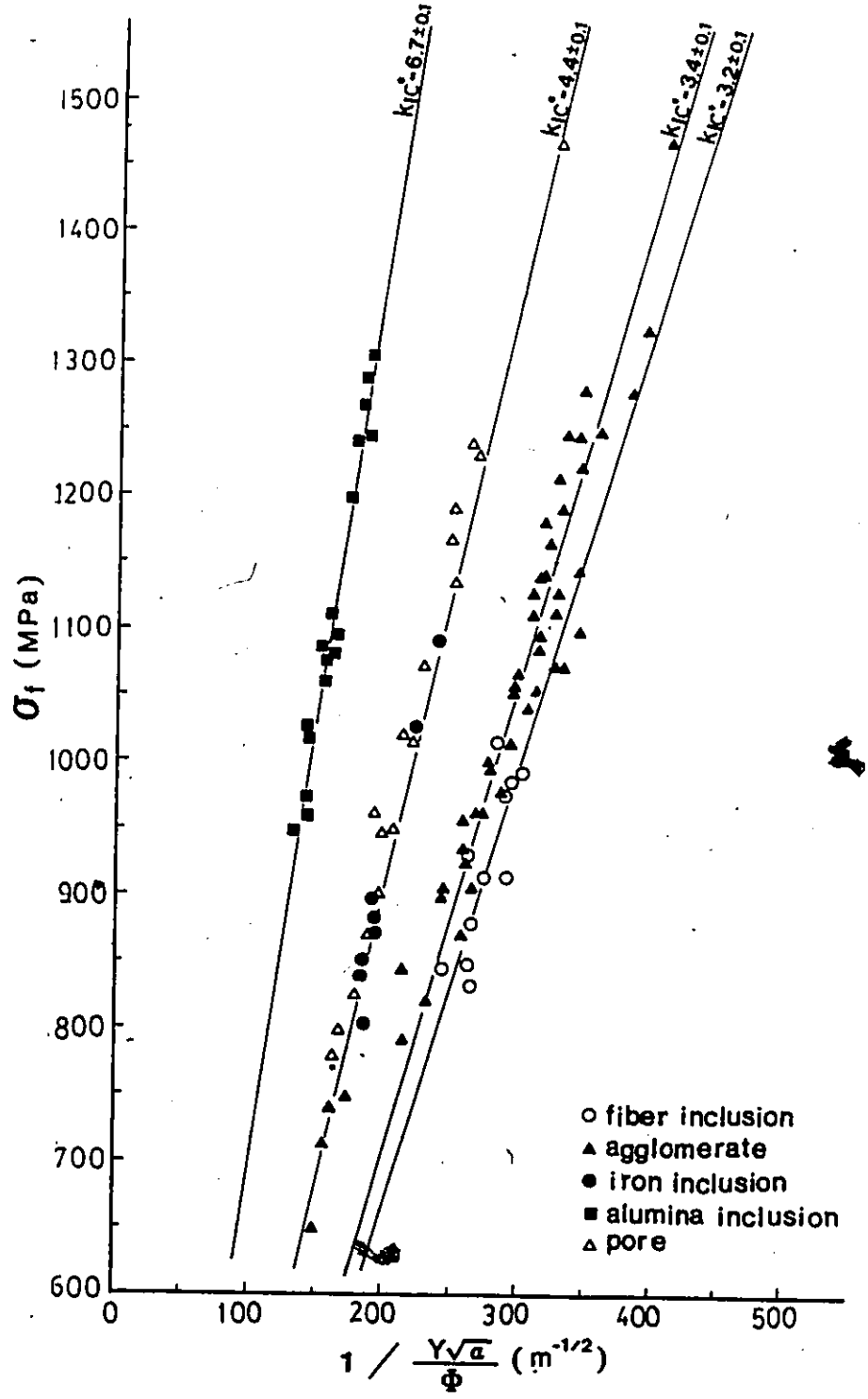

Fig. 4.3 Fracture stress - inverse equivalent fracture origin dimension plot for 4.5 wt% Y-PSZ.

indenter[26] with 294 N load gave a K_{Ic} value of 6.9 ± 0.3 $MN \cdot m^{-3/2}$. Comparing this value with the theoretical one calculated from the part-through crack extension model, i.e. for pores, a ratio of 1.55 is obtained. This result is close to that reported by Seshadri [1981] for defects in SiC using the same crack model. He obtained K_{Ic}^{*} = 2 to 2.8 $MN \cdot m^{-3/2}$ as compared with indentation-K_{Ic} values of ≃ 3.5 $MN \cdot m^{-3/2}$. The origin of the discrepancy is still unknown. Previous studies [Rice, 1980a, 1980b; Usami, 1986] reported that the critical stress intensity factor to extend a small flaw might be considerably smaller than that determined by fracture mechanical methods. The predicted apparent K_{Ic} for pore defects in the present study may represent the real K_{Ic} associated with a residual-stress-free flaw in tetragonal zirconia. A "relative defect severity parameter" (termed "X") can be defined and Eq. (3.1) rearranged to give ;

$$K_{Ic} = \sigma_f \cdot X \cdot \frac{Y \sqrt{a}}{\Phi} \qquad (4.2a)$$

$$\frac{K_{Ic}}{\sqrt{1 - \nu^2}} = \sigma_f \cdot X \cdot \frac{Y \sqrt{a}}{\Phi} \qquad (4.2b)$$

X values based on indentation-K_{Ic} (and crack-model prediction) for fracture origin types are : 1.03 (0.66) for

---

26. Zwick, Conn. U.S.A.

alumina inclusions, 1.57 (1.00) for pores and iron inclusions, 2.03 (1.29) for agglomerates and 2.16 (1.38) for fiber inclusions. It is noted that X values for various fracture origin types depend on the material and processing methods as well as the methods used to measure fracture toughness. The "relative" nature of X is emphasized.

Eq. (4.2) represents a necessary correction to the original crack model incorporating the defect-severity parameter. This influences strength predictions. The form of Eq. (4.2) as well as the specific values of relative-defect-severity-parameter are useful for predicting the fracture stress of a ceramic component wherein the types, dimensions and positions of the most critical defects are known (by NDE methods, for example).

4.5 Conclusions

The present analysis reached the following conclusions ;

(1) The relative severity of defect types in a model ceramic has been identified via a part-through crack extension model applied to the data for the various processing routes.

(2) A unified explanation of the observed relative defect severity has been suggested using the local residual stresses associated with the defects.

(3) The relative severity of the defect types can be

quantitatively expressed by the "apparent fracture toughness" of the defective ZrO_2 or a "relative defect severity parameter" (X) defined to correct the original model.

CHAPTER 5

Residual-Stress Defect-Severity Relationships in Ceramics

5.1 Introduction

In Chapter 4, the relative severity of defect types in a model ceramic was identified and their order quantitatively ranked. It was proposed that the relative defect severity is related to local residual stresses developed during processing. Previous studies (Ch. 2.3.1) showed that residual stress might develop around an agglomerate defect due to local differential sintering and around an inclusion defect due to thermal contraction mismatch. The magnitude of the residual stresses around an inclusion defect below the stress-relaxation-temperature, T_g, has been determined. Evidence of residual stresses around an agglomerate-defect has still to be gathered. This chapter reports and discusses evidence supporting the existence of residual stresses associated with the specific defect types. The Variation of the relative-defect-severity-parameter (X) with temperature (200 to 1000°C) is determined for the various defect types in tetragonal ZrO_2 ceramics and the value of T_g is obtained experimentally. Implications for strength improvement are also discussed.

5.2 Analytical Procedure

A modified crack model for the flaw/strength relationship incorporating the relative severity parameter was given in Eq. (4.2). Since the principle of superposition allows transference of local stresses to remote boundaries (Ch. 2.3.1), the residual stresses around defects can be superimposed on the applied tension in the same direction, i.e. Eq. (4.2b) can be rewritten as ;

$$\frac{K_{Ic}}{\sqrt{1-\nu^2}} = X \cdot (\sigma_{0f} - \sigma_{\bullet}) \cdot \frac{Y\sqrt{a}}{\Phi} \qquad (5.1)$$

where $\sigma_{\bullet}$ is an "equivalent" applied tension transferred from local residual stress, positive for tension and negative for compression, and σ_{0f} is the fracture stress in the absence of residual stress (an analytical expression for $\sigma_{\bullet}$ is derived in Chapter 8). Since $\sigma_f = \sigma_{0f}$ and $X = 1$ (Ch. 4.4) for a residual-stress-free pore fracture origin so, for the other types of fracture origin with the same equivalent defect dimension ($Y\sqrt{a}/\Phi$) as a pore, one obtains ;

$$X \cdot (\sigma_{0f} - \sigma_{\bullet}) = 1 \cdot \sigma_{0f} \qquad (5.2)$$

i.e. $$X \cdot \sigma_f = 1 \cdot (\sigma_f + \sigma_{\bullet})$$

or $$X = 1 + \frac{\sigma_{\bullet}}{\sigma_f} \qquad (5.3)$$

X is thus related to σ_r and any variation of residual stress should be reflected in a variation of X. X values at particular temperatures can be determined from Eq. (4.2b) via corresponding fracture-stresses, fracture-toughnesses and fracture-origin-dimensions. This is evident for the temperature-dependent residual stress associated with an inclusion due to thermal contraction mismatch (Ch. 2.3.1, Eq.(2.12)). Agglomerate- and pore- defects can also be examined to identify any residual stress relaxation with temperature. It is possible to obtain the T_g value for the matrix as the temperature whereat the corresponding X value is equal to unity [from Eq. (2.12)]. An experimental method of determining the residual stresses associated with the fracture-initiating defects and the magnitude of T_g for the matrix will now be described.

5.3 Experimental Procedure

5.3.1 High-Temperature Strength of As-Sintered Y-PSZ

4.5 wt% Y-PSZ samples were prepared, sedimented, burntout and reisopressed (Ch. 3.3.3). The high-temperature flexural strength was measured between 200 and 1000°C at 200°C intervals using the four-point-bend testing device described in Chapter 3 (Fig. 3.6), with a furnace capable of attaining 1400°C and a steel post water-cooled during heating to protect the load cell. The machine crosshead speeds utilized were 0.2 to 0.8 mm/min; the higher speeds

were used at high temperatures to assure linear elastic fracture (Ch. 2.5.1).

5.3.2 High-Temperature Fracture Toughness Measurement

The chevron-notch bend-bar test was used to determine the fracture toughness (Ch. 2.5.2). The sample dimensions were 3 x 4 x 25 mm with an inner span of 10 mm and an outer span of 20 mm. The chevron-notch geometry was α_0= 0.5 and α_1= 1 with a slot width of 150 μm. The same device was used to obtain load and displacement data as for the high-temperature four-point-bend test. Crosshead speeds were two-step controlled (0.003 to 0.3 mm/min) to assure crack initiation and valid stable crack growth (Ch. 2.5.2). Detailed procedures are described in Chapter 7. Data were gathered at the same temperatures used for the strength tests.

5.3.3 Stress Relaxation Treatments

The as-sintered samples were heat-treated in air at 1250°C for 3 hours. This temperature and time was chosen following the results of Procedures 5.3.1 and 5.3.2 (details in Results and Discussion). The samples were four-point-bend strength tested as per Procedure 5.3.1.

5.3.4 Defect Characterization

Fracture origins were examined by scanning electron

microscopy. The dimensions and types of defect were identified and the "equivalent defect dimension" computed following the procedure described in Ch. 3.2. $\hat{X}$ values were calculated for the various defect types as a function of temperature.

5.4 Results and Discussion

The high-temperature strength data for Y-PSZ are shown in Fig. 5.1. The strength continuously decreases as temperature increases. This behavior is typical of Y-PSZ ceramics (Ch. 2.4). The strength degradation accompanies the diminishing potency of the phase-transformation toughening with increasing temperature. The marked improvement of Y-PSZ room-temperature strength by flaw elimination (Ch. 3.3.3) did not carry through to high temperatures whereat the strength is low.

Y-PSZ high-temperature fracture toughness data are shown in Fig. 5.2. Transformation toughening decreases linearly with increasing temperature up to $\simeq 800^{\circ}C$, consistent with Lange's prediction [1982b]. These results suggest the $m \rightarrow t$ phase transformation occurs between 800 and $1000^{\circ}C$. The strength and fracture toughness curves reveal that no substantial change of flaw population (types, proportions and dimensions) occurs in Y-PSZ between 200 and $1000^{\circ}C$ as compared with room temperature. The results in Fig. 5.2 also suggest that no other fracture-toughness

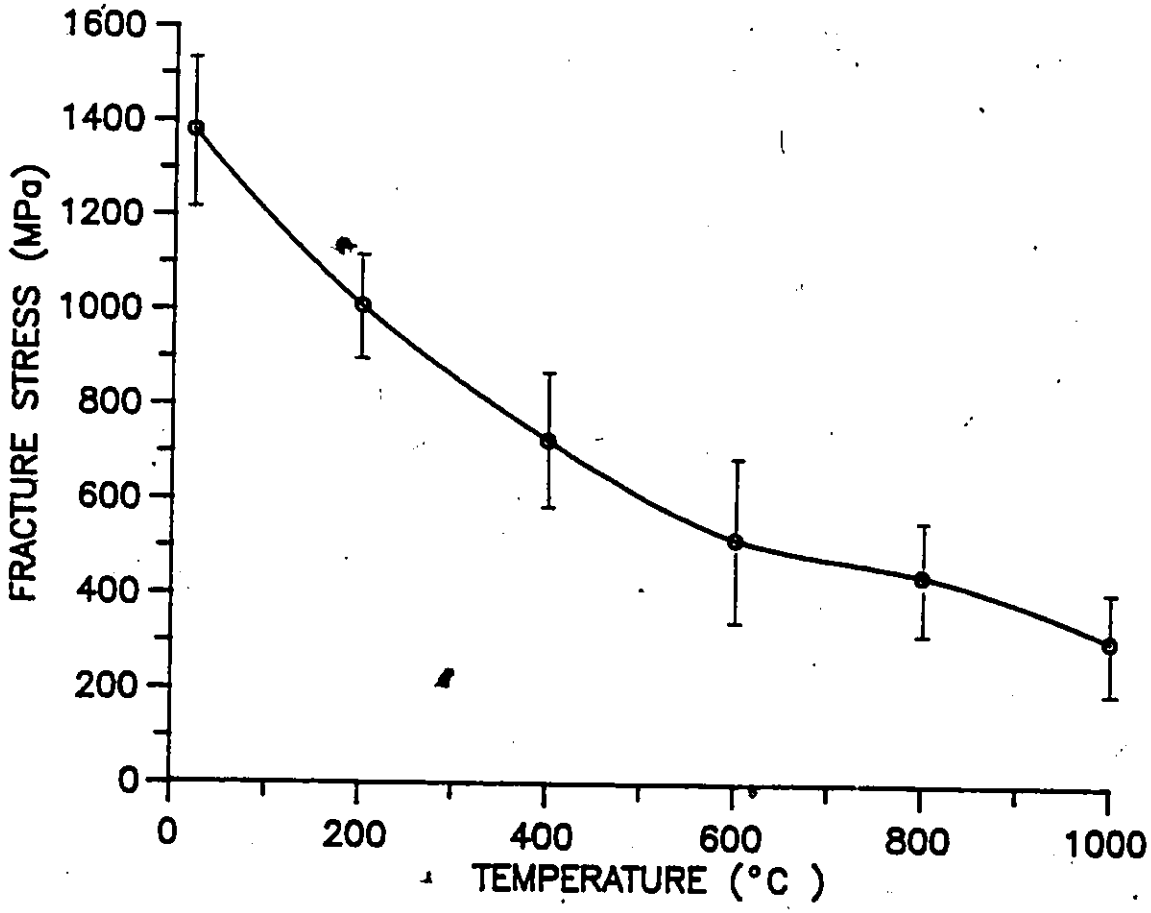

Fig. 5.1 High-temperature bend strength data for Y-PSZ.

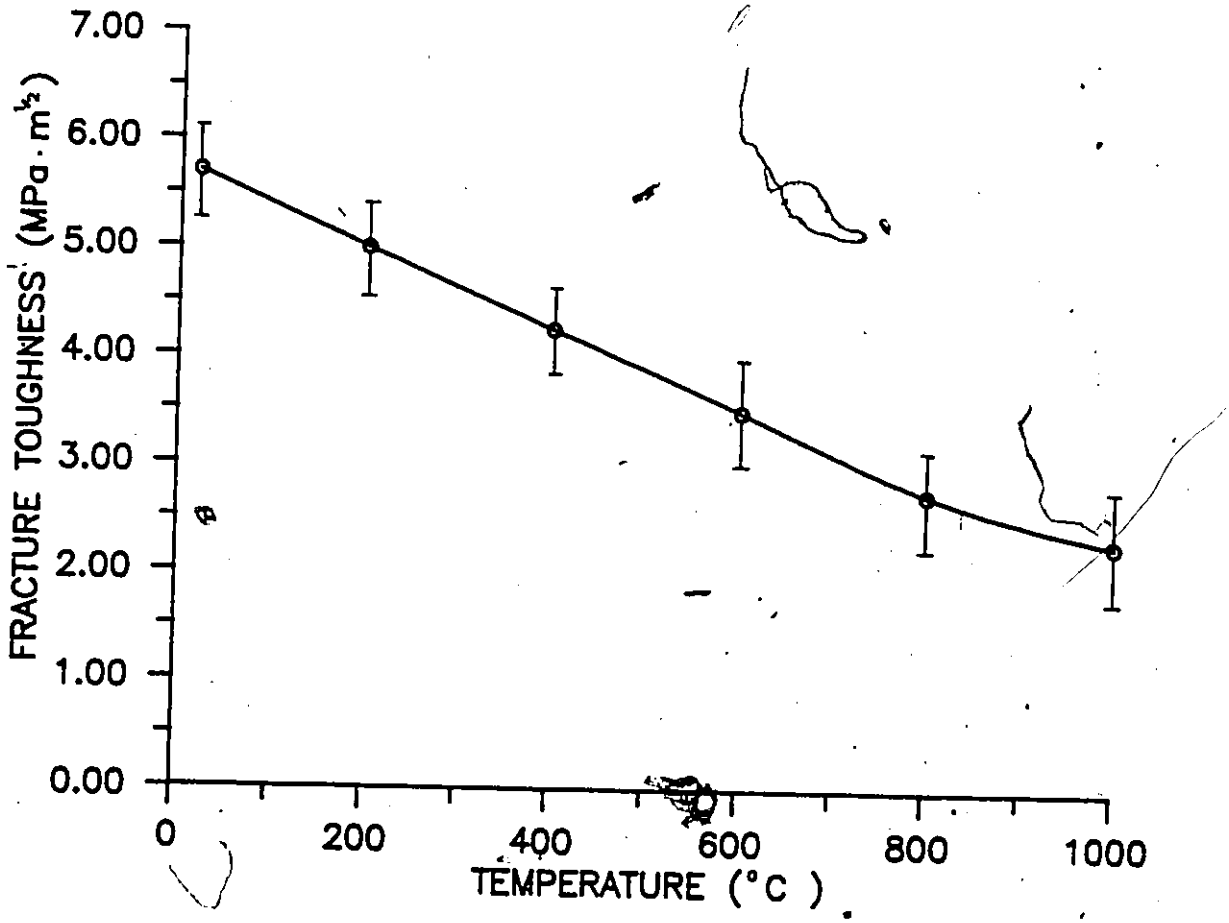

Fig. 5.2 High-temperature fracture toughness data for Y-PSZ.

degrading mechanisms or global creep processes [Evans, 1983] are active in this temperature range. This observation is further supported by the linearity of the bend-test load-displacement curves.

The variation of X with temperature for the α-Al_2O_3 defects in t-ZrO_2 is shown in Fig. 5.3. X increases linearly with increasing temperature, consistent with the predictions of Eqs. (2.12) and (5.3). The α-Al_2O_3 defects have a more severe effect as temperature increases. Residual stresses will completely relax at $T \geq T_g$ (from Eq. (2.12)) and then the residual-stress-free α-Al_2O_3 inclusions, of lower fracture toughness than the matrix, will act like iron inclusions or pores and the X value should equal unity (Ch. 4.4). The existence of this residual-stress-free condition is the basis of an experimental method for determining T_g, i.e. the temperature at which the X-curve for α-Al_2O_3 defects extrapolates to unity will be T_g. This extrapolation is shown in Fig. 5.3 and $T_g \simeq 1135^{\circ}C$.

The variation of X with temperature for pore- and agglomerate-defects is shown in Figs. 5.4 and 5.5 respectively. No change of X was detected in this temperature range suggesting the severity of these defect types is constant with rising temperature. So either the residual stresses associated with these defect types are not relaxed or residual stresses did not exist in the first place. Residual stresses are unlikely to be associated with

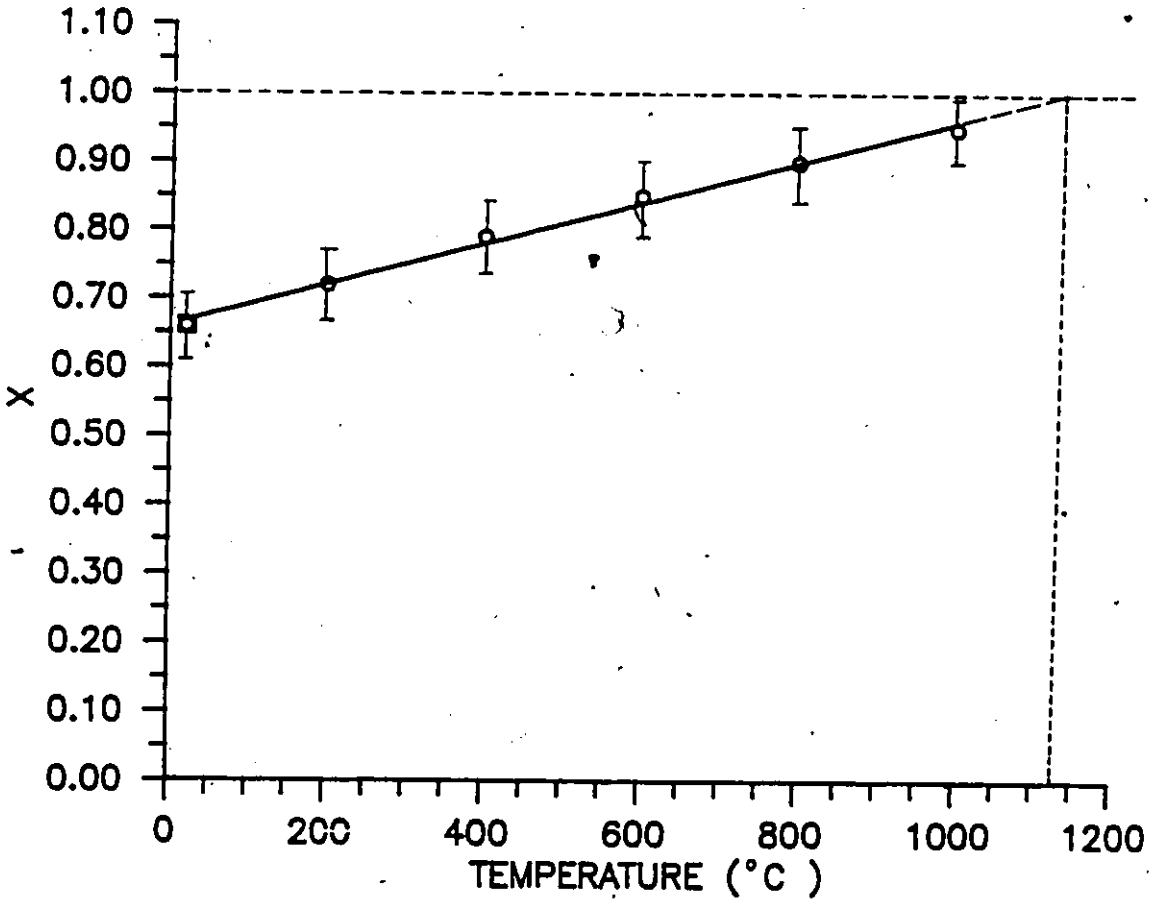

Fig. 5.3 Defect severity parameter (X) - temperature plot for α-Al_2O_3 defects in Y-PSZ.

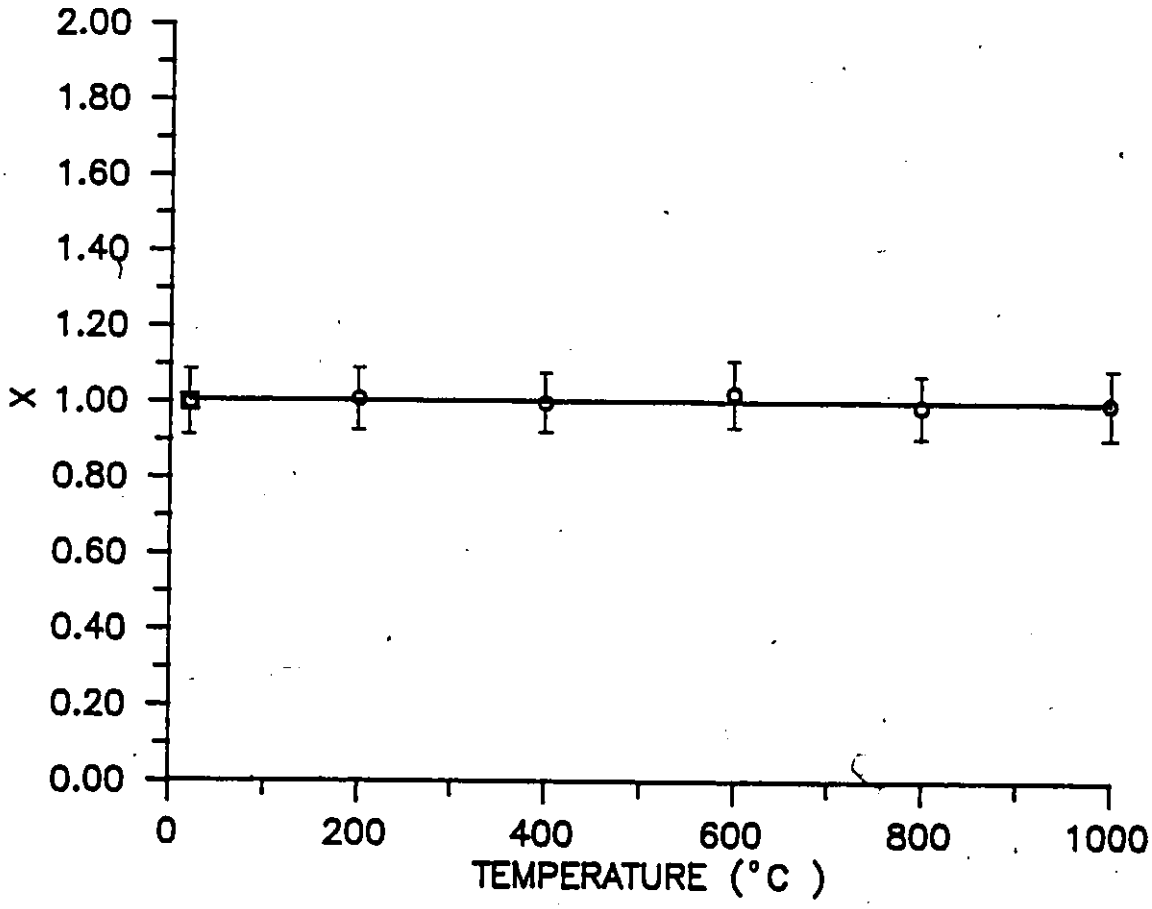

Fig. 5.4 Defect severity parameter (X) - temperature plot for pore defects in Y-PSZ.

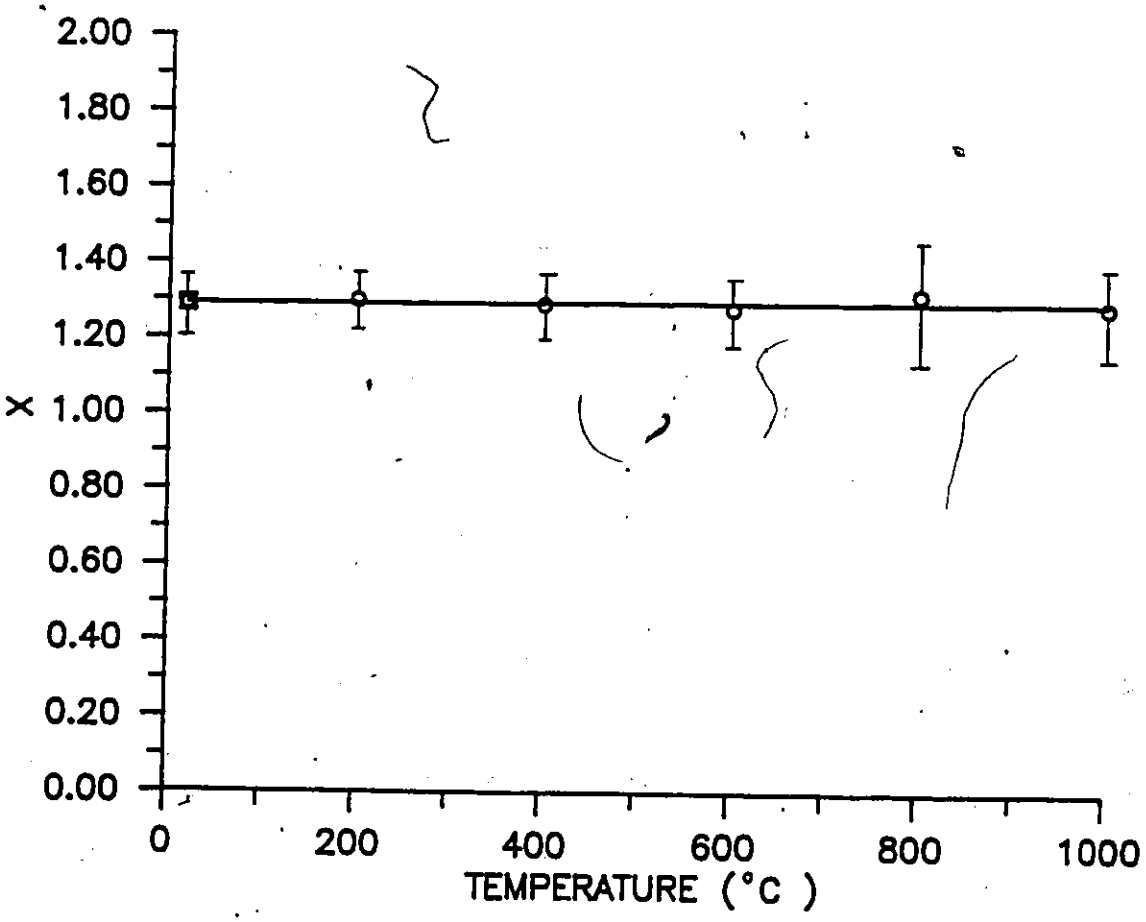

Fig. 5.5 Defect severity parameter (X) - temperature plot for agglomerate defects in Y-PSZ.

pores following sintering. There is some question as to whether residual stresses associated with agglomerate defects survive sintering (Ch. 3.3.1).

The physical significance of T_g is further examined to clarify these issues. Evans and Clarke [1980b] defined T_g as the temperature below which existing residual stresses are no longer relaxed by diffusion or viscous flow (the latter can occur in the presence of a grain-boundary amorphous phase). From the relaxation behavior of residual stress associated with thermal contraction mismatch (Eq. (2.12) and Fig. 5.3), the requirement for fast stress redistribution during cooling favors relaxation by viscous flow. For residual-stress induction processes other than thermal contraction mismatch, substantial relaxation by viscous flow could be time-dependent. Therefore holding sintered samples for sufficient times at $T > T_g$ could relieve residual stresses possibly associated with agglomerate defects following sintering. Such a change of residual stress state should be reflected in changes of the corresponding X values. Sintered samples were therefore reheated to 1250°C for 3 hours (Experimental Procedure 5.3.3), i.e. about T_g + 100°C, a temperature and time judged to be sufficient for stress relaxation but insufficient to reactivate the sintering process and alter the material properties (e.g. fracture toughness). The X-value results for pore- and agglomerate-fracture-origin samples following

this heat treatment are shown in Fig. 5.6 and Fig. 5.7 respectively. The X values for pore defects (Fig. 5.6) are unchanged. The X values for the agglomerate defects are lowered from X = 1.30 for the unannealed samples to X = 1.0 for the annealed ones (Fig. 5.7). This indicates that residual stresses did exist associated with agglomerate defects following sintering and these relax during heat treatment giving a severity equivalent to equal-sized pores. The unchanged X values for pores following heat treatment supports their residual-stress-free condition after sintering.

The survival of residual stresses associated with agglomerate defects following sintering (at a sintering temperature > T_g) requires the occurrence of several events. These involve the residual-stress, (1) build-up process during the initial stages of sintering, (2) elastic relaxation process on formation of the circumferential cavity, (3) viscous relaxation during sintering. Complete investigation on these complicated issues is beyond the scope of the present study. In Chapter 9 a preliminary model is developed to rationalize the observed phenomena and correlate with the experimental data.

The present results have implications on the strength improvement of ceramics by flaw elimination. The substantial improvement of ceramic strength achieved by

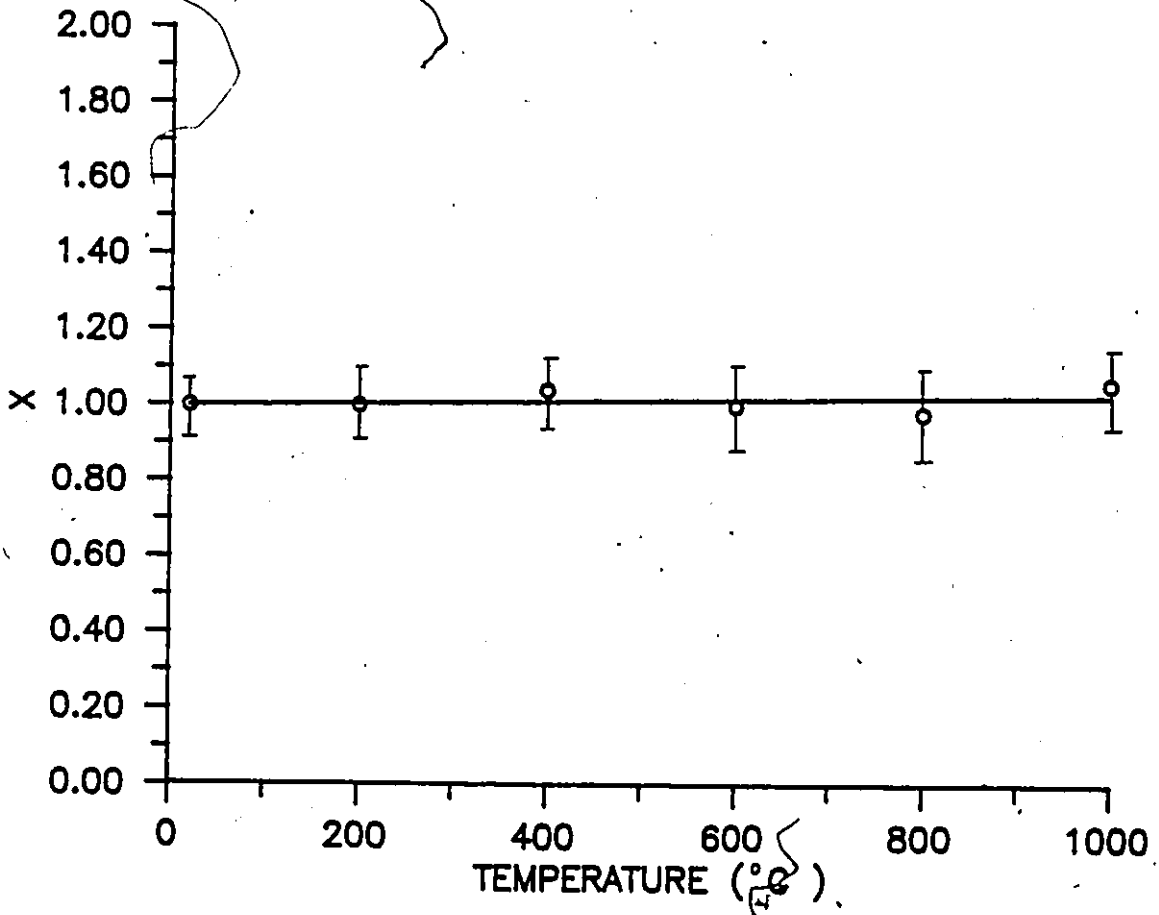

Fig. 5.6 Variation of X values with temperatures for pore defects in heat-treated Y-PSZ.

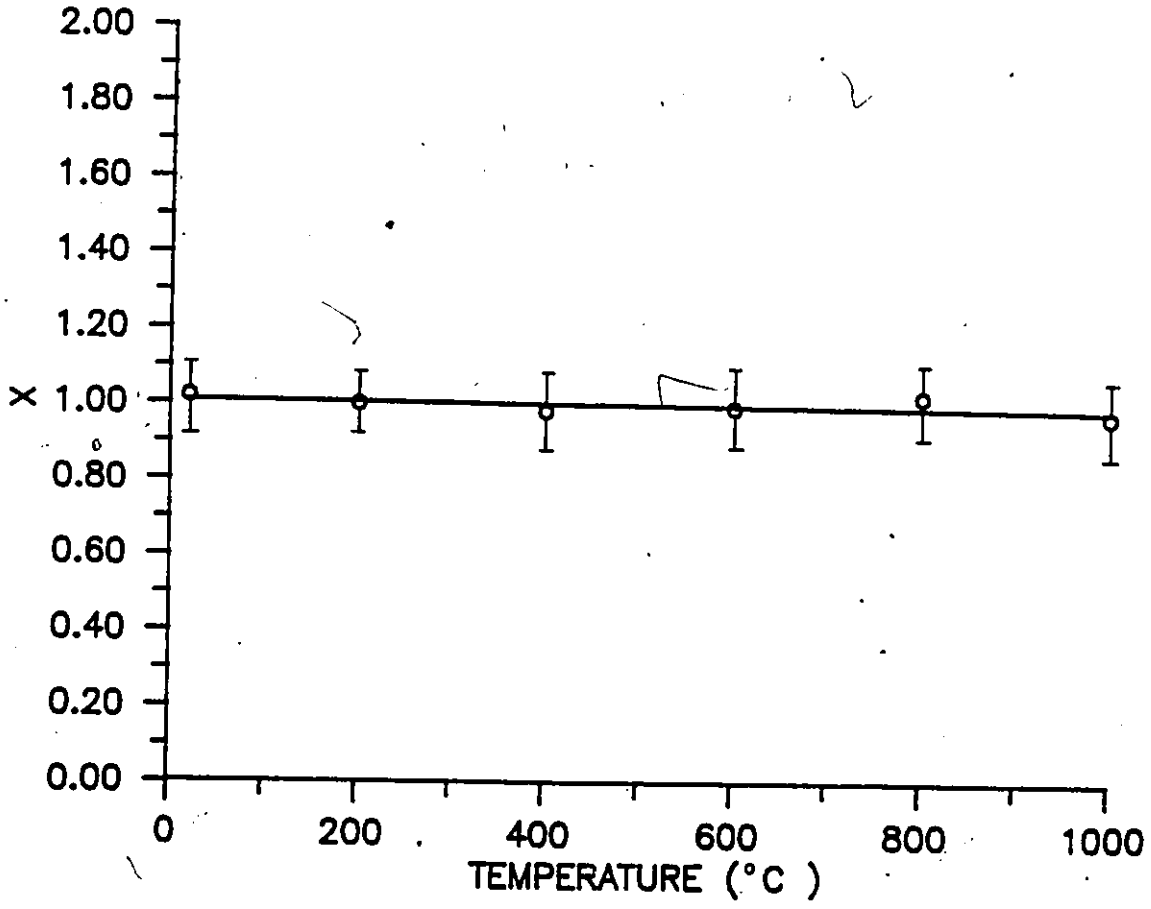

Fig. 5.7 Variation of X values with temperatures for agglomerate defects in heat-treated Y-PSZ..

eliminating large agglomerates via sedimentation processing (Ch. 3.3.2) is further reinforced by reduction of the severity of the remaining agglomerate defects by appropriate heat treatment during or after the sintering process. Knowledge of T_g is necessary to select optimum conditions. The severity of pore defects is unaffected by heat treatment and reduction of their number and size (e.g. via hot isostatic pressing or slip casting) is the only way to reduce their effect. α-Al_2O_3 defects in a t-ZrO_2 matrix have a low severity ($X < 1$) at room temperature but X approaches unity as temperature rises. These will become the predominant flaws at elevated temperatures. Since α-Al_2O_3 defects are insensitive to removal by sedimentation (Ch. 3.3.2), Al_2O_3-free Y-PSZ powder can only be achieved by the powder synthesizer.

5.5 Conclusions

The residual stresses associated with defects in t-ZrO_2 have been investigated by combined high-temperature strength, fracture-toughness tests and fractography. The following conclusions have been reached :

(1) The relative severity of the defect types in t-ZrO_2 ceramics arises from local residual stresses developed during sintering and cooling.

(2) A residual-stress relaxation temperature, $T_g \simeq$ 1135°C, was determined for t-ZrO_2.

(3) Below T_g, a temperature-dependent residual stress is associated with α-Al_2O_3 defects in t-ZrO_2. A temperature-independent residual stress is associated with agglomerate defects. Pore defects are residual-stress free.

(4) Residual stress around agglomerate defects following sintering can be relaxed by post-sintering heat treatment at $T = T_g + 100^{\circ}C$ for 3 hours.

CHAPTER 6

Analysis of the Fracture Characteristics of α-Al_2O_3 Inclusions in a Tetragonal Zirconia Matrix

6.1 Introduction

Application of the crack model to the flaw/strength relationship of Chapter 3 and 4 requires a knowledge of the size equivalence between the fracture-initiating defects and their resulting flaws (Ch. 2.1.1). Theoretical deductions (Ch. 2.3.1) suggest that the stress states developed by a spherical alumina inclusion embedded in a tetragonal zirconia matrix due to thermal contraction mismatch will induce radial cracking around the inclusions. However, thermal mismatch alone cannot predict the fracture behaviour as the significant elastic mismatch also plays a role under applied loads (Ch. 2.3.1). Direct experimental verification can clarify this issue. It is possible that the fracture-initiating alumina inclusion may develop a specific type of flaw before it extends into the matrix and fracture occurs. If so, other alumina inclusions local to the fracture origin should also develop the same type of flaw. This most likely occurs in the constant-stress region of the stressed four-point-bend bar (Ch. 2.5.1 (1)). A special experiment was therefore conducted to follow the flaw development

associated with the Al_2O_3 defects in the Al_2O_3-ZrO_2 composite.

6.2 Experimental Procedure

A thin layer (thickness $\simeq$ 0.2mm) of 10 vol% α-Al_2O_3 in t-ZrO_2 was sintered onto the surface of a pure Y-PSZ bar. The Al_2O_3-ZrO_2 composite powder was prepared by vibratory mixing 10 vol% α-Al_2O_3 powder[27] (size 1 to 20 μm) and the Y-PSZ[28] powder in methanol for 24 hours. The mixed powder was dried and ground and a thin layer laid uniformly on the bottom surface of the steel die. The die was then filled with the pure Y-PSZ powder and a composite bar was pressed, isopressed, burnout/re-isopressed and sintered (Ch. 3.3.2). The sintered, carefully finished specimens were four-point-bend tested with the composite layer as the tensile surface. The fracture surfaces of the broken specimens were SEM examined and those with alumina-fracture-origins separated out. The tensile surfaces of these specimens were polished to 1 μm and the α-Al_2O_3 inclusions around the identified fracture origin of each was examined.

6.3 Results and Discussion

Representative micrographs of the tensile surface

---

27. ALCAN, Kingston, Canada

28. Sedimented as per the procedure in Ch. 3.3.3.

near the fracture origin are shown in Fig. 6.1. Fig. 6.1(a) shows an internally fractured large alumina inclusion (≃ 12 μm). It has no associated crack extension into the matrix. Similar results are shown in Fig. 6.1(b) for a ≃ 20 μm alumina inclusion. The cracks appear to propagate intergranularly in the inclusion. In both cases, surrounding smaller alumina inclusions (1 to 5 μm) did not fracture. These results suggest that alumina inclusion fracture occurs under the combined thermal-contraction and elastic-mismatch stresses. The smaller alumina inclusions require higher stresses for fracture so they remain intact.

To further substantiate these findings, a series of micrographs were taken across the tensile surface. The results are shown in Fig. 6.2, wherein the maximum stress region has been marked and the position on the fractured specimen schematically shown. All internally-fractured alumina inclusions are 10 to 20 μm. Interfacial cracking occurred at some inclusions of irregular shape with higher aspect ratio (≃ 10). This could be associated with weaker interfaces from inefficient t-ZrO_2 powder/Al_2O_3 particle packing on pressing leading to unsound sintering. Radial cracking was not observed even around large-size inclusions. Inclusions in the tensile fiber-stress region were unfractured down to 50% of the maximum stress.

Experimental results suggest that alumina inclusion fracture occurs prior to global fracture. The most severe

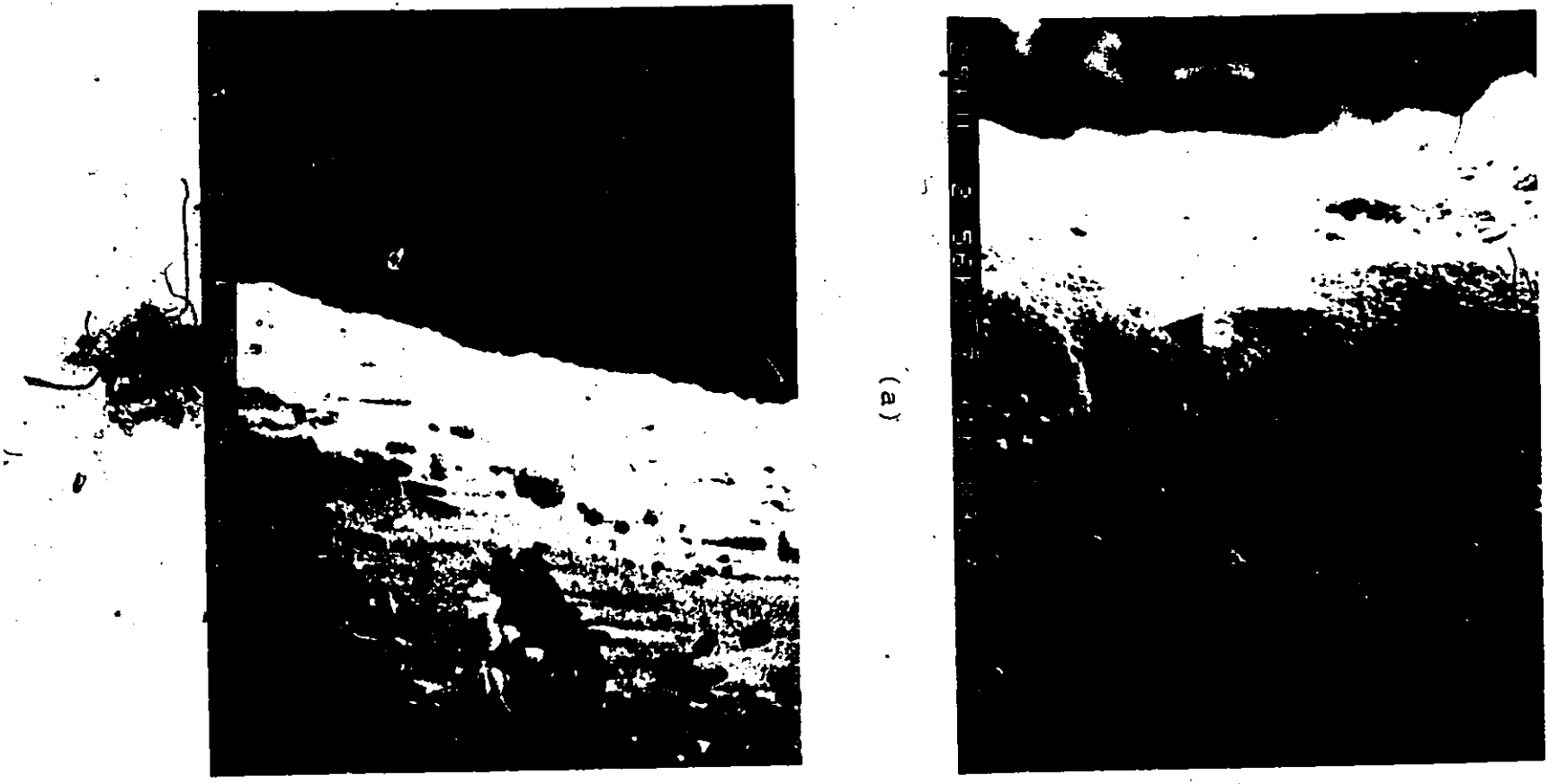

Fig. 6.1 Fracture of the alumina inclusions on the tensile surface of the ZrO_2-Al_2O_3 composite test bar, showing (a) a medium-sized unagglomerated inclusion (b) a large-sized agglomerated inclusion.

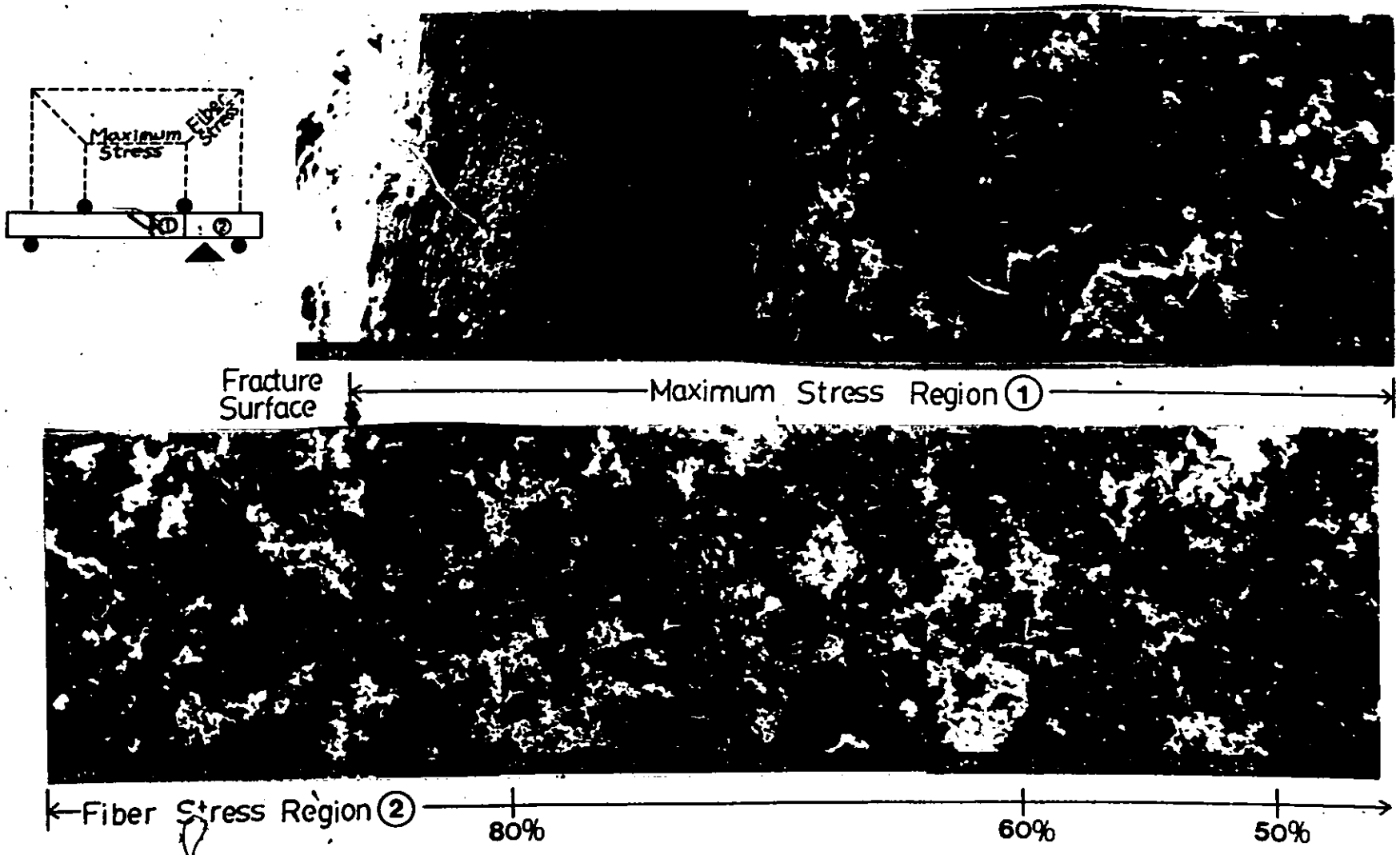

Fig. 6.2 Fracture of the alumina inclusion in the maximum- and fiber-stress region on the tensile surface of the ZrO_2-Al_2O_3 composite test bar.

fractured-inclusion flaw becomes the fracture origin. This is consistent with the microstructures of alumina fracture origins observed in Chapter 3 and verifies the valid application of the crack model for characterizing the flaw/strength relationships. Internal fractures observed in the large alumina inclusions ($z \simeq 10$ μm) are also consistent with the data of Chapter 3, i.e. all the observed fracture origins were $z \simeq 5.2 \times 10^{-3} m^{1/2}$ equivalent dimension, or an equivalent spherical radius of $\simeq 20$ μm. It is to be expected that the fracture-origin alumina inclusions will be the larger ones, i.e. those which can develop the longer (critical) flaws than the surrounding, smaller fractured ones. These results appear contrary to the theoretical deduction based solely on thermal contraction mismatch consideration. This implies that the elastic mismatch has a significant influence on the final stress state in the alumina-inclusion/tetragonal-zirconia-matrix system, i.e. the suppression of matrix radial cracking around the inclusions and reversal of the compression inside the inclusions to the tensile state. This will be analysed in detail in Chapter 8.

6.4 Conclusions

As the result of the present study the following conclusions can be made ;

(1) Preceding inclusion fracture occurs in the fracture-

initiating alumina inclusions > 10 μm size embedded in a tetragonal zirconia matrix.

(2) Use of the crack model to characterize flaw/strength relationships for alumina-inclusion fracture origins in tetragonal zirconia is valid.

CHAPTER 7

Valid K_{Ic} Determination via In-Test Subcritical Precracking of Chevron-Notched Bend Bar

7.1 Introduction

K_{Ic} measurement using chevron-notched-bar specimens is popular as precracking is unnecessary and fracture toughness data can be directly acquired. As discussed earlier (Ch. 2.5.2) low displacement rates can promote subcritical crack growth and overload is usually necessary for crack initiation. This invalidates the test. The present study investigated conditions for valid K_{Ic} testing using chevron-notched bars. Critical displacement rates required to avoid subcritical crack growth were determined and an in-test precracking technique was developed.

7.2 Theory

A four-point-bend-chevron-notched bar was used in the present study to gather room- and high-temperature fracture toughness data. The loading arrangement and specimen geometry are shown in Fig. 2.11. It has been mentioned (Ch. 2.5.2) that a particular stable crack growth will occur as the crack initially extends from the chevron tip. To use the maximum loads to compute the fracture

toughness values via Eqs. (2.29) and (2.30), stable crack growth must occur. This condition appears as a nonlinear region on the load-displacement curve between the initial elastic region and the final fracture. An overload $> P_{max}$ triggers immediate fast fracture based on the initial crack length, a_0, and results in an exclusively elastic region prior to fracture. This is unacceptable for valid K_{Ic} determination. A small overload $< P_{max}$ for crack initiation will give a "pop-in" (sudden crack extension) followed by stable crack extension. This still gives a valid K_{Ic} value. These three conditions are schematically shown in Fig. 7.1 (Type I-III) and are consistent with previous experimental results [Himsott, 1987]. Precracking of the chevron-notched bar $\leq a_m$ will produce a load-displacement curve of Type IV in Fig. 7.1, i.e. a truncated stable-crack-growth region of the Type III curve following the higher-compliance elastic region characteristic of the precrack length.

Based on the characteristics of subcritical crack growth in ceramics (Ch. 2.5.2), an in-test precracking procedure can be first carried out by applying a load that induces the appropriate stress intensity level for subcritical crack growth. The K_{Ic} test then follows. The subcritical precracking utilizes an appropriate displacement rate chosen experimentally by detecting the compliance change following the initial elastic region of the load-displacement curve. Once subcritical precracking has been

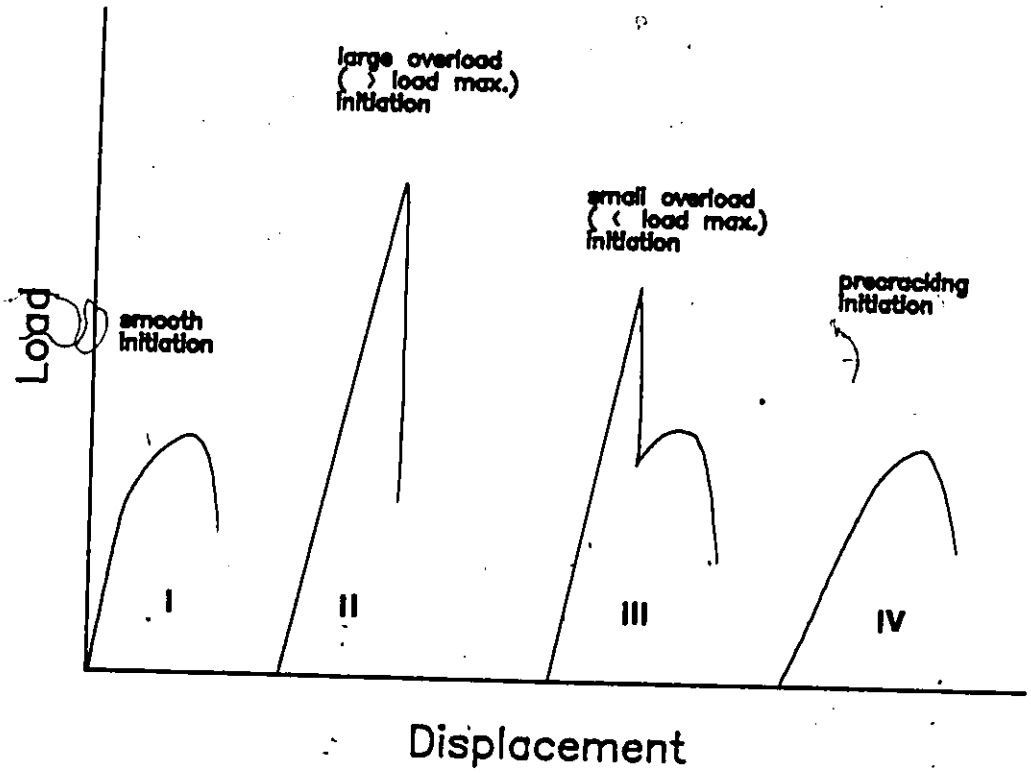

Fig. 7.1 Room-temperature load-displacement curves for different crack initiation conditions in a chevron-notched bend bar.

achieved, the displacement rate is increased to that for fast fracture. The total testing procedure therefore involves two-step control of the machine crosshead speed. A valid K_{Ic} test is assured.

7.3 Experimental Procedure

Chevron-notched bend bars were prepared from the 4.5 wt% Y-PSZ powder as per the processing procedure of Ch. 3.3.3. Specimens were cut and machined to 3 x 4 x 25 mm and chevron notches were cut with a thin diamond blade to $\alpha_0 = 0.5$ and $\alpha_1 = 1.0$. The slot width was 150 μm. The machined specimens were annealed in air at 1400°C for 30 minutes to remove any surface residual stress and were tested in a four-point-bend fixture (Ch. 3.3 and 5.3.1). Load was monitored by a piezoelectric load-cell and displacement was recorded by an LVDT device with an accuracy ± 0.001%[29]. The crosshead speed was steplessly controlled between 10^{-4} and 5 mm/min. Experiments were performed in two parts : appropriate crosshead speeds for fast fracture and subcritical precracking were determined for each temperature then K_{Ic} tests were performed starting with subcritical precracking using the predetermined crosshead speeds. When the recorded load-displacement curves deviated from a straight line (elastic region), the crosshead speed was

---

29. Schenvitz 100 DC-D, U.S.A.

quickly changed to that predetermined for fast fracture. Tests then proceeded to final fracture and P_{max} was recorded. K_{Ic} values were computed from Eqs. (2.29) and (2.30). Tests were conducted between room temperature (RT) and 1000°C at 200°C intervals. Complete thermal equilibrium was established before each test.

7.4 Results and Discussion

Typical room-temperature load-displacement curves for different crosshead speeds are shown in Fig. 7.2. Above ≃ 0.05 mm/min, the curves exhibit linear elastic regions to final fracture, i.e. Type II curve of Fig. 7.1. This speed was identified as the minimum fast-fracture speed. Between ≃ 0.05 and ≃ 0.003 mm/min, a gradual change from linear to nonlinear response was detected . The extent of nonlinearity is considered insufficient for precracking. Below ≃ 0.003 mm/min, the curves exhibit pronounced nonlinearity and is considered satisfactory. This speed was identified as the maximum subcritical-crack-growth speed. The minimum fast-fracture (FF) and the maximum subcritical crack growth (SCG) speeds for 4.5 wt% Y-PSZ at various temperatures are listed in Table 7.1.

The existence of subcritical crack growth below a particular displacement rate depends on the material and its environment. A previous study showed that Y-PSZ exhibited subcritical crack growth in the atmosphere at a sufficiently

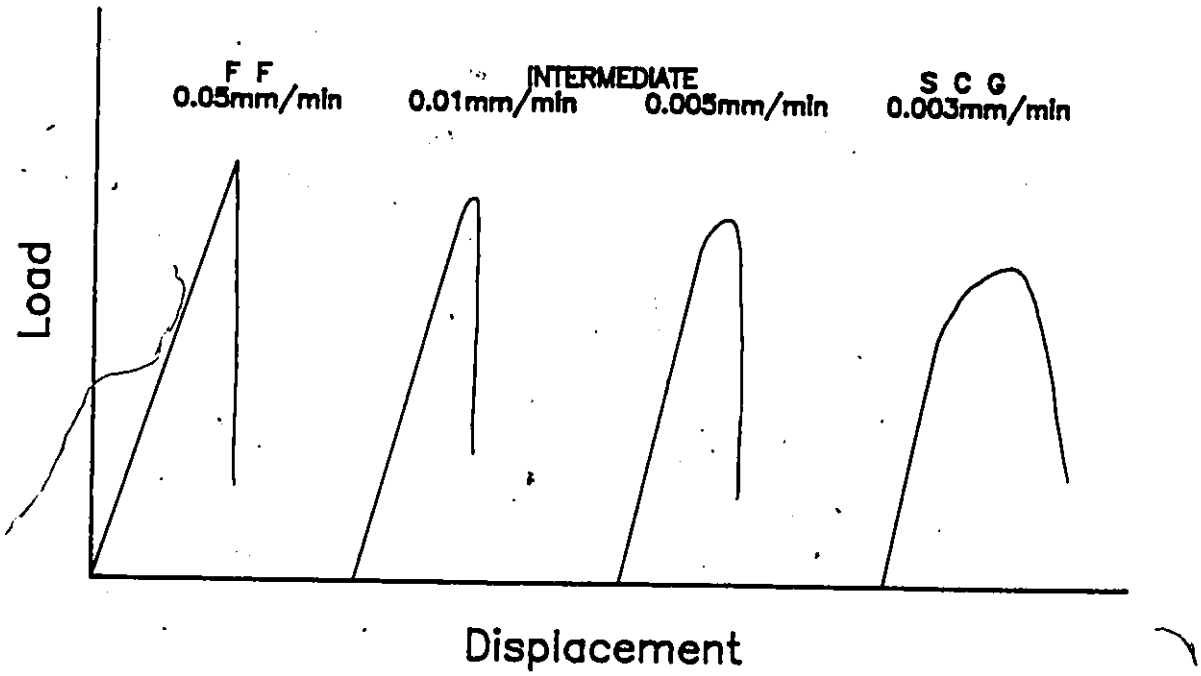

Fig..7.2 Various types of load-displacement curves due to different crosshead speeds for a chevron-notched bend bar.

Table 7.1 Maximum subcritical crack growth (SCG) crosshead speed and minimum fast fracture (FF) crosshead speed for chevron-notched bend bars from RT - 1000°C.

Crosshead speed / Temperature	SCG (mm/min)	FF (mm/min)
Room temp.	0.003	0.05
200°C	0.003	0.05
400°C	0.002	0.08
600°C	0.001	0.10
800°C	0.0008	0.20
1000°C	0.0005	0.30

low crosshead speed (Ch. 2.5.2). Moisture appeared the active environmental factor. For materials not sensitive to the atmosphere, a specific corrosive environment can be introduced to produce practical subcritical crack growth. The maximum SCG speed decreases with rising temperature, implying a lowering of the threshold K_I with temperature. This is consistent with the reported high-temperature behavior of ceramics [Evans, 1983]. Higher minimum-FF-speeds are required at higher temperatures, an observation similar to those for high-temperature tensile and flexure tests [Quinn, 1984]. A typical load-displacement curve using subcritical precracking via the two-step crosshead speed control technique is shown in Fig. 7.3. No precise control

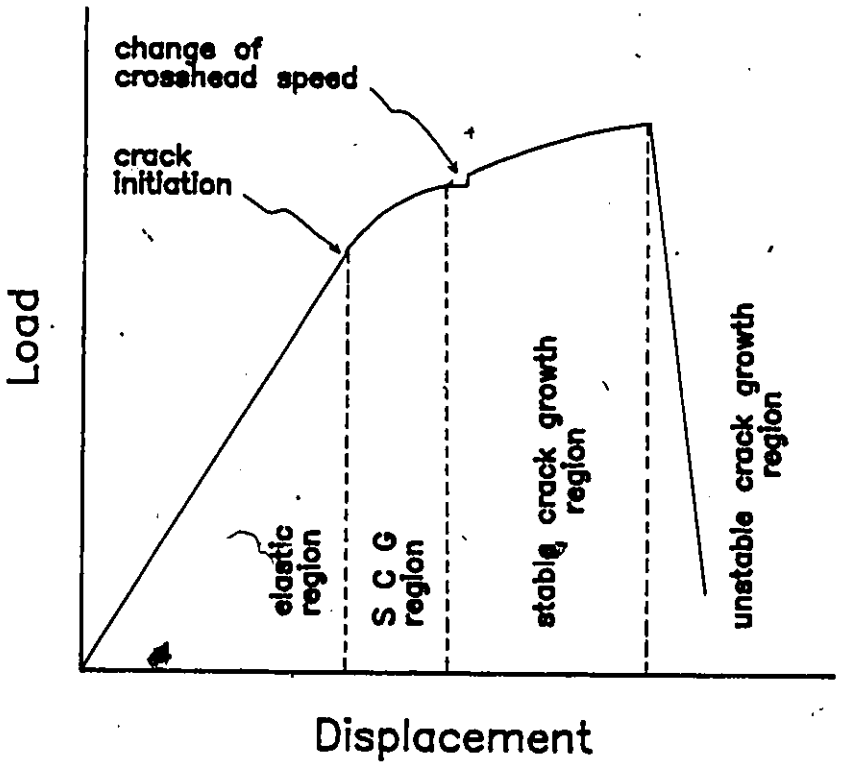

Fig. 7.3 A load-displacement curve for chevron-notched bend bar using displacement rate control and subcritical precracking.

of precrack length (extent of subcritical crack growth) is necessary. The subcritical precracking serves to facilitate crack initiation and any precracking extent < α_m (the crack extension corresponding to P_{max}) is acceptable. This is judged by the occurrence of a subsequent stable-crack-growth region. The K_{Ic} values determined by this technique at various temperatures for 4.5 wt% Y-PSZ are shown in Fig. 7.4. The deviation for each set of K_{Ic} values (five specimens) is ≤ 5% and the valid-test-rate is 100%.

The internal accuracy and consistency of the test data suggest the usefulness of the present technique. This is the first time that K_{Ic} measurements have been determined at elevated temperatures for 4.5 wt% Y-PSZ using chevron-notched bar specimens. Comparison of the present results with those of previous studies [Lange, 1982c, 1986c; Masaki, 1986; Mecartney, 1987; Ruhle, 1984; Tsukuma, 1984, 1985a] using other techniques for 4.5 wt% (2.5 mol%) Y-PSZ at room or elevated temperatures is shown in Fig. 7.5. The present data agree well with most previous results at room temperature using indentation or indentation-strength techniques. The decrease of K_{Ic} with temperature is similar to that observed by Lange [1982c].

7.5 Summary

An in-test subcritical-precracking technique has been developed for K_{Ic} determination using chevron-notched-

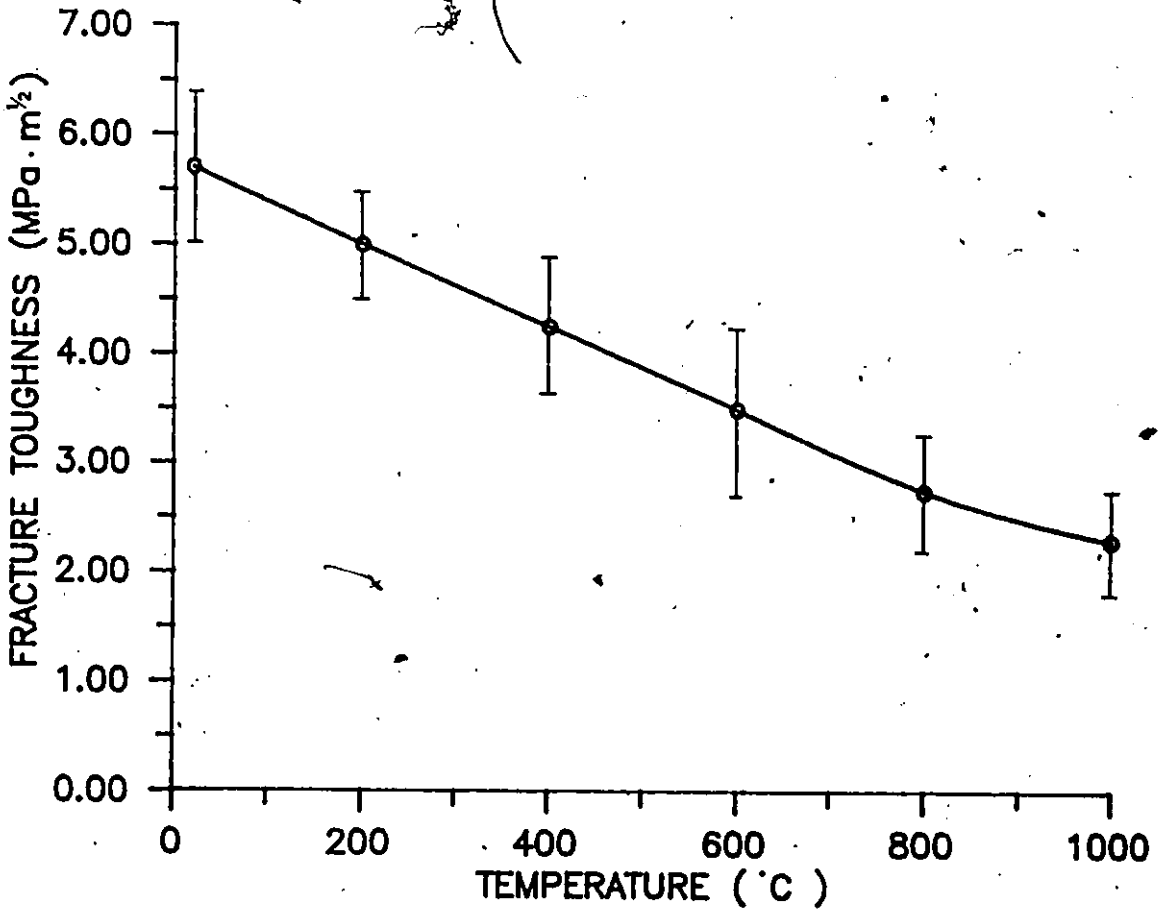

Fig. 7.4 Fracture toughness - temperature plot for 4.5 wt% Y-PSZ ceramics.

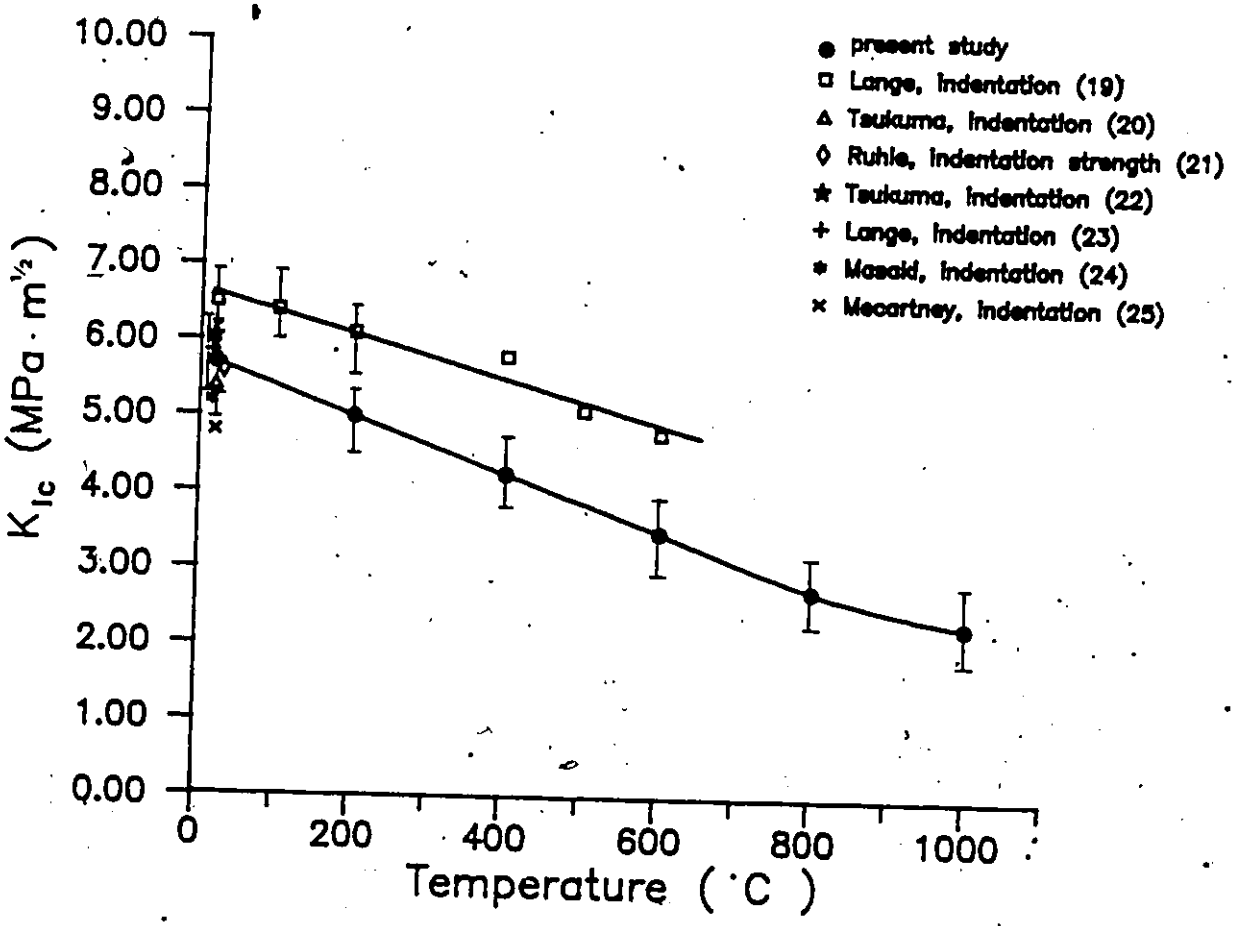

Fig. 7.5 Comparison of K_{Ic} data for 4.5 wt% (2.5 mol%) Y-PSZ of present study with previous results

bend-bar . The technique was applied to a 4.5 wt% Y-PSZ and was shown to be a simple and reliable testing method. This technique enables the chevron-notched specimen to be used for valid K_{Ic} determination of ceramic materials at room and elevated temperatures.

CHAPTER 8

An Inclusion-Initiated Fracture Model for Ceramics

8.1 Introduction

Linear elastic fracture mechanics relates the fracture stress to the critical defect dimensions for ceramic materials (Ch. 2.1.1). The fracture-initiating defects that commonly exist in ceramics are inclusions, agglomerates, pores and machining flaws (Ch. 2.1.2). It has been recognized that these defects initiate fracture differently (Ch. 2.1.1) and in Chapter 4 the relative severity of the defect types was quantitatively ranked. Thermal contraction mismatch may cause cracks to develop inside or around defects and upon application of external stresses, the local stresses may be further modified by elastic mismatch (Ch. 2.3.1). Inclusion-defects have been extensively studied with respect to microcracking phenomena but little analysis exists on their influence on strength. Previous analysis by Evans [1975] and Green [1982] were restricted to a through-the-thickness crack or neglected perturbation of stress fields by crack extension (Ch. 2.3.1). For a part-through crack experiencing residual stresses that are partially relaxed by microcracking, a more rigorous analysis is necessary. The present study analyzed a

part-through-the-thickness crack in a typical inclusion-initiated fracture of a ceramic material. The inclusion/matrix relationships considered were $\alpha_i < \alpha_m$, $K_{oi} < K_{cm}$ and $E_i > E_m$ which represent some common inclusion-matrix systems, i.e. α-Al_2O_3 in tetragonal ZrO_2(t-ZrO_2), SiC in α-AlO_3 and Si_3N_4 in t-ZrO_2. The weight function method (Ch. 2.3.2) is used to compute the residual-stress-intensity-factors. The predicted strength is compared with experimental data for the α-AlO_3/t-ZrO_2 system (Ch. 4) and the T_g for t-ZrO_2 is theoretically determined.

8.2 The Inclusion Fracture Model

The microstructure evidence of Chapter 3 and the experimental results of Chapter 6 suggest that α-Al_2O_3 inclusion fracture occurs before α-Al_2O_3-defect-initiated fracture of t-ZrO_2. This is not predicted by thermal contraction mismatch analysis (Ch. 2.3.1), suggesting a substantial influence of the elastic mismatch. An inclusion-fracture model was therefore constructed.

A spherical inclusion of radius R embedded in an infinite matrix subjected to a remote uniform tension σ_∞ is shown in Fig. 8.1. Owing to the lower thermal expansion coefficient of the inclusion, a hydrostatic residual compressive stress of magnitude σ_T develops inside the inclusion upon cooling as shown in Eq. (2.12). Since the magnitude of T_g for t-ZrO_2 is known (Ch. 5.4), σ_T can be

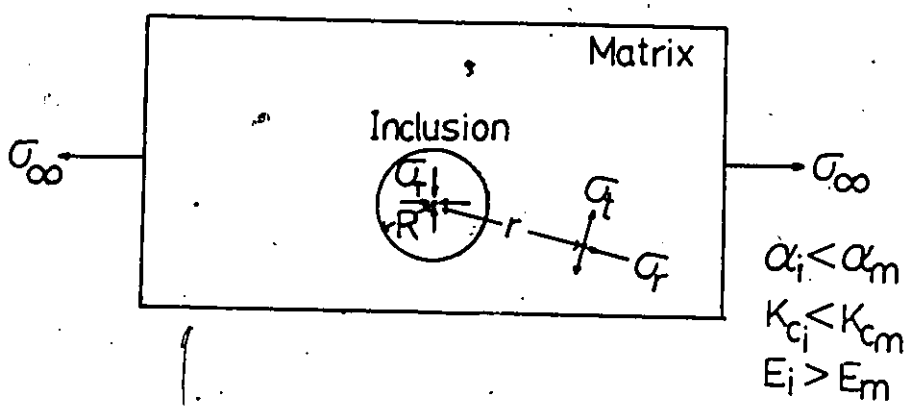

Fig. 8.1 A spherical inclusion embedded in a matrix with thermal and elastic mismatch.

calculated. The magnitude of σ_T is $\simeq$ 0.4 to 0.6 times the fracture stress (from Ch. 3). The radial compression (σ_r) and tangential tension (σ_t) in the matrix a distance r from the inclusion center are shown in Eqs. (2.13). At the inclusion/matrix interface, $\sigma_r^m = -2\sigma_t^m = \sigma_T$, where the superscript m denotes the maximum magnitude. The maximum components of these interfacial residual stresses in the direction of the remote tension (at AA', BB') are shown in Fig. 8.2(a). The residual tangential tensile stress at the interface can induce radial microcracking. The occurrence and degree of such microcracking will depend on the magnitude of σ_T, the size of the inclusion (R) and the size of preexisting flaws at the interface (Ch. 2.3.1). A minimum critical inclusion size (R_c^{min}) exists, below which microcracking will not occur. If it does occur, residual stresses will be partially relieved. The radial microcracks generated when $R > R_c^{min}$ are also shown in Fig. 8.2(a). Upon application of an external load, additional elastic-mismatch stresses develop associated with the inclusion (Ch. 2.3.1). The stress concentration within the inclusion, ξ_i, is given by Eq. (2.17). In the present analysis, it is assumed that ν = 0.25 and E_i/E_m = 1 to 5, giving ξ_i = 1 to 1.55. The stress concentration around the inclusion is greatest at the interface. The magnitude and direction of these additional elastic stresses were exemplified for a perfect rigid inclusion (Ch. 2.3.1), and are indicated in Fig. 8.2(b).

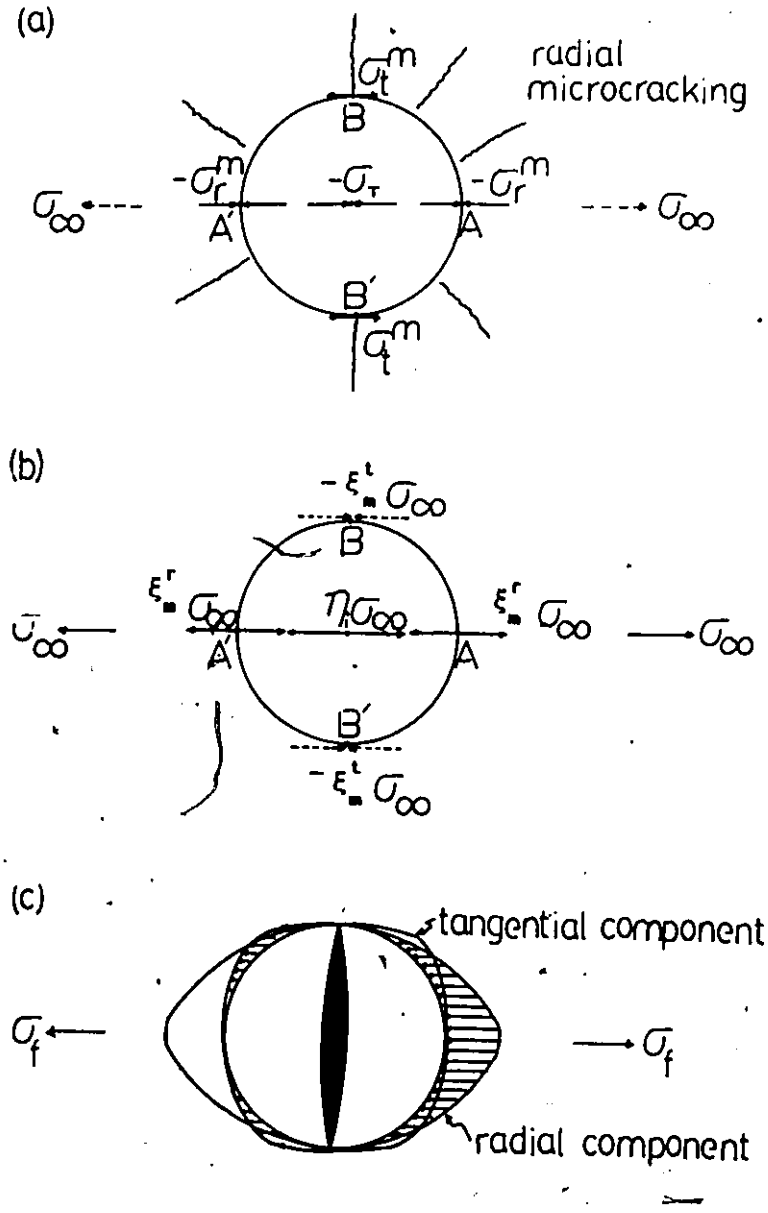

Fig. 8.2 (a) Maximum components of thermal mismatch stresses σ_r, σ_t, and σ_T in the direction of σ_∞ and the occurrence of radial microcrackihg for $R > R_c^{min}$ (b) Maximum elastic mismatch stress inside and at inclusion/matrix interface (c) Propagation and arrest of a central microcrack under the resultant stresses and the recovered thermal mismatch stress distribution at the interface in the direction of σ_∞.

A radial tension exists at AA' with a stress concentration $\xi_m^r \simeq 1.96$ for $\nu = 0.25$ (Eq. (2.18)). At BB', there is a tangential compression with a stress concentration $\xi_m^t = -0.03$ for $\nu = 0.25$ (Eq. (2.19)). The magnitude of ξ_m^r and ξ_m^t for an inclusion with $E_i/E_m = 1$ to 5 in the present analysis are expected to be less than those for a perfect rigid inclusion. These may be estimated as follows : since the radial stresses should be continuous from inside the inclusion to the interface (AA'), $\xi_m^r = \xi_i = 1$ to 1.55. ξ_m^t are calculated for $E_i/E_m = 1$ to 5 and values not much less than zero are obtained (eg. $\xi_m^t = -0.019$ for $E_i/E_m = 2$). The magnitude of ξ_m^t can be reasonably taken as zero. These elastic stress states are as shown in Fig. 8.2(b). The resultant stress states are then obtained by superimposing the residual stresses of Fig. 8.2(a) upon the elastic stresses of Fig. 8.2(b). When σ_∞ approaches the fracture stress of the matrix, σ_f, the radial residual stresses and elastic stresses balance at AA' and inside the inclusion, leaving a tensile stress of magnitude 0.5 to 1.0 σ_f. At BB' the resultant stress is still 0.2 to 0.3 σ_f in tension. The significance of these local stresses depends on the fracture-toughness and the distribution of flaws within the inclusion, matrix and interface [Evans, 1980a]. As $K_{ci} < K_{cm}$ and K_c of the interface is expected to be between K_{ci} and K_{cm}, a crack will most probably initiate from a preexisting critical flaw within the inclusion and extend to the

interface (as observed in Ch. 6). It now encounters the higher fracture resistance of the matrix and therefore arrests. The crack may only extend further when the stress intensity reaches the fracture toughness of the matrix. This intermediate crack arrest is shown in Fig. 8.2(c). As the inclusion has suffered complete fracture, the elastic mismatch stresses no longer exist and only residual stresses originating from the thermal mismatch exist exclusively. These residual radial and tangential stress components in the direction of applied stress are shown in Fig. 8.2(c).

8.3 Crack Extension Characterization

Because the inclusion fractures and the crack arrests, this crack will act as the fracture-initiator for the matrix and can be analyzed by the "part-through elliptical crack extension model" (Ch. 2.1.1). In the present analysis, a part-through crack is subject to local residual stresses and a remote applied stress. Due to the axi-symmetric nature of the former and tension of the latter, the opening mode of fracture is exclusively involved. Crack extension into the matrix is thus characterized by the stress intensity factor obtained by superimposing the residual- and applied-stress intensity factors along the crack front (Ch. 2.3).

8.3.1 The Part-Through Elliptical Crack Extension Model

This model (Ch. 2.1.1) computes the stress intensity factor for an elliptical crack in the interior (or a semi-elliptical crack at the surface) of a finite plate subjected to a uniform tension (σ) perpendicular to its elliptical axes (a and c). The maximum K_I along the crack front (K_I^m) is given by ;

$$K_I^m = \frac{Y\sqrt{1-\nu^2}}{\Phi}\,\sigma\sqrt{a} \qquad \text{,for } a \le c \qquad (8.1a)$$

$$K_I^m = \frac{Y\sqrt{1-\nu^2}}{\Phi}\,\sigma\sqrt{c} \qquad \text{,for } a \ge c \qquad (8.1b)$$

In the absence of any loading other than the applied load, the crack will initiate when the fracture toughness of the matrix (K_{Ic}) is reached, i.e.;

$$K_I^m = K_{Ic} = \frac{Y\sqrt{1-\nu^2}}{\Phi}\,\sigma_f\sqrt{a} \qquad (8.2)$$

where σ_f is the fracture stress and a is the minor crack dimension. Eq. (8.2) has been successfully used to characterize the strength/flaw-dimension relationships in previous Chapters [3 and 4]. A "defect severity parameter" (X) was defined and incorporated for the relative severity of the defect types in terms of the strength of ceramics, i.e. (in plane strain) ;

$$\frac{K_{Ic}}{\sqrt{1-\nu^2}} = \sigma_r \cdot X \cdot \frac{Y\sqrt{a}}{\Phi} \qquad (4.2b)$$

The theoretical value of X in Eq. (4.2b) will now be calculated via the model established.

8.3.2 Residual Stress Intensity Factor

A weight function method (Ch. 2.3.2) is used to determine the residual stress intensity factor arising from the thermal and elastic mismatches of the defect and its matrix. A weight function (h) for a two-dimensional crack symmetrical about the x-axis and extending in the x-direction is given by ;

$$h(x,a) = \frac{H}{2K_I^{(1)}} \frac{\partial \mu(x,a)}{\partial a} \qquad (2.20)$$

where μ is the crack opening displacement along the crack surface perpendicular to the x-axis, a the crack length, $K_I^{(1)}$ the stress intensity factor for a known symmetric loading (System (1)) and H = E (Young's modulus) for plane stress and H = $E/(1-\nu^2)$ for plane strain. The stress intensity factor, $K_I^{(2)}$, for another symmetric loading (System (2)) with stress, $\sigma_s(x)$, acting along the surface of the same crack geometry is given by ;

$$K_I^{(2)} = \int_0^a \sigma_s(x)\, h(x,a)\, dx \qquad (2.21)$$

The final expressions for $K_I^{(2)}$ along the crack front of a two-dimensional crack and a three-dimensional crack (the elliptical crack of the present analysis) at the ends of the semi-axes can be derived (Appendix D) ;

$$K_I^{(2)} = \frac{H}{K_I^{(1)}} \int_0^a \sigma_s(x)\, \frac{\partial \mu(x,a)}{\partial a}\, dx \qquad \text{(2-D crack)} \qquad (8.3a)$$

$$K_I^{(2)} = \frac{H}{K_I^{(1)}} \frac{8}{\pi c} \int_{y=0}^{c} \int_{x=0}^{a\sqrt{1-(y^2/c^2)}} \sigma_s(x,y)\, \frac{\partial \mu(x,y,a,c)}{\partial a}\, dx\, dy$$

(3-D crack at the ends of a-axis) (8.3b)

The maximum residual stress intensity factor (K_{Ir}^m) in the present analysis can be computed from the maximum applied stress intensity factor (K_I^m) (Eq. (8.2)) and the crack opening displacement of a reference system, i.e., the known Irwin solution [Irwin, 1962] ;

$$\mu = \frac{2\sigma a(1-\nu^2)}{E\Phi} \left(1 - \frac{x^2}{a^2} - \frac{y^2}{c^2}\right)^{1/2} \quad \text{, for } a \le c \qquad (8.4)$$

The magnitude and distribution of the residual stresses along the crack surface are obtained by superimposing the radial and tangential stress components at the inclusion/

matrix interface in the direction of the applied stress since these stress components are responsible for fracture. This process is illustrated in Fig. 8.3. The origin of the coordinate system is set at the inclusion center and the stresses vary between $-\pi/2 \leq \theta \leq \pi/2$ (or $-a \leq x \leq a$). The radial stress component is $-\sigma_T \cos(\pi x/2a)$ and the tangential stress component is $(1/2)\,\sigma_T\,|\sin(\pi x/2a)|$ (σ_T is the hydrostatic stress inside the inclusion as defined in Eq. (2.12)). The resultant residual stress in two-dimensions is : $\sigma_T\,[(1/2)|\sin(\pi x/2a)| - \cos(\pi x/2a)]$ and, to facilitate mathematical treatment, this is approximated by the polynomial; $\sigma_T[0.82(\pi x/2a)^{4/3} - 1]$ (shown in Fig. 8.3). Since radial microcracking ($R > R_c^{min}$) could partially relieve the residual stress, a "residual stress relief function", S, may be defined as the ratio of the relieved to the unrelieved residual stress. The residual stress distribution along the semi-axis ($-c \leq y \leq c$), i.e. y-z plane, assume the same shape as in the x-z plane so leading to the final form in three-dimensions ;

$$\sigma_S = -\sigma_T S\,[0.82(\pi x/2a)^{4/3} - 1]\,[0.82(\pi y/2c)^{4/3} - 1]$$

$$\text{with } -a\sqrt{1-(y^2/c^2)} \leq x \leq +a\sqrt{1-(y^2/c^2)}\,,\ -c \leq y \leq +c \qquad (8.5)$$

"S" is a function of the inclusion size. For a spherical inclusion, a = c = R, Eq. (8.4) gives ;

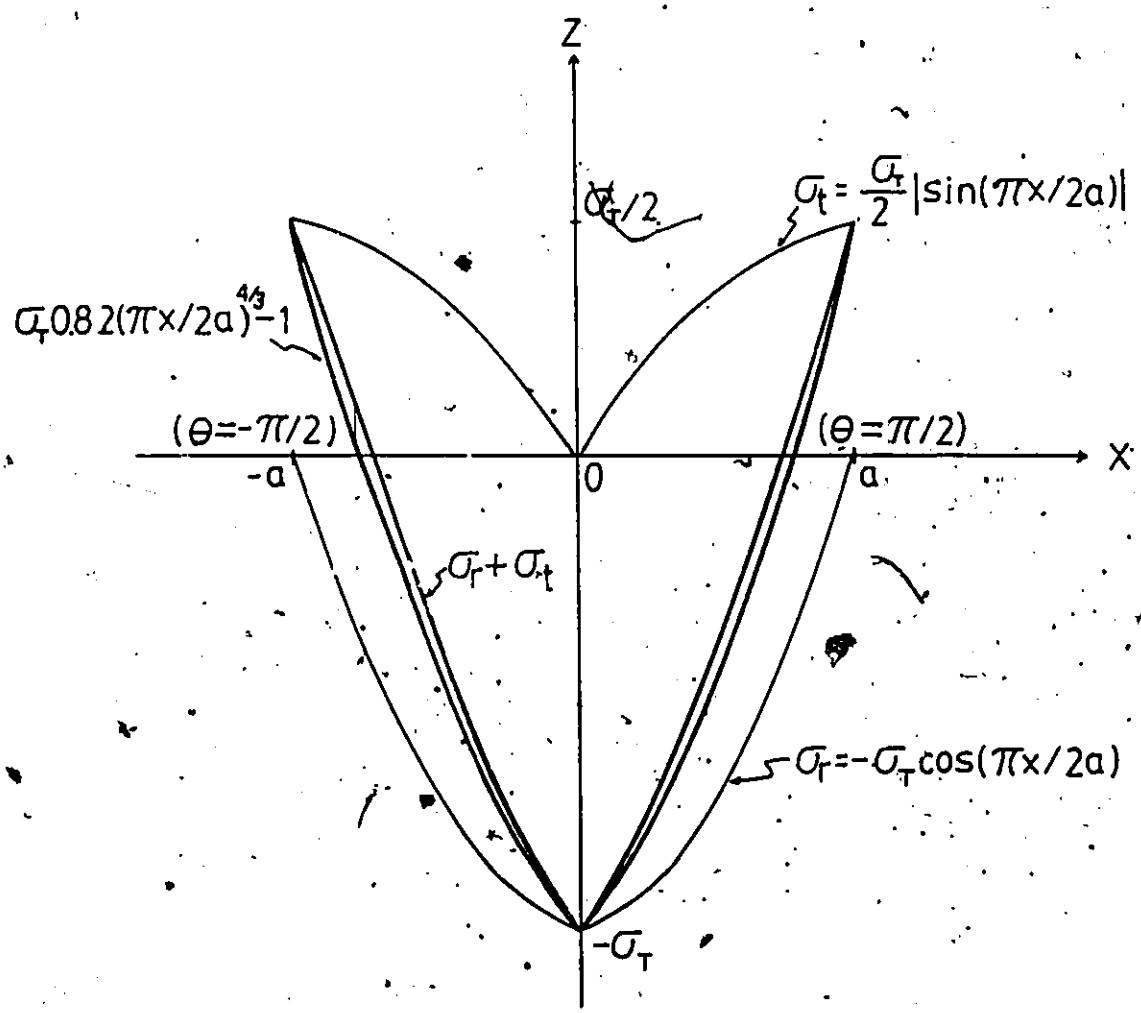

Fig. 8.3 The radial and tangential residual stress components in the x-axis direction, their resultant stresses and their approximation by a polynomial.

$$\frac{\partial \mu}{\partial R} = \frac{2\sigma(1-\nu^2)}{E\Phi} \left(1 - \frac{x^2+y^2}{R^2}\right)^{-1/2} \qquad (8.6)$$

and Eq. (8.5) gives ;

$$\sigma_s = -\sigma_T S\{2.24(xy/R^2)^{4/3} - 0.82[(\pi x/2R)^{4/3}+(\pi y/2R)^{4/3}]+1\} \qquad (8.7)$$

Substituting Eq. (8.2), (8.6) and (8.7) into Eq. (8.3b), the maximum residual stress intensity factor is ;

$$K^m_{Ir} = \frac{E/(1-\nu^2)}{Y\sigma\sqrt{R}\sqrt{(1-\nu^2)/\Phi}} \frac{8}{\pi R} \int_{y=0}^{R} \int_{x=0}^{\sqrt{R^2-Y^2}} \sigma_T S\Big\{2.24(xy/R^2)^{4/3} - 0.82[(\pi x/2R)^{4/3} + (\pi y/2R)^{4/3}] + 1\Big\} \left[\frac{2\sigma(1-\nu^2)}{E\Phi}\left(1 - \frac{x^2+y^2}{R^2}\right)\right] dx\, dy \qquad (8.8)$$

The analytical solution of this equation is given in Appendix E and is;

$$K^m_{Ir} = \frac{-1.5\ \sigma_T\ S}{Y\sqrt{1-\nu^2}} \sqrt{R} \qquad (8.9)$$

The resultant maximum-stress-intensity-factor (K^m_{It}) is obtained by combining Eq. (8.2) and Eq. (8.9), i.e.;

$$K^m_{It} = K^m_I + K^m_{Ir}$$

$$= \frac{Y\sigma\sqrt{1-\nu^2}}{\Phi}\sqrt{R} - \frac{1.5\,\sigma_T^{\sim}\,S}{Y\sqrt{1-\nu^2}}\sqrt{R} \qquad (8.10)$$

which rearranges for the elliptical crack model to give ;

$$\frac{K_{It}^{m}}{\sqrt{1-\nu^2}} = \left[\sigma - \frac{1.5\Phi\,\sigma_T S}{Y^2(1-\nu^2)}\right]\cdot\frac{Y\sqrt{R}}{\Phi} \qquad (8.11)$$

The criteria for crack extension in the presence of local residual and remote tensile stresses is then ;

$$\frac{K_{Ic}^{*}}{\sqrt{1-\nu^2}} = \left[\sigma_{of} - \frac{1.5\Phi\,\sigma_T S}{Y^2(1-\nu^2)}\right]\cdot\frac{Y\sqrt{R}}{\Phi} \qquad (8.12)$$

where K_{Ic}^{*} is the apparent fracture toughness of the matrix and is associated with the specific defect type (Ch. 4.4) and σ_{of}, the fracture stress in the absence of a residual stress.

8.4. Discussion

From Eq. (8.12), the fracture strength (σ_f) of a ceramic matrix containing a typical inclusion of radius R is given by ;

$$\sigma_f = \sigma_{of} - \frac{1.5\Phi\,\sigma_T S}{Y^2(1-\nu^2)} \qquad (8.13)$$

The first term is the fracture stress associated with a residual-stress-free fracture origin (e.g. a pore of radius R), and the second term ;

$$\frac{1.5\Phi\ \sigma_T S}{Y^2(1-\nu^2)}\ \left(=\sigma_e\right) \qquad (8.14)$$

represents the influence of the residual stress. From the principle of superposition (Ch. 2.3.2), σ_e can be regarded as an equivalent remote stress transferred from the crack line. This supports the previous argument and the expression for the relative defect severity, i.e.;

$$X = 1 + \frac{\sigma_e}{\sigma_f} \qquad (5.3)$$

Therefore fracture origins associated with local compressive residual stresses result in an underestimation of the fracture stress based exclusively on the defect size, i.e. these defects are less severe than their size predicts. Tensile residual stresses lead to fracture stress overestimation and a more severe condition. This is consistent with the experimental results and explanation in Chapter 4.--

To compute the strength, the residual stress relief function (S) must be evaluated. This is done in the present analysis by considering the strain energy release rate for

an annular crack around an inclusion (Appendix F) and the result is ;

$$\begin{cases} S = [K_c^2 \omega / E\beta(1 - \nu^2)\sigma_T^2]^{1/2} \cdot (1/\sqrt{R}) & \text{, for } R \geq R_c^{min} \\ S = 1 & \text{, for } R < R_c^{min} \end{cases} \quad (8.15)$$

where K_c is the fracture toughness of the matrix, ω the normalized crack size, E and ν are the Young's modulus and Poisson's ratio of the matrix respectively. $\beta = [(1 + \nu_m)/2E_m + (1 - 2\nu_i)/E_i]$, σ_T is the hydrostatic residual stress in the inclusion and R_c^{min} is the minimum critical radius below which microcracking will not occur.

8.5 Applications

8.5.1 T_g Prediction

T_g, the temperature below which existing residual stresses are no longer relaxed by diffusion or viscous flow, was experimentally determined in Chapter 6. It is $\simeq 1135^{\circ}C$ for the Y-PSZ ceramic. T_g can be theoretically computed using the present model. The X values and the corresponding σ_f for α-Al_2O_3 defects in the previous studies are substituted into Eq. (5.3) to acquire σ_e and this and the calculated S function values (from Eq. (8.15)) are substituted into Eq. (8.14) to obtain σ_Ts. T_g values can then be determined from Eq. (2.12). The experimental data and the computed results for the α-Al_2O_3 defects are listed

in Table 8.1. The average value for T_g is 1114 ± 34°C, in good agreement with the experimental value.

8.5.1 Strength Prediction

To check the validity of the model for strength prediction, the α-Al_2O_3/t-ZrO_2 inclusion-matrix system was examined. The values of various parameters utilized are as follows ;

α_i= 8.0 x 10^{-6}/°C; α_m= 10.0 x 10^{-6}/°C; E_i= 400 GPa; E_m= 220 GPa; $\nu_i = \nu_m$= 0.25; K_c(t-ZrO_2) = 4.5 MPa·$m^{-1/2}$ [an intrinsic K_{Ic} for a small flaw, Ch. 4.4]; Φ = 1.57 [spherical shape, Ch. 3.2]; Y = 1.86 [an average of the subsurface and surface crack, Ch. 3.2]; T_g= 1115°C [from the present study]; ω, the normalized preexisting flaw size is taken as 0.3 - 0.5, following the studies of Ito [1980] and Green [1981].

The above parameter values were substituted into Eq. (8.13) and (8.15), and the range of predicted strength plotted. The resultant predicted strength curve together with the experimental data are shown in Fig. 8.4. The agreement is good.

The value of "defect severity parameter" (X) can also be theoretically computed using Eq. (5.3) and (8.14). The result for the α-Al_2O_3/t-ZrO_2 system is X = 0.67 ± 0.03, in good agreement with the experimentally determined value of 0.66 (Ch 4.4).

Table 8.1 Fracture data and computed results of X, S and T_g for α-Al_2O_3 defects in t-ZrO_2 matrix at elevated temperature.

Temperature(°C)	Sample #	Fracture Stress (MPa)	Defect Dimension (μm)		Y	Φ	$Y\sqrt{a}/\Phi$ (x$10^3 m^{1/2}$)	X	S	T_g(°C)
			c	a						
200	4704	1047	25.5	14.0	1.77	1.243	5.329	0.71	1.00	1163
400	4706	996	28.5	13.7	1.77	1.199	5.465	0.73	1.00	1090
400	4909	764	24.3	12.7	1.94	1.225	5.641	0.79	0.93	1091
600	4907	550	25.0	15.8	1.94	1.299	5.938	0.85	0.63	1070
800	5007	388	33.1	17.3	1.85	1.226	6.279	0.90	0.43	1123
1000	5103	321	252.0	9.6	1.94	1.003	5.991	0.95	0.48	1149
									Ave. $T_g = 1114 \pm 34$	

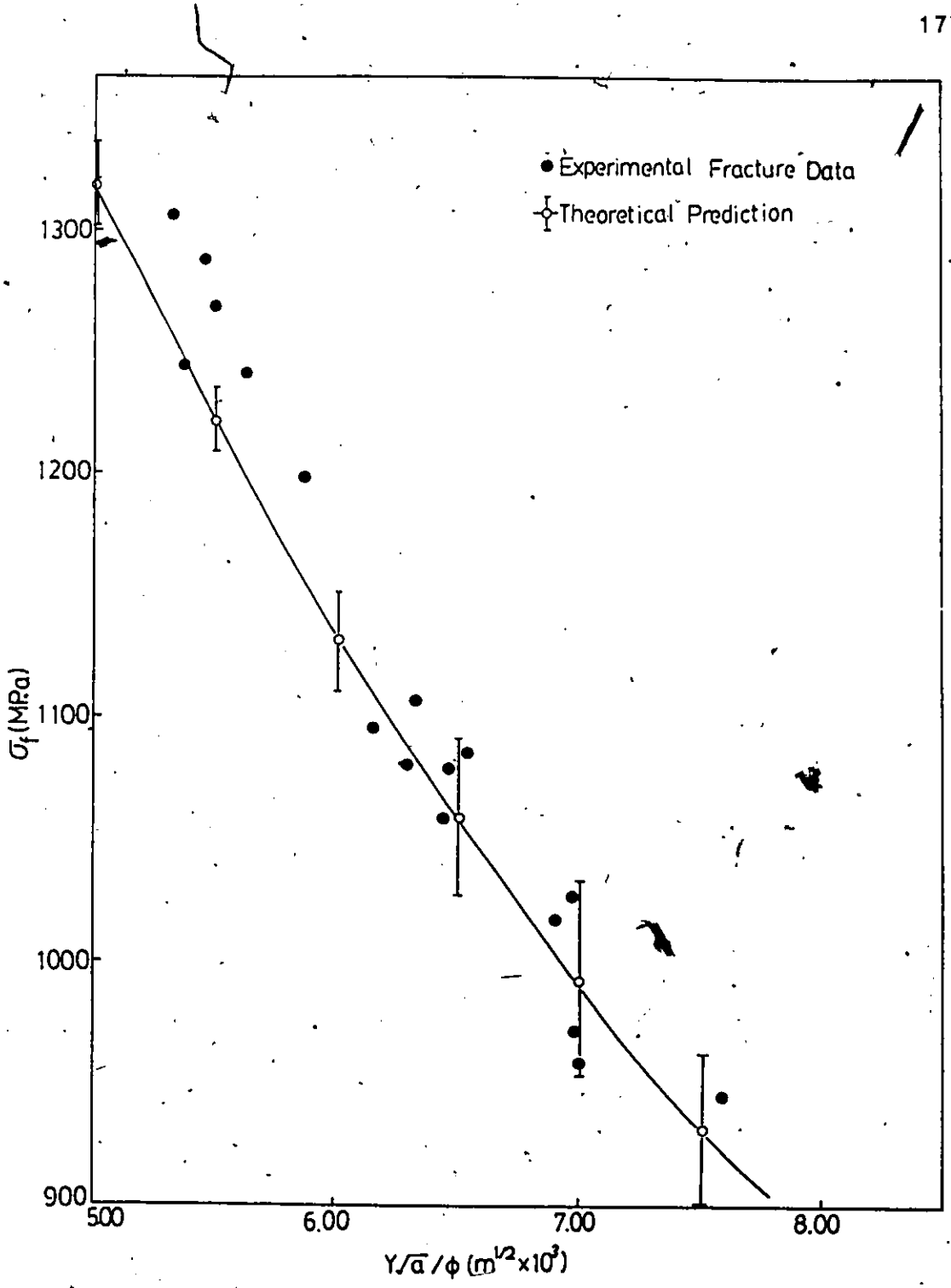

Fig. 8.4 Theoretical prediction v.s. actual fracture stress for an alumina fracture origin in a tetragonal zirconia ceramic.

An important implication of the present analysis is the prediction of the fracture stress of ceramics containing known defects. If the near-surface defects in a ceramic are detected by NDE with respect to their size, shape, depth and type, the fracture strength associated with the most critical detected can be calculated. The present analysis only applies to the particular defect/matrix system wherein $\alpha_i < \alpha_m$, $K_{ci} < K_{cm}$ and $E_i > E_m$. For other types of inclusion and defect, a similar analysis can be performed.

8.6 Conclusions

The results presented in this chapter lead to the following conclusions :

(1) Combination of the weight function method and the part-through elliptical crack extension model results in a pedagogy for analyzing the fracture behavior of ($\alpha_i < \alpha_m$, $K_{ci} < K_{cm}$, $E_i > E_m$) inclusion/matrix systems.

(2) The residual stresses developed around inclusions due to thermal contraction mismatch and subsequent elastic mismatch stresses during loading have a significant effect on the strength of the ceramic matrix.

(3) T_g and strength predictions for an α-Al_2O_3/t-ZrO_2 inclusion/matrix system based on the analysis agree well with experimental data.

CHAPTER 9

An Agglomerate-Initiated Fracture Model for Ceramics

9.1 Introduction

In Chapter 4, it was shown that an agglomerate defect initiates fracture differently from a pore defect of the same equivalent dimension and the increased severity is suggested to be related to local residual stresses developed around the defect. The existence of residual stresses was experimentally demonstrated in Chapter 5. It was proposed (Ch. 2.3.1) that differential sintering occurs and a tensile stress develops for the higher-green-density agglomerate during sintering. This qualitatively explains the observed circumferential cavity and the central larger-grained region associated with an agglomerate fracture origin (Ch 3.3.1). To understand the agglomerate-initiated fracture process, its behaviour during sintering must be examined (Ch. 5.4). An agglomerate-initiated fracture model is now constructed by examining the sintering process and suggesting a residual stress retention mechanism. The results are compared with experimental data.

9.2 An Agglomerate Sintering Model

It is suggested that lower-green-density powder

agglomerates will not survive processing and the higher-green-density powder agglomerates are more likely to be the source of the final defects (Ch. 2.1.2; 2.3.1; 4.3). Also the denser agglomerates will start and finish sintering earlier than the matrix (Ch 2.3.1). It is expected a sintering-rate transition will exist for agglomerates and their matrix. Initially a higher-green-density agglomerate will sinter faster than its matrix and a radial tensile stress will develop. This will lead to decohesion as the local stress exceeds the interfacial bond strength. This is expected to happen before the sintering-rate transition point. Thereafter, the lower-green-density matrix will sinter faster than the agglomerate giving continuous shrinkage until maximum density is reached. This model is schematically illustrated in Fig. 9.1. The sintering process for the agglomerates and matrix are expressed in this figure in terms of the % theoretical sintered density (ρ_t) and plotted v.s. temperature. The green density of the agglomerate is assumed 60% ρ_t and that of the matrix 50% ρ_t. These are considered reasonable values. According to this model, the point of equivalent-sintering-rate should occur during the final sintering stage of the agglomerate and the initial sintering stage of the matrix. The corresponding heat-up (temperature increase) curve is also shown in the figure. Four regions appear on the diagram, i.e. (1) the zero-sintering region (2) the region wherein the agglomerate

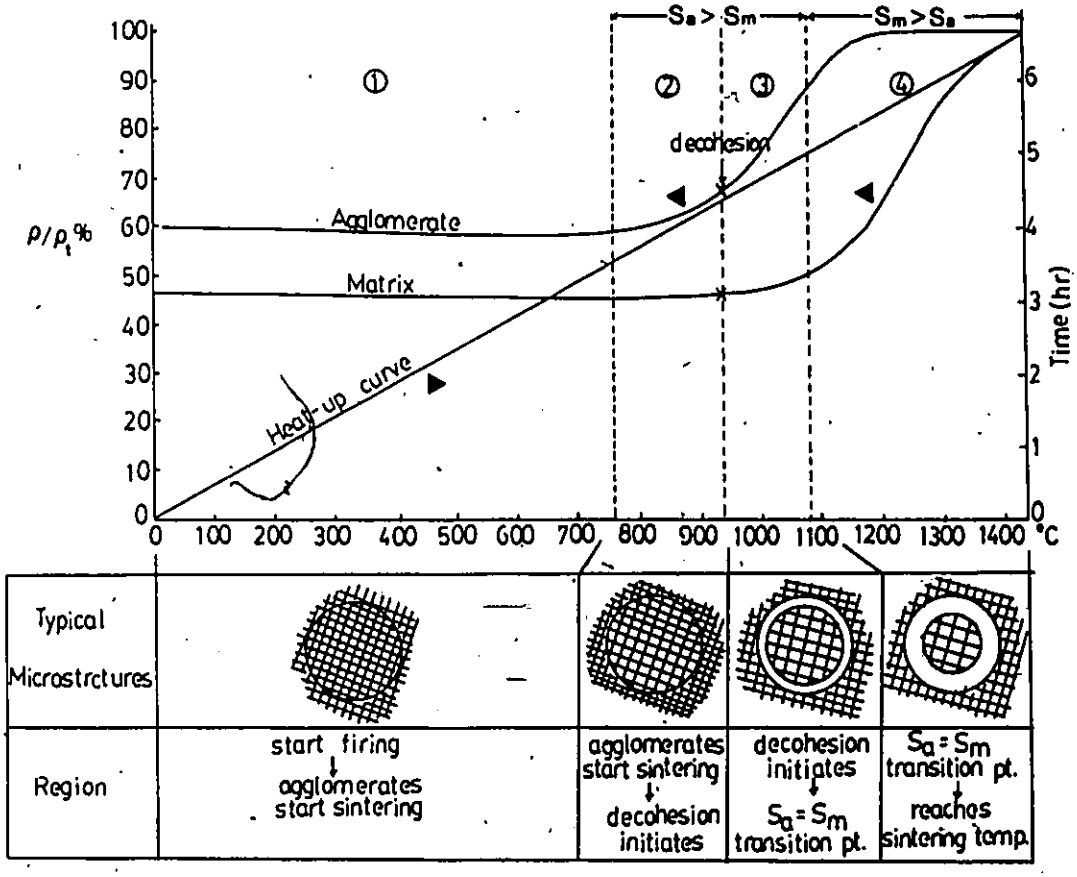

Fig. 9.1 An agglomerate sintering model.

sintering rate (S_a) > matrix sintering rate (S_m) - before decohesion, (3) the same after decohesion and (4), the $S_a < S_m$ region. The corresponding schematic microstructures developed in each region are also shown. The agglomerate sinters earlier so its grains will be larger. The larger starting agglomerate will sinter faster and leave a larger circumferential cavity. These predictions are consistent with present experimental observation (Ch 3.3.1).

9.3 A Residual-Stress Retention Model

The development of residual strain associated with an agglomerate due to differential sintering ($\Delta\varepsilon_d$) has been treated (Ch. 2.3.1) and the result is given in Eq. (2.14). For a spherical agglomerate of radius R embedded in the matrix, an elastic hydrostatic tension, σ_d, can exist exclusively inside the agglomerate with the magnitude (from Eq. (2.14) and (2.15)) ;

$$\sigma_d = - \frac{1}{1/4G_m + 1/3K_a} [(\rho_{0a}/\rho_a)^{1/3} - (\rho_{0m}/\rho_m)^{1/3}] \qquad (9.1)$$

where G_m is the shear modulus of matrix and K_a the bulk modulus of agglomerate, which are the function of the density of the corresponding materials [Coble, 1956; Kingery, 1976b]. Eq. (9.1) will be used later to demonstrate the magnitude of stress if the agglomerate and the matrix

both respond elastically during sintering. In general, the viscoelastic stress has to be considered (Ch. 2.3.1) and σ_d is acquired from Eq. (2.16). The components of residual stresses in the radial (σ_r) and tangential directions (σ_t) in a matrix a distance r from the centre of agglomerate are;

$$\sigma_r = \sigma_d \, (R/r)^3 \qquad (9.2a)$$

$$\sigma_t = -1/2 \, \sigma_d \, (R/r)^3 \qquad (9.2b)$$

At the agglomerate/matrix interface $\sigma_r^m = -2\sigma_t^m = \sigma_d$, where the superscripts denote the maximum magnitude. σ_r^m will be responsible for the formation of circumferential cavity.

Decohesion criterion for an agglomerate due to differential sintering can be derived based on the results of Ito (1981). Ito studied the interfacial cracking associated with an inclusion due to thermal contraction mismatch with its matrix. The strain energy release rate (G) for a preexisting crack of normalized length μ at the interface of a spherical inclusion of radius R is given by :

$$G = 0.56 \, \Delta\varepsilon \, \bar{\sigma} \, R \, \sin\mu \, [2 - \sin\mu] \qquad (9.3)$$

where $\Delta\varepsilon = \Delta\alpha \cdot \Delta T$ is the thermal strain and $\bar{\sigma}$ is the corresponding thermal stress (Ch. 2.3.1). This result can be applied to the differential sintering associated with an agglomerate, i.e. substituting $\Delta\varepsilon_d$ (Eq. (2.14)) and σ_d (Eq. (9.1)) for $\Delta\varepsilon$ and $\bar{\sigma}$ in the above equation respectively

and replacing K for G, obtain ;

$$K^2 = 0.56\ \sigma_d^{\ 2}\ R\ \sin\mu\ [2 - \sin\mu]\ E_{ma}(1 - \nu^2)(1/4G_m + 1/3K_a) \qquad (9.4)$$

where E_{ma} is the Young's modulus estimated at agglomerate/ matrix interface. Crack extension at the interface will occur when K in Eq. (9.4) reaches K_{Ic} associated with the interface and σ_d becomes the fracture stress (σ_{df}) at the interface.

The retention of residual stresses for agglomerate defects following formation of the circumferential cavity and sintering is considered due to the concurrent shrinkage of the matrix during sintering. During the initial residual-stress build-up stage, the matrix grains near the interface are strained along the stress direction. Suppose the matrix is fully "sintered" and responds linear elastically (i.e. an imaginary condition of unsintered agglomerates in a fully sintered matrix) then the interfacial stressed matrix grains will resume their original shape on decohesion and no residual stress is retained. However, for a "sintering" matrix (i.e. both agglomerates and matrix are sintering but at different rates), at the moment of decohesion it is possible that the global matrix has shrunk to an extent that precludes complete elastic recovery of the interfacial stressed matrix grains, "locking-in" levels of residual stress. Although subsequent sintering favors the relaxation

of these locked-in residual stresses by viscous flow processes (Ch. 2.3.1), the continued shrinkage of the global matrix may still prevent complete relaxation and residual stresses are retained. This process is schematically shown in Fig. 9.2. where an interfacial hexagonal-shaped matrix grain is simultaneously strained by differential-sintering and global-sintering stresses. It is expected that appreciable stress relaxation via viscous flow may occur during the later stages of sintering when matrix shrinkage has ceased. This is often avoided to control undesirable grain growth so leaving retained residual stresses. Another possible source of residual-stress retention involves the partial decohesion of the agglomerate/matrix interface. As shown in Fig. 3.9, the intact portion of the interface may preclude total elastic recovery at decohesion and a level of locked-in residual stress could be retained.

9.4 Estimation of the Retained Residual Stresses

Exact calculation of the retained residual stresses from the above models requires knowledge of the relaxation processes involved in elastic and thermal recovery. This is complicated by the influence of varied sintering conditions (i.e. heating rate, sintering temperature and period). No detailed analysis of this complex process is attempted, rather an order-of-magnitude estimation is made to investigate the validity of the proposed model.

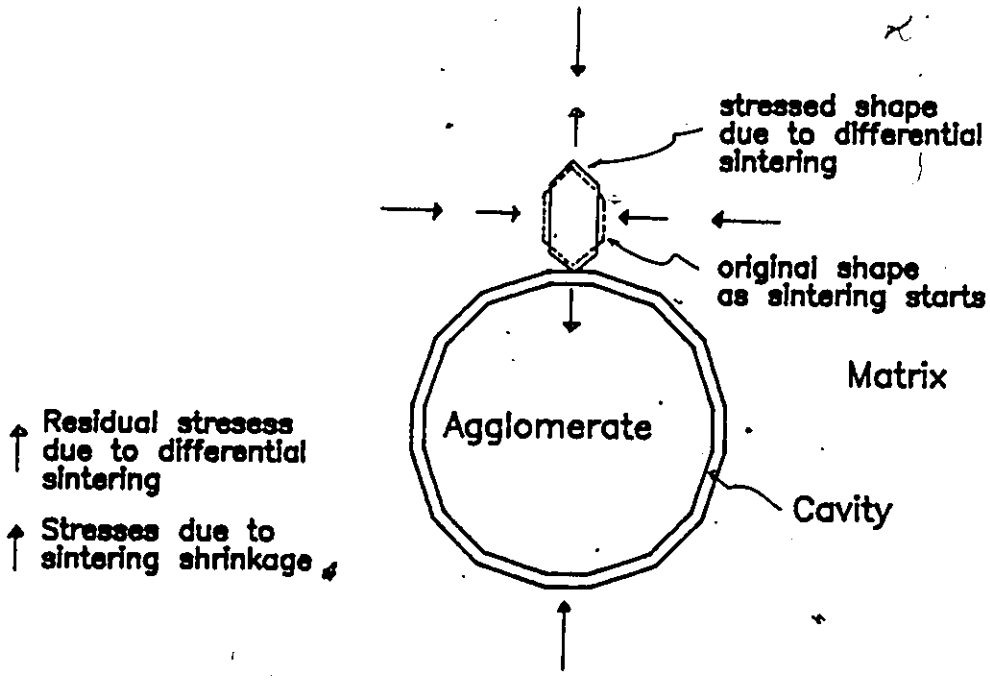

Fig. 9.2 Residual stress states due to differential sintering and sintering shrinkage for a hexagonal-shaped matrix grain around an agglomerate defect.

The exclusively elastic stress (Eq. (9.1)) is first examined. If the agglomerate/matrix interface remains coherent in the sintering region $S_a > S_m$ (Fig. 9.1), the magnitude of residual stress at $S_a = S_m$ can be estimated from Eq. (9.1). Choosing the most probable parameter ranges : ρ_{0a}= 0.6 to 0.7, ρ_{0m}= 0.45 to 0.5, ρ_a= 0.9 to 1.0 and ρ_m= 0.5 to 0.7; and , G_m= 0.4G, K_a=0.6K and E = 220 GPa, σ_d is in a range of 1 to 5 GPa. This is even greater than the matrix strength after sintering, therefore viscous relaxation in this stage must be considered. Although the viscoelastic stress may be calculated from the model prediction (Eq. (2.16)), the more relevant fracture stress at agglomerate/matrix interface can be directly estimated from Eq. (9.4). The corresponding interface fracture-toughness at decohesion is expected to be very low since decohesion occurs at the early stage of sintering. This will be close to the fracture toughness of a green compact and is estimated as 0.15 to 0.35 MPa·$m^{1/2}$ for t-ZrO_2 [Bradt, 1988]. The critical interfacial flaw size is assumed as 0.1πR following the results of Ito [1981]. For an agglomerate of R = 10 μm, the interface fracture stress at decohesion, σ_{df}, is in the range of 600 to 1300 MPa. The final retained residual stress is the fraction of σ_{df} left after the elastic and viscous recovery. This can be indirectly estimated from the results of previous Chapters (5 and 8). From Eq. (5.3), the defect severity parameter is : X

$= 1 + (\sigma_e/\sigma_f)$. The residual stress term, σ_e, for an agglomerate can be rewritten from Eq. (8.14) as ;

$$\frac{1.5\Phi\ \sigma_{df} T}{Y^2(1-\nu^2)} \left(= \sigma_e \right) \qquad (9.5)$$

where T is a residual stress relief function associated with the elastic and thermal recovery. For an agglomerate X = 1.30 (Ch. 5.4) with R = 10 μm, and σ_f= 900 MPa (Ch. 3.3.2), σ_e estimated as 300 MPa, giving $\sigma_{df}T \simeq 410$ MPa. Comparing this result with the corresponding magnitude of σ_{df} (600 to 1300 MPa), a value of T between 0.30 and 0.65 is obtained. This is smaller than the magnitude of S associated with the inclusions and is considered reasonable, because T includes more-severe interfacial cracking and viscous recovery while the S only involves radial microcracking.

The complexity of the processes only permit models to be proposed and order-of-magnitude fracture data determined. More work is needed to clarify the agglomerate behavior during sintering and decohesion with emphasis on the relaxation process at and after cavity formation.

9.5 Summary

The present study is summarized as follows :

(1) An agglomerate sintering model and relevant residual stress retention model are proposed to describe the fracture behavior of an agglomerate defect.

(2) The estimated fracture data are reasonable compared with the experimental results.

(3) Detailed analysis and experiments pertaining to the residual-stress relaxation process should be conducted.

CHAPTER 10

Conclusions and Future Work

The present document reports research on the defect-initiated fracture in and strength improvement of zirconia ceramics and the following conclusions result ;

1. The flexural strength of linear elastic ceramic materials can be greatly improved by flaw elimination from the precursor powders. A 4.5 wt% Y-PSZ was used as the model system to demonstrate the potential improvement. Fracture-initiating defects of larger-size or higher-density than the host fine powders, i.e. agglomerates, iron inclusions etc. can be eliminated by a colloid-dispersion/sedimentation procedure. Organic inclusions in the powder can be eliminated by a burnout/re-isopressing procedure. The size of the pore defects is also reduced by these procedures. Lower-density inclusion defects, eg. alumina in Y-PSZ powders, are unaffected by this secondary powder processing.

2. To explain the non-equivalence vis-á-vis strength of the equivalent-dimensioned defects of different types a residual stress model is proposed. Local residual stresses develop around defects in ceramics due to thermal-, elastic-mismatch or differential sintering. These results explain the relationship between the severity of different defect

types and the ceramic strength modification. Tensile residual stresses are proposed associated with fiber inclusions and agglomerates in Y-PSZ and these two defect types are more severe than an equi-dimension pore defect. No residual stresses are expected with pores or iron inclusions and the corresponding ceramic strengths are predicted by the crack model. It is suggested that compressive residual stresses develop around alumina inclusions and these are therefore less severe than the equivalent-dimensioned pores. The observed relative severity of the defect types was quantitatively ranked and a "relative defect severity parameter" (X) defined to correct the crack model.

3. The existence of residual stress associated with the defect types was experimentally verified and the stress-relaxation-temperature (T_g) was determined for Y-PSZ (1135°C). It was shown that, below T_g, a temperature-dependent residual stress is associated with α-Al_2O_3 defects in Y-PSZ and a temperature-independent residual stress is associated with agglomerate defects. Pore defects are residual-stress free. The severity of agglomerate defects could be decreased by appropriate heat treatment procedure (1250°C x 3 hrs).

4. The size equivalence of a defect and its associated flaw size was verified for the alumina inclusion in Y-PSZ. It was found that the alumina inclusions fracture prior to global fracture of Y-PSZ and no radial cracking is

associated with the inclusions.

5. An in-test subcritical precracking procedure was developed for the valid determination of K_{Ic} using chevron-notched-bend bar. This technique uses two-step control of the testing machine crosshead speed to facilitate precracking and maintain the necessary stable crack growth. The technique was applied to 4.5 wt% Y-PSZ and was shown to be a simple and reliable testing method.

6. Inclusion- and agglomerate- initiated-fracture mechanisms were modeled. In the former, a weight-function method was used to compute the residual stress intensity factor. The results were used to compute T_g for Y-PSZ and to make strength predictions for the α-Al_2O_3/t-ZrO_2 system. The agreement with experiment in both cases was good. In the latter, an agglomerate sintering model and residual stress retention model were proposed and fracture data was estimated. The results agreed with experimental data.

Some work is suggested to do in the future, these include ;

(1) development of a powder processing procedure to remove those solid inclusions with lower density than the fine powder.

(2) combination with other fabrication procedures to eliminate the pores and improve the Weibull modulus.

(3) investigation of the sintering behaviour of the

higher-green-density powder agglomerates, the residual stresses associated with the agglomerate defects and refinement of the agglomerate-initiated fracture model.

APPENDIX A

The Part-Through Elliptical Crack Extension Model

Assume the crack lies in the X,Z-plane with its major dimension 2c along the Z-axis and its minor dimension 2*a* along the X-axis. Then the crack opening displacement, μ, in the Y-direction (tensile direction) is expressed as ;

$$\mu = \mu_0 \left(1 - \frac{x^2}{a^2} - \frac{z^2}{c^2}\right)^{1/2} \qquad (A.1)$$

where μ_0 is half the maximum total crack opening displacement at the crack center. The variation of μ at a fixed distance r from the crack border can be expressed by inserting $x = a \sin\theta$ and $z = c \cos\theta$ into (A.1), as ;

$$\mu^2 = \mu_0^2 \frac{2r}{ac} \left(a^2\cos\theta^2 + c^2\sin\theta^2\right) \qquad (A.2)$$

μ is further related to the stress intensity factor, K, as ;

$$\mu = \frac{2(1 - \nu^2)}{E} (2r)^{1/2} K \qquad (A.3)$$

and also from LEFM ;

$$G = \frac{\pi}{E} (1 - \nu^2) K^2 \qquad (A.4)$$

Inserting μ^2 from (A.2) into (A.3), gives ;

$$K^2 = \frac{1}{4}\left(\frac{E}{1-\nu^2}\right)\left(\frac{\mu_0^2}{ac}\right)(a^2\cos^2\theta + c^2\sin^2\theta)^{1/2} \qquad (A.5)$$

and then ;

$$G = \frac{\pi}{4}\left(\frac{E}{1-\nu^2}\right)\left(\frac{\mu_0^2}{ac}\right)(a^2\cos^2\theta + c^2\sin^2\theta)^{1/2} \qquad (A.6)$$

μ_0 can be evaluated from the strain energy change at small outward displacement, which gives ;

$$\mu_0 = \frac{2(1-\nu^2)\sigma a}{E\Phi} \qquad (A.7)$$

Inserting (A.7) into (A.5) and (A.6) and consider the free surface effect, then ;

$$K_I^2 = GE = \frac{Y^2\sigma^2(1-\nu^2)}{\Phi^2}\left(\frac{a}{c}\right)(a^2\cos^2\theta + c^2\sin^2\theta)^{1/2} \qquad (A.8)$$

where Y is a geometrical factor.

APPENDIX B

Fluid Mechanical Aspects of Sedimentation

B.1 Laminar Flow Condition

Stokes' law describes the terminal velocity, V_t, of a spherical solid particle settling in an infinitely-dilute suspension under laminar flow condition as ;

$$V_t = \frac{2\,R^2(\rho_s - \rho_l)\,g}{9\,\eta} \qquad (2.11)$$

The laminar flow condition has been experimentally established [Geiger, 1973] and is expressed via the Reynolds number, Re. It has been shown that Stokes' law is valid up to $Re \simeq 1.0$ for a spherical particle. In practice, since $Re = 2RV_t\rho_l/\eta$, the limiting laminar flow condition sets a maximum sphere radius, R_{max}, in a specific fluid system beyond which Stokes' law no longer applies, i.e. by substituting Eq. (2.11) into the Re equation ;

$$R_{max} = \left(\frac{9\,Re_{(laminar)}\,\eta^2}{4\,\rho_l(\rho_s - \rho_l)\,g} \right)^{1/3} \qquad (B.1)$$

The non-sphericity and non-infinite-dilution for valid application of Stokes' law are now discussed.

B.2 Non-Sphericity Effect

An "equivalent settling velocity diameter" (D_{vel}) was introduced to deal with the non-spherical particles in settling [Woods, 1988a]. D_{vel} is defined as the diameter of an imaginary sphere which has the same terminal settling velocity as the specific particle, i.e. from Eq. (2.11) ;

$$D_{vel} = \left(\frac{18 \eta V_t}{(\rho_s - \rho_l) g} \right)^{1/2} \qquad (B.2)$$

Fixed relations between D_{vel} and the optically-determined particle dimensions exist. One of such dimension relevant to the present study is D_m, which is defined as the diameter of a standard circle with the nearest-equal-area to the microscopic image of the particle [Woods, 1988a] and ;

$$\frac{D_{vel}}{D_m} = \frac{\sqrt{\alpha_v}}{0.72} \qquad (B.3)$$

where α_v is a "volume shape factor", i.e. a proportional constant between the particle volume (V_p) and D_m such $\alpha_v = V_p/D_m^3$. Values of α_v for various particle geometries and some common minerals are listed in Table B.1.

Table B.1 Volume shape factor (α_v) for various geometries and minerals

geometry	α_v	mineral
cube	0.7	-
sphere	0.52	-
rod	0.23	coal (0.227)
-	-	limestone (0.164)
-	-	gypsum (0.128)
plate	0.03	mica (0.03)

From Eq. (B.3), for most encountered particles with α_v = 0.02 to 0.5, $D_m > D_{vel}$. That means the "actual" settling velocity based on D_{vel} (V_{ta}) is smaller than the "expected" settling velocity based on D_m (V_{te}), i.e., from Eqs. (B.2) and (B.3);

$$\frac{V_{ta}}{V_{te}} = \frac{D_{vel}^2}{D_m^2} = 1.93\ \alpha_v \qquad (B.4)$$

B.3 Hydrodynamic Effect

The non-infinite-dilution of colloid suspension promotes particle-particle interaction. Correction for the application of Stokes' law is necessary due to the induced hydrodynamic effect and electrostatic effect.

Hydrodynamic effect is a consequence of backflow which occurs when a particle falling through a fluid drags

some fluid along with it. In a bounded system this down flow of particles plus fluid must be compensated for by a reverse flow of fluid elsewhere in the system, as illustrated in Fig. B.1 [Reed, 1976]. In a dilute system where particles are set apart far enough, the overall effect of backflow for a particle is expected a decrease in settling velocity compared with that predicted by Stokes' law. Correction for the terminal settling velocity due to hydrodynamic effect has been extensively studied [Batchelor, 1972; Oliver, 1961; Reed, 1976; Richardson, 1954]. Batchelor's results [1972] are most often used, which applies to a sphere settling in a dilute suspension of concentration (C) ≤ 0.02, i.e.;

$$V_{ts} = V_{to} (1 - KC) \qquad (B.5)$$

where K is a constant and equal to 6.55 for identical random hard spheres.

B.4 Electrostatic Effect

Theoretical studies [Booth, 1954; Dickinson, 1980] on the electrostatic effect concluded that the interaction between the charges on the particles modifies the fluid field and alters the settling velocity of the particles. Dickinson [1980] related the constant K (Eq. (B.5)) to the interparticle spacing which will be modified if surface charges exist. This gives;

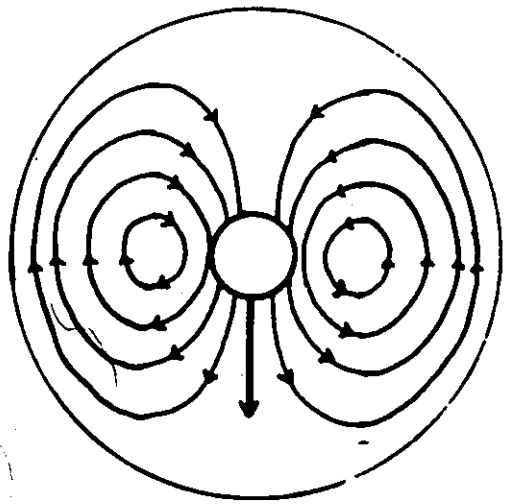

Fig. B.1 Fluid streamlines for particles motion in a bounded system.

$$K \simeq 1.5\ \rho_0^{\ 2} + 3.75\ \rho_0^{\ -1} - 1.32 \qquad (B.6)$$

where $\rho_0 = 2r/(a_1 + a_2)$, r is the spacing between two particles with radius a_1 and a_2 respectively. In most cases, it was shown that $2 \leq \rho_0 \leq 2.6$ corresponding a decrease in settling velocity of 0 to 9 %.

The physical explanation for the reduction in settling velocity due to electrostatic effect lies on the fact that the pairs of interaction particles are not allowed to approach closely because of the electrostatic repulsion. They are more influenced by the diffuse upward flow and therefore settle slower.

B.5 Combined Effect

Combined effect of non-sphericity, hydrodynamics and electrostatics can be incorporated into a correction factor, F, in Stokes' law, such ;

$$V_t = F\ \frac{2\ R^2(\rho_s - \rho_l)\ g}{9\ \eta} \qquad (B.7)$$

From Eqs. (B.4), (B.5) and (B.6), F can be written as;

$$F = (1.93\ \alpha_v)\cdot(1 - 6.55C)\cdot(2.32 - 1.5\ \rho_0^2 - 3.75\ \rho_0^{-1}) \qquad (B.8)$$

APPENDIX C

Comparison of the Sedimentation Behavior in 2-Propanol, Methanol and Water

As stated in Appendix B.1, the laminar flow condition sets a maximum equivalent sphere radius in a specific suspension system beyond which Stoke's law is no longer applicable. The calculation are performed for these three liquid media and the results are plotted as sphere radius v.s. Reynolds number in Fig. C.1. It is shown for Re = 1, the corresponding maximum sphere radius is 76.6 μm for 2-propanol, 35.6 μm for water and 26.9 μm for methanol. These radius set the upper limits for the valid application of Stoke's law. It is noted that 2-propanol appears to be more suitable for the situation where the target size eliminated is large.

The settling velocity for the particles of specific size is determined by the density and viscosity of the dispersants. This also has some influence on the sedimentation procedure since too fast or too slow settling is unpractical. The settling velocity of the spherical Y-PSZ with radius from 0.1 to 100 μm for the three dispersants are shown in Fig. C.2. The time scale shown is the time required for travelling 10 cm distance. It is noted that the settling

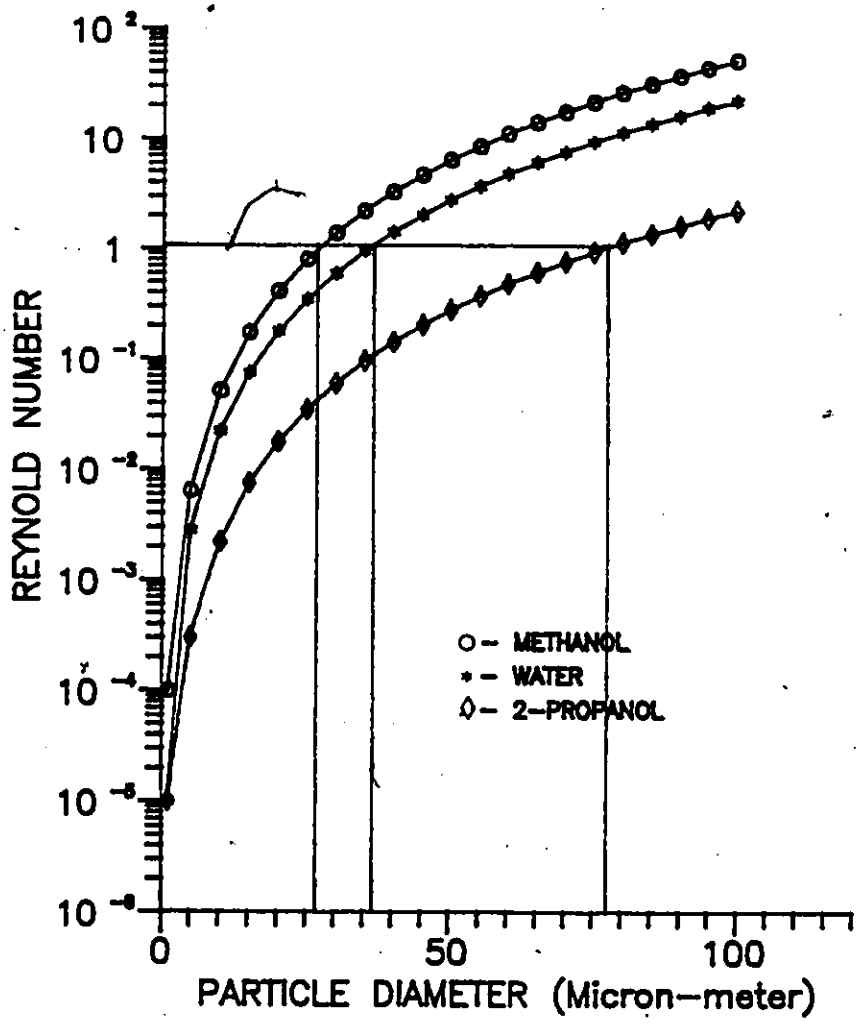

Fig. C.1 Settling of the Y-PSZ spheres in various dispersants.

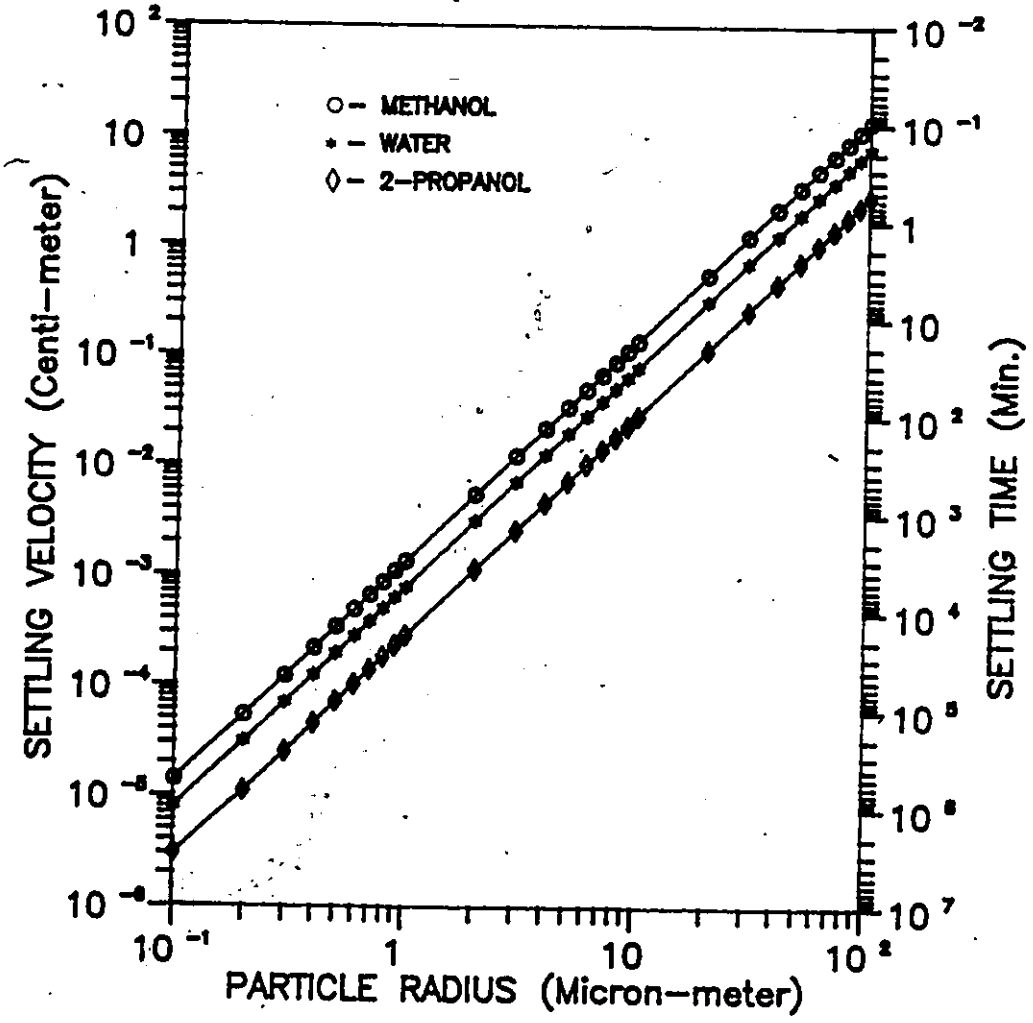

Fig. C.2 Settling velocity of Y-PSZ spheres in various dispersants.

velocity of Y-PSZ particles in methanol is almost double that in water and five-time faster than in 2-propanol.

APPENDIX D

The Weight Function for a Through-Thickness and a Part-Through-Thickness Elliptical Crack

The stress intensity factor for a given 2-dimensional crack geometry under an arbitrary loading is given by [Rice, 1972] ;

$$K_I = \int_\Gamma t \cdot h \, d\Gamma + \int_A f \cdot h \, dA \qquad (D.1)$$

where t is the stress vector acting on boundary Γ chosen around the crack tip and f is the body force acting in region A defined by Γ. h is a universal weight function determined from a known loading system (as Eq. 2.18).

For a through-thickness crack of length *a* extending along the x-axis, displaced along the y-axis by a symmetric pressure $\sigma_*(x)$ perpendicular to the crack surface (if the boundary Γ consists of the crack surfaces and no body force exists in area A), Eq. (D.1) can be written (realizing Γ is equal to twice of the crack length *a*) ;

$$K_I^{(2)} = \int_\Gamma \sigma_*(x) \left[\frac{H}{2K_I^{(1)}} \frac{\partial \mu(x,a)}{\partial a} \right] d\Gamma$$

$$= 2\cdot\int_0^a \sigma_s(x)\left[\frac{H}{2K_I^{(1)}}\frac{\partial\mu(x,a)}{\partial a}\right]dx$$

$$= \frac{H}{K_I^{(1)}}\int_0^a \sigma_s(x)\frac{\partial\mu(x,a)}{\partial a}\,dx \qquad (D.2)$$

Eq. (D.2) has been widely used in previous studies (Ch. 2.3.2).

The analog for 3-dimensional crack geometry is ;

$$K_I = \int_S t\cdot h\,dS + \int_V f\cdot h\,dV \qquad (D.3)$$

where S is the surface chosen around the crack tip and V the volume defined by S.

For a part-through-thickness elliptical crack with semi-axis a along the x-axis, $(-a \le x \le a)$, another semi-axis c along the y-axis $(-c \le y \le c)$, displacement along the z-axis and a symmetric pressure $\sigma_s(x,y)$ perpendicular to the crack surface, Eq. (D.3) can be written (for a surface section element along the x-axis, $d\Gamma_x$ and along the y-axis, $d\Gamma_y$, $dS = d\Gamma_x \times d\Gamma_y$) ;

$$K_I^{(2)} = \int_S \sigma_s(x,y)\left[\frac{H}{2K_I^{(1)}}\frac{\partial\mu(x,y,a,c)}{\partial A}\right]dS$$

$$= \frac{H}{2K_I^{(1)}}\int_{\Gamma_x}\int_{\Gamma_y}\left[\sigma_s(x,y)\frac{\partial\mu(x,y,a,c)}{\partial A}\right]d\Gamma_x d\Gamma_y \qquad (D.4)$$

A general expression for $K_I^{(2)}$ has been given in Bueckner's study [1977], however the special case of the stress intensity factor for the crack front along a semi-axis (eg. the x-axis) can be computed. Realizing dA is $\pi c da$, $\Gamma_x = 4a\sqrt{1-(y^2/c^2)}$ and $\Gamma_y = 4c$, Eq. (D.4) can be rewritten as ;

$$K_I^{(2)} = \frac{H}{2K_I^{(1)}}\left[4\int_{y=0}^{c}\left(4\int_{x=0}^{a\sqrt{1-(y^2/c^2)}}\sigma_s(x,y)\,\frac{\partial\mu(x,y,a,c)}{(\pi c)\partial a}\,dx\right)dy\right]$$

$$= \frac{H}{K_I^{(1)}}\,\frac{8}{\pi c}\int_{y=0}^{c}\int_{x=0}^{a\sqrt{1-(y^2/c^2)}}\sigma_s(x,y)\,\frac{\partial\mu(x,y,a,c)}{\partial a}\,dx\,dy \qquad (D.5)$$

Similar expressions to Eq. (D.5) can be found in previous studies [Besuner, 1974, Mattheck, 1983] wherein the average stress intensity factors were used. In the present analysis, the stress intensity factors at the end of semi-axes of an elliptical crack are involved.

APPENDIX E

Solution for the Maximum Residual Stress Intensity Factor

Eq. (8.8) can be simplified to ;

$$K_{Ir}^{m} = \frac{-3.24\ \Phi\sigma_T S}{Y\sqrt{1-\nu^2}\sqrt{R}} \int_{y=0}^{R} \Big[(2.24\ R^{-8/3} y^{4/3} - 1.5\ R^{-4/3}) \cdot \int_{x=0}^{R} (R^2 - x^2 - y^2)\, dx + (-1.5\ R^{-4/3} y^{4/3} + 1) \cdot \int_{x=0}^{R} (R^2 - x^2 - y^2)^{-1/2} dx \Big]\, dy \qquad (E.1)$$

and these integrals can be reduced by using the formula [Beyer, 1987] ;

$$\int_0^a x^m (a^2 - x^2)^{n/2}\, dx = \frac{1}{2}\, a^{m+h+1} \frac{\Gamma\left(\frac{m+1}{2}\right)\ \Gamma\left(\frac{n+2}{2}\right)}{\Gamma\left(\frac{m+n+3}{2}\right)} \qquad (E.2)$$

where Γ is a gamma function. On substitution, the following equation results ;.

$$K_{Ir}^{m} = \frac{3.24\ \Phi\sigma_T S}{Y\sqrt{1-\nu^2}\sqrt{R}} (0.27\ R - 0.56\ R).$$

$$= \frac{-0.95\ \Phi\sigma_T S\sqrt{R}}{Y\sqrt{1-\nu^2}} \qquad (E.3)$$

Since $\Phi = 1.57$ for a spherical shape. then ;

$$K_{Ir}^{m} = \frac{-1.5\ \sigma_T S}{Y\sqrt{1-\nu^2}}\sqrt{R} \qquad (8.9)$$

APPENDIX F

Evaluation of the Residual Stress Relief Function S

The following analysis is based on global crack surface energy equivalence between a annular crack and many small radial microcracks around an inclusion. Consider a spherical inclusion of radius R around which there exists an annular (radial) crack of normalized crack length ω (ω = c/R) (Fig. F.1). The total strain energy, U_0, of the uncracked system with hydrostatic residual stress σ_T is given by [Davidge, 1968] ;

$$U_0 = 2 \pi \beta \sigma_T^2 R^3 \qquad (F.1)$$

where $\beta = [(1 + \nu_m)/2E_m] + [(1 - 2\nu_i)/E_i]$. The strain energy U of the cracked system is then ;

$$U = U_0 f(\omega) = 2 \pi \beta \sigma_T^2 f(\omega) R^3 \qquad (F.2)$$

where $f(\omega)$ is a residual strain energy relief function [Ito, 1980]. If σ_T' is the remaining residual stress in the cracked system such that $\sigma_T' = \sigma_T S(\omega)$, ($S(\omega)$ is a residual stress relief function already defined), then ;

$$\begin{aligned} U &= 2 \pi \beta \sigma_T'^2 R^3 \\ &= 2 \pi \beta \sigma_T^2 S(\omega)^2 R^3 \end{aligned} \qquad (F.3)$$

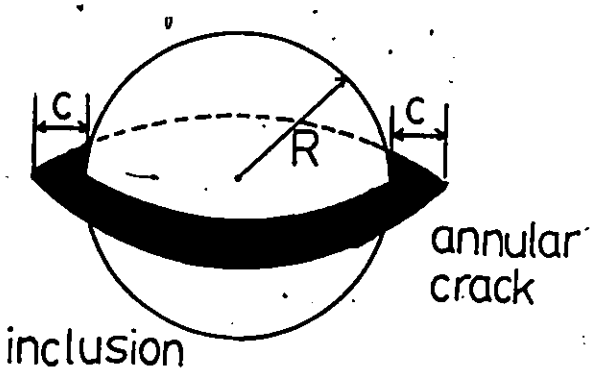

Fig. F.1 A spherical inclusion with an annular crack of the normalized size $\omega = c/R$

or

$$S(\omega) = \sqrt{f(\omega)}$$

The strain energy release rate (G) for crack extension is ;

$$G = \frac{dU}{dA} = U_0 \frac{df(\omega)}{dA} \qquad (F.4)$$

for small ω. the area (A) of the annular crack is ;

$$A = 2\pi Rc \simeq 2\pi \omega R^2 \qquad (F.5)$$

Substituting (F.1) and (F.5) into (F.4) gives ;

$$G = R \beta \sigma_T^2 \frac{df(\omega)}{d\omega} \qquad (F.6)$$

At $R \geq R_c^{min}$, crack initiation occurs and $G = G_c$, so ;

$$G_c = R \beta \sigma_T^2 \frac{df(\omega)}{d\omega} \quad , \text{for } R \geq R_c^{min} \qquad (F.7)$$

Rearranging and integration, gives ;

$$f(\omega) = (G_c \omega / R \beta \sigma_T^2) + C \qquad (F.8)$$

where C is an integration constant. Substituting (F.8) into (F.3) results in ;

$$S(\omega) = \sqrt{f(\omega)} = \sqrt{(G_c \omega / R \beta \sigma_T^2) + C} \qquad (F.9)$$

Because $S(\omega)$ must satisfy Eq. (8.9) and bears the form of $K/\sqrt{R}$ (where K is a constant), the integration constant, C = 0, and ;

$$S(\omega) = [G_c^{\prime}\omega \;/\; R\,\beta\,\sigma_T^2\,]^{1/2}$$

$$= [K_c^2\,\omega \;/\; E\,\beta\,(1-\nu^2)\,\sigma_T^2\,]^{1/2}\,(1\;/\;\sqrt{R}\,) \qquad (F.10)$$

For $R \le R_c^{min}$, the crack does not extend and $S(\omega) = 1$.

REFERENCES

Bansal, G.K. (1976). *J. Am. Ceram. Soc.*, 59, 87-88.

Batchelor, G.K. (1972). *J. Fluid. Mech.*, 52, 245-268.

Batdorf, S.B. (1978). In R.C. Bradt (Ed.), *Fracture Mechanics of Ceramics*, Vol. 3, Plenum Press, pp. 1-30.

Baumard, J.F. and P. Abelard (1984). In N. Claussen, *Science and Technology of Zirconia II*, American Ceramic Society, pp. 555-571.

Barringer, E.A. and H.K. Bowen (1984). *Ceram. Eng. and Sci. Proc.*, 5, 285-297.

Baratta, F.I. (1978). *J. Am. Ceram. Soc.*, 61, 490-493.

Baratta, F.I. (1982). *AMMRC*, TR 82-80.

Barker, L.M. (1977). *Eng. Frac. Mech.*, 9, 361-369.

Batchelor, G.K. (1972). *J. Fluid Mech.*, 52, 245-268.

Bergman, B. (1985). *J. Mater. Sci. Let.*, 4, 1143-1146.

Bergman, B. (1986). *J. Mater. Sci.*, 21, 611-614.

Besuner, P.M. (1974). *Mechanics of Crack Growth, ASTM STP 590*, ASTM, pp. 403-419.

Beyer, W.H. (1987). *CRC Standard Mathematical Tables*, CRC Press, 28th Ed.

Blendell, J.E. and R.L. Coble (1982). *J. Am. Ceram. Soc.*, 65, 174-178.

Bluhm, J.I. (1975). *Eng. Frac. Mech. 7*, 593-604.

Bluhm, J.L. (1978). In D.M.R. Tappin (Ed.), *ICF 4*, Vol. 3, Pergamon Press, pp. 409-417.

Booth, F. (1954). *J. Chemical Physics*, 22, 1956-1968.

Bradt, R.C. (1988). Personal communication.

Broek, D. (1978a). *Elementary Engineering Fracture Mechanics*, Sijthoff & Noordhoff, Netherlands. pp. 166-179.

Broek, D. (1978b). *Elementary Engineering Fracture Mechanics*, Sijthoff & Noordhoff, Netherlands. pp. 67-73.

Broek, D. (1978c). *Elementary Engineering Fracture Mechanics*, Sijthoff & Noordhoff, Netherlands. pp. 80-86.

Bueckner, H.F. (1971). *ZAMM*, 51, 97-109.

Bueckner, H.F. (1977). In G.C. Sih, *Fracture Mechanics and Technology*, Vol. II, Sijthoff & noordhoff, pp. 1069-1107.

Butler, E.P. (1985). *Mater. Sci. and Tech.*, 1, 417-432.

Chen, K.J. and Ko, Y.C. (1983). *Ceram. Bull.*, 62, 1030-1035.

Claussen, N. (1984). In N. Claussen, *Science and Technology of Zirconia II*, American Ceramic Society, pp. 325-351.

Claussen, N. (1985). *Mater. Sci. and Eng.*, 71, 23-38.

Coble, R.L. and W.D. Kingery (1956). *J. Am. Ceram. Soc.*, 39, 377-385.

Davidge, R.W. and T.J. Green (1968). *J. Mater. Sci.*, 3, 629-634.

Dickinson, E. (1980). *J. Colloid Interface Sci*, 10, 578-581.

DOD (1983). MIL-STD-1942(MR).

Eshelby, J.D. (1972). Proc. Roy. Soc., 241A, 257-297.

Evans, A.G. and G. Tappin (1972). *Proc. Br. Ceram. Soc.*, 20, 275-297.

Evans, A.G. (1974). *J. Mater. Sci.*, 9, 1145-1152.

Evans, A.G. and T.R. Wilshaw (1976a). *Acta Metall.*, 24, 939-956.

Evans, A.G. and E.A. Charles (1976b). *J. Am. Ceram. Soc.*, 59, 371-372.

Evans, A.G., G.S. Kino, P.T. Khuri-Yakub and B.R. Tittmann (1977). *Mater. Eval.*, 35, 85-96.

Evans, A.G., D.R. Biswas and R.M. Fulrath (1979a). *J. Am. Ceram. Soc.*, 62, 101-106.

Evans, A.G. (1979b). In S.W. Freiman, *Fracture Mechanics Applied to Brittle Materials, ASTM STP 678*, ASTM, pp. 112-135.

Evans, A.G., M.E. Meyer, K.W. Fertig, B.I. Davis and H.R. Baumgartner (1980a). *J. Nond. Eval.*, 1, 111-122.

Evans, A.G. and D.R. Clarke (1980b). In D.P.H. Hasselman, *Thermal Stress in Severe Environment*, Plenum Press, pp. 629-648.

Evans, A.G. and A.H. Heuer (1980c). *J. Am. Ceram. Soc.*, 63, 241-248.

Evans, A.G. (1982a). *J. Am. Ceram. Soc.*, 65, 127-137.

Evans, A.G. (1982b). *J. Am. Ceram. Soc.*, 65, 497-501.

Evans, A.G. and W. Blumenthal (1983). In R.C. Bradt (Ed.), *Fracture Mechanics of Ceramics*, Vol. 6, Plenum Press, pp. 423-448.

Evans, A.G. (1984). In N. Claussen, *Science and Technology of Zirconia II*, American Ceramic Society, pp. 193-212.

Evans, A.G. (1986). *Ceram. Eng. Sci. Proc.*, 7, 1073-1094.

Fegley, B.R., D. White and H.K. Bowen (1985). *Am. Ceram. Soc. Bull.*, 64, 1115-1120.

Ferrari, R. and F. Magrini (1983). In P. Vincenzini (Ed.), *Ceramic Powders*, Elsevier Scientific, pp. 269-282.

Freiman, S.W. (1988). *Ceram. Bull.*, 67, 392-402.

Garvie, R.C. and P.S. Nicholson (1972). *J. Am. Ceram. Soc.*, 55, 152-157.

Garvie, R.C. (1984). In N. Claussen, *Science and Technology of Zirconia II*, American Ceramic Society, pp. 465-479.

Geiger, G.H. and D.R. Poirier (1973). *Transport Phenomena in Metallurgy*, Addison-Wesley, pp. 68-80.

Goodier, J.N. (1933). *J. Appl. Mech.*, 1, 39-44.

Graaf, M.A.C.G., J.H.H. Maat and A.J. Burggraaf (1983). In P. Vincenzini (Ed.), *Ceramic Powders*, Elsevier Scientific, pp. 783-794.

Green, D.J. (1981). *J. Am. Ceram. Soc.*, 64, 138-141.

Green, D.J. (1982). In D.O. Thomson (Ed.), *Review of Progress in Quantitative NDE*, Vol. 1, Plenum Press, pp. 279-285.

Green, D.J. (1983a). In R.C. Bradt (Ed.), *Fracture Mechanics of Ceramics*, Vol. 5, Plenum Press, pp. 457-478.

Green, D.J. (1983b). *J. Am. Ceram. Soc.*, 66, 807-810.

Green, D.J., F.F. Lange and M.R. James (1984). In N. Claussen, *Science and Technology of Zirconia II*, American Ceramic Society, pp. 240-250.

Gupta, T.K., J.H. Bechtold and R.C. Kuznicki (1977). *J. Mater. Sci.*, 12, 2421-2426.

Gupta, T.K., F.F. Lange and J.H. Bechtold (1978). *J. Mater. Sci.*, 13, 1464-1470.

Hasselman, D.P.H. and R.M. Fulrath (1967). *J. Am. Ceram. Soc.*, 50, 399-404.

Himsott, G., D. Munz and T. Fett (1987). *J. Am. Ceram. Soc.*, 70, C-133-C-135.

Hsueh, C.H., A.G. Evans and R.M. Cannon (1986). *Acta Metall.*, 34, 927-936.

Ingel, R.P., D. Lewis, B.A. Bender and R.W. Rice (1982). *J. Am. Ceram. Soc.*, 65, C-150-C-152.

Irwin, G.R. (1962). *J. Appl. Mech.*, 29, 651-654.

Ito, Y.M., M. Rosenblatt and L.Y. Cheng (1981). *Int. J. Frac.*, 17, 483-491.

Jayatilaka, A.S. (1979). *Fracture of Engineering Brittle Materials*, Ch. 5, Applied Science Publishers, pp. 116-135.

Jeryan, R.A. (1978). In E.M. Lenoe (Ed.), *Ceramics for High-Performance Application II*, Brook Hill, pp. 35-51.

JIS (1981). JIS 1601.

Katz, R.W. (1985). *Mater. Sci. and Eng.*, 71, 227-249.

Kellett, B and F.F. Lange (1984). *J. Am. Ceram. Soc.*, 67, 369-371.

Kingery, W.D. and H.K. Bowen and D.R. Uhlmann (1976a). *Introduction to Ceramics*, 2nd Ed., Wiley Interscience, pp. 469-490.

Kingery, W.D. and H.K. Bowen and D.R. Uhlmann (1976b). *Introduction to Ceramics*, 2nd Ed., Wiley Interscience, pp. 770-777.

Kino, G.S., D.M. Barnett and N. Grayeli (1980). *J. Nond. Eval.*, 1, 67-77.

Kirchner, H.P., R.M. Gruver and W.A. Sotter (1986). *Mater. Sci. and Eng.*, 22, 147-156.

Knott, J.F. (1973a). *Fundamental of Fracture Mechanics*. Butterworth,. pp.94-113.

Knott, J.F. (1973b). *Fundamental of Fracture Mechanics*. Butterworth,. pp.114-149.

Knott, J.F. (1980). In D.R.J. Owen (Ed.), *Numerical Methods in Fracture Mechanics*, Pineridge Press, pp. 1-24.

Lange, F.F. (1978). In R.C. Bradt (Ed.), *Fracture Mechanics of Ceramics*, Vol. 4, Plenum Press, pp. 799-819.

Lange, F.F. (1982a). *J. Mater. Sci.*, 17, 235-239.

Lange, F.F. (1982b). *J. Mater. Sci.*, 17, 225-234.

Lange, F.F. (1982c). *J. Mater. Sci.*, 17, 255-262.

Lange, F.F. and M. Metcalfe (1983a). *J. Am. Ceram. Soc.*, 66, 398-406.

Lange, F.F., B.I. Davis and I.A. Aksay (1983b). *J. Am. Ceram. Soc.*, 66, 407-408.

Lange, F.F. (1986a). In P.S. Nicholson (Ed.). *Transaction of the Canadian University-Industry Council on Advanced Ceramics*, 2nd Workshop, pp. 1-29.

Lange, F.F., B.I. Davis and and E. Wright (1986b). *J. Am. Ceram. Soc.*, 69, 66-69.

Lange, F.F., H. Shubert and N. Claussen (1986c). *J. Mater. Sci.*, 21, 768-774.

Larker, H.T. (1985). *Mater. Sci. Eng.*, 71, 329-332.

Lawn, B.R. and D.B. Marshall (1979). *J. Am. Ceram. Soc.*, 62, 347-350.

Lawn, B.R., A.G. Evans and D.B. Marshall (1980). *J. Am. Ceram. Soc.*, 63, 574-581.

Li, L.S. and R.F. Pabst (1980). *J. Mater. Sci.*, 15, 2861-2866.

MacKinnon, R.J. and J.B. Blum (1983). In J.A. Mangels (Ed.), *Advanced in Ceramics*, Vol. 9, American Ceramic Society, pp. 158-163.

Marion, R.H. (1979). In S.W. Freiman, *Fracture Mechanics Applied to Brittle Materials, ASTM STP 678*, ASTM, pp. 104-111.

Marshall, D.B. and B.R. Lawn (1979). *J. Mater. Sci.*, 14, 2001-2012.

Masaki, T (1986). *J. Am. Ceram. Soc.*, 69, 638-640.

Matsui, M, T. Soma and I. Oda (1984). In N. Claussen, *Science and Technology of Zirconia II*, American Ceramic Society, pp. 371-381.

Mattheck, C., P. Morawietz and D. Munz (1983a). *Int. J. Frac.*, 23, 201-212.

Mattheck, C., P. Morawietz and D. Munz (1983b). *Eng. Frac. Mech.*, 18, 633-641.

McMeeking, R.M. and A.G. Evans (1982). *J. Am. Ceram. Soc.*, 65, 242-246.

Mecartney, M.L. (1987). *J. Am. Ceram. Soc.*, 7, 54-58.

Mecholsky, J.J., Jr., S.W. Freiman and R.W. Rice (1976). *J. Mater. Sci.*, 11, 1310-1319.

Miller, C.A. and P. Neogi (1985). *Interfacial Phenomena*, Marcel Dekker, pp. 91-134.

Mizuta, S.and H.K. Bowen (1984). *Ceram. Int.*, 10, 43-48.

Munz, D., R.T. Bubsey and J.L. Shannon, Jr. (1980). *J. Test. Eval.*, 8, 103-107.

Munz, D., R.T. Bubsey and J.L. Shannon, Jr. (1981). *J. Am. Cerm. Soc.*, 63, 300-305.

Munz, D. (1983). In R.C. Bradt (Ed.), *Fracture Mechanics of Ceramics*, Vol. 5, Plenum Press, pp. 457-478.

Narayanaswamy, O.S. and R. Gardon (1969). *J. Am. Ceram. Soc.*, 52, 554-558.

Newman, J.C. (1984). In Underwood, J.H., (Ed.), *Chevron-Notched Specimens: Testing and Stress Analysis*, ASTM STP 855, pp. 5-31.

Niihara, K., R. Morena and D.P.H. Hasselman (1982). *J. Mater. Sci.* Let., 17, 13-16.

Ostojic, P. and R. McPherson (1987). *Int. J. of Frac.*, 33, 297-312.

Oliver D.R. (1961). *Chemical Eng. Sci.*, 15, 230-242.

Pampuch, P. and K. Haberko (1983). In P. Vincenzini (Ed.), *Ceramic Powders*, Elsevier Scientific, Amsterdam, pp. 623-634.

Parfitt, G.D. (1973). *Dispersion of Powder in Liquids*, 2nd Ed., Applied Science Publishers, pp. 1-2.

Parish, M.V. and H.K. Bowen (1984). *Ceramic International*, 10, 75-77.

Parish, M.V., R.R. Garcia and H.K. Bowen (1985). *J. Mater. Sci.*, 20, 996-1008.

Parker, A.P. (1981a). *The Mechanics of Fracture and Fatigue*, E. & F. N. Spon, pp.30-48.

Parker, A.P. (1981b). *The Mechanics of Fracture and Fatigue*, E. & F. N. Spon, pp.49-88.

Pimental, G.C. (1960). *The Hydrogen Bond*, W.H. Freeman, pp. 3-9.

Porter, L. and A.H. Heuer (1979). *J. Am. Ceram. Soc.*, 62, 298-305.

Quinn, G.D. (1984). *Ceram. Eng. Sci. Proc.*, 5, 298-311.

Reed, C.C. and J.L. Anderson (1976). In M. Kerker (Ed.) *Colloids and Interfacial Science*, Vol. IV, Academic Press, pp. 501-512.

Reed, J.S., T.Carbone and C. Scott (1978). In H. Palmour III (Ed.), Materials Science and Research, Vol. 11, Plenum Press, 171-180.

Rhodes, W.H. (1981). *J. Am. Ceram. Soc.*, 64, 19-22.

Rice, J.R. (1972). *Int. J. Solid Structure*, 8, 751-758.

Rice, R.W. (1974). In R.C. Bradt (Ed.), *Fracture Mechanics of Ceramics*, Vol. 1, Plenum Press, pp. 323-345.

Rice, R.W. and B.J. Hockey (Eds.) (1979). *The Science of Ceramic Machining and Surface Finishing II*, NBS Special Publication 562.

Rice, R.W. (1980a). *J. Am. Ceram. Soc.*, 63, 703-710.

Rice, R.W. (1980b). *J. Am. Ceram. Soc.*, 63, 129-136.

Richerson, D.W. (1982). *Modern Ceramic Engineering*, Marcel Dekker, pp. 325-374.

Richarson, J.F. (1954). *Trans. INSTN. Chem. Engrs.*, 32, 35-53.

Ruhle, M., N. Claussen and A.H Heuer (1984). In N. Claussen, *Science and Technology of Zirconia II*, American Ceramic Society, pp. 352-370.

Salem, J.A. and J.L. Shannon, Jr. (1987). *J. Mater. Sci.*, 22, 321-324.

Sato, T. (1985). *J. Am. Cerm. Soc.*, 68, 356-359.

Schneider, S.J. and R.W. Rice (Eds.) (1972). *The Science of Ceramic Machining and Surface Finishing*, NBS Special Publication 348.

Selsing, J. (1961). *J. Am. Cerm. Soc.*, 44, 419.

SESA (1980). *Experimental Mech.*, 20, 253-264.

Seshadri, S.G. and M. Srinivasan (1981). *J. Am. Ceram. Soc.*, 64, C-69-C-71.

Shannon, J.L.,Jr. and D.G. Munz (1984). In Underwood, J.H., (Ed.), *Chevron-Notched Specimens: Testing and Stress Analysis*, ASTM STP 855, pp. 5-31.

Shih, T.T. (1979). *Eng. Frac. Mech.*, 12, 479-498.

Shih, T.T. (1981). *J. Test. Eval.*, 9, 50-55.

Stanley, P. (1973). *Proc. Brit. Ceram. Soc.*, 22, 453-487.

Subbarao, E.C. (1981). In A.H. Heuer, *Science and Technology of Zirconia*, American Ceramic Society, pp. 1-13.

Sung, J. and P.S. Nicholson (1988). *J. Am. Ceram. Soc.*, submitted for publication.

Swain, M.V. (1985). *J. Am. Ceram. Soc.*, 68, C-97-C-99.

Swain, M.V. (1986). In R.C. Bradt (Ed.), *Fracture Mechanics of Ceramics*, Vol. 8, Plenum Press, pp. 151-162.

Taguchi, H., Y. Takahashi and H. Miyamoto (1985). *J. Am. Ceram. Soc.*, 68, C-264-C-265.

Tiller, F.M. and C.D. Tsai (1986). *J. Am. Ceram. Soc.*, 69, 882- 887.

Troczynski, T.B. and P.S. Nicholson (1985). *J. Am. Ceram. Soc.*, 68, 439-443.

Troczynski, T B. (1987a). *Ph.D. Thesis*, McMaster University.

Troczynski, T.B. and P.S. Nicholson (1987b). *J. Am. Ceram. Soc.*, 70, 78-85.

Tsai, R.L. and R. Raj (1982). *Acta Metall.*, 30, 1043-1058.

Tsukuma, K., Y. Kubotaand T. Tsukidate (1984) In N. Claussen, *Science and Technology of Zirconia II*, American Ceramic Society, pp. 382-390.

Tsukuma, K. and M. Shimada (1985a). *Am. Ceram. Soc. Bull.*, 64, 310-313.

Tsukuma, K. and K. Ueda (1985b). *J. Am. Ceram. Soc.*, 68, C-56 -C-58.

Tskuma, K. and M. Shimada (1985c) *J. Mater. Sci.*, 20, 1178-1184.

Tsukuma, K. and K. Ueda (1985d). *J. Am. Ceram. Soc.*, 68, C-4-C-58.

Underwood, J.H., S.W. Freiman and F.I. Baratta (Eds.) (1984). *Chevron-Notched Specimens: Testing and Stress Analysis*, ASTM.

Usami, S., H. Kimoto and I. Takahashi (1986). *Eng. Frac. Mech.*, 23, 745-761.

Weibull, W. (1951). *J. Appl. Mech.*, 18, 293-297.

Weil, N.A. and Daniel, I.M. (1964). *J. Am. Ceram. Soc.*, 47, 268-274.

Wiederhorn, S.M. (1974). In R.C. Bradt (Ed.), *Fracture mechanics of Ceramics*, Vol. 2, Plenum Press, pp. 613-646.

Woods, D.R. (1988a). *Surface Colloids and Unit Operation*, ChE 6Z3 Textbook, McMaster University, pp. 2-1-2-20.

Woods, D.R. (1988b). *Surface Colloids and Unit Operation*, ChE 6Z3 Textbook, McMaster University, pp. 1-30-1-46.

Woods, D.R. (1988c). *Surface Colloids and Unit Operation*, ChE 6Z3 Textbook, McMaster University, pp. 8-1-8-71.

Wu, S.X. (1984). *Int. J. Frac.*, 26, R43-R47.

Wu, X.R. and J. Carlsson (1984). In J. Carlsson (Ed.), *ICM 4*, Vol. 2, pp. 935-941.